10. SITE 1082[1]

Shipboard Scientific Party[2]

HOLE 1082A

Position: 21°5.6373′S, 11°49.2361′E

Start hole: 0445 hr, 13 September 1997

End hole: 0005 hr, 16 September 1997

Time on hole: 67.33 hr

Seafloor (drill pipe measurement from rig floor, mbrf): 1290.7

Total depth (drill pipe measurement from rig floor, mbrf): 1891.3

Distance between rig floor and sea level (m): 11.4

Water depth (drill pipe measurement from sea level, m): 1279.3

Penetration (mbsf): 600.6

Coring totals:
Type: APC
Number: 14
Cored: 128.60 m
Recovered: 134.88 m (104.88%)

Type: XCB
Number: 50
Cored: 472.0 m
Recovered: 367.13 m (77.78%)

Lithology:
Subunit IA: intercalated intervals of nannofossil- and foraminifer-rich clay
Subunit IB: intercalated intervals of nannofossil- and diatom-rich clay and nannofossil-rich diatomaceous clay
Subunit IC: intercalated intervals of nannofossil-rich clay and nannofossil clay
Unit II: nannofossil ooze

HOLE 1082B

Position: 21°5.6517′S, 11°49.2326′E

Start hole: 0005 hr, 16 September 1997

End hole: 0825 hr, 16 September 1997

Time on hole: 8.42 hr

Seafloor (drill pipe measurement from rig floor, mbrf): 1291.8

Total depth (drill pipe measurement from rig floor, mbrf): 1418.8

Distance between rig floor and sea level (m): 11.4

Water depth (drill pipe measurement from sea level, m): 1280.4

Penetration (mbsf): 127

Coring totals:
Type: APC
Number: 14
Cored: 127.0 m
Recovered: 133.17 m (104.86%)

Lithology:
Subunit IA: intercalated intervals of nannofossil- and foraminifer-rich clay
Subunit IB: intercalated intervals of nannofossil- and diatom-rich clay and nannofossil-rich diatomaceous clay

HOLE 1082C

Position: 21°5.6690′S, 11°49.2342′E

Start hole: 0825 hr, 16 September 1997

End hole: 0200 hr, 17 September 1997

Time on hole: 17.58 hr

Seafloor (drill pipe measurement from rig floor, mbrf): 1293.5

Total depth (drill pipe measurement from rig floor, mbrf): 1495.5

Distance between rig floor and sea level (m): 11.4

Water depth (drill pipe measurement from sea level, m): 1282.1

Penetration (mbsf): 202

Coring totals:
Type: APC
Number: 24
Cored: 202 m
Recovered: 217.83 m (107.84%)

Lithology:
Subunit IA: intercalated intervals of nannofossil- and foraminifer-rich clay
Subunit IB: intercalated intervals of nannofossil- and diatom-rich clay and nannofossil-rich diatomaceous clay

Principal results: Site 1082 is located in 1280-m deep water ~120 km to the southeast of Deep Sea Drilling Project (DSDP) Site 532, within the Northern Cape Basin. Together with Ocean Drilling Program (ODP) Sites 1081 and 1083 and DSDP Sites 532 and 362, it is part of a transect that is central to the reconstruction of the history of the Benguela Current. Site 1082 is closest to the coast and is expected to contain a direct record of upwelling history in the Walvis Bay area. The DSDP sites are well seaward of the upwelling center but contain an upwelling signal that was transported to this location by the Benguela Current and its filaments and eddies. Compared with DSDP Site 532, which shows evidence of sediment redeposition, Site 1082 offers a more continuous and less disturbed sequence.

Three holes were cored with the advanced hydraulic piston corer/extended core barrel (APC/XCB) at Site 1082 to a maximum depth of 600.6 meters below seafloor (mbsf). Hole 1082A was cored with the APC to 128.6 mbsf and was extended with the XCB to a depth of 600.6 mbsf. Hole 1082A was logged with a full suite of sensors (seismostratigraphic suite, lithoporosity suite, Formation MicroScanner [FMS] suite, and the geolog-

[1]Wefer, G., Berger, W.H., Richter, C., et al., 1998. *Proc. ODP, Init. Repts.,* 175: College Station, TX (Ocean Drilling Program).

[2]Shipboard Scientific Party is given in the list preceding the Table of Contents.

ical high-sensitivity magnetic tool [GHMT]) from 599.3 to 65 mbsf. At Hole 1082B, 14 cores were taken with the APC to 127.0 mbsf. Hole 1082C was cored with the APC to 202 mbsf. Detailed comparisons between the magnetic susceptibility and the gamma-ray attenuation porosity evaluator (GRAPE) density records generated on the multisensor track (MST) and the color reflectance measured with the Minolta spectrophotometer demonstrated complete recovery of the sedimentary sequence down to 141 meters composite depth (mcd).

Drilling at Site 1082 recovered an apparently continuous hemipelagic sedimentary section spanning the upper Miocene to Holocene (0–5.8 Ma). The upper part of the succession is composed of moderately bioturbated, intercalated intervals of olive to black clays, which contain varying abundances of diatoms, nannofossils, foraminifers, and radiolarians. Three subunits are defined based on the various abundances and types of microfossils in the sediments: nannofossil- and foraminifer-rich clay (0–112 mbsf), diatom-rich clay (112–369 mbsf), and nannofossil clay (369–475 mbsf). The underlying lithostratigraphic unit (475–590 mbsf) consists of homogeneous, greenish gray nannofossil ooze. The lithostratigraphy at Site 1082 can be correlated to the one identified at Site 1081. Differences between these two sites are the higher sedimentation rates (70–200 m/m.y.) and the better temporal resolution at Site 1082. Sediments at Site 1082 also have higher abundances of nannofossils than those at Site 1081.

The detrital component of the sediments consists of clay with rare silt-sized, angular and subangular, mono- and polycrystalline quartz and feldspar grains. Muscovite and biotite are present in trace amounts. Dolomite rhombs are observed in the diatom-rich clay and the nannofossil ooze. The biogenic component is represented by varying abundances of foraminifers (whole and fragments), nannofossils, diatoms, radiolarians, sponge spicules, and silicoflagellates.

Fine biostratigraphic resolution was achieved by integrating datums from all microfossil groups. Calcareous nannofossils are abundant within the entire section. Planktonic foraminifers indicate upwelling at 70 mbsf, and downhole faunal variations indicate that a warm surface-water current (Angola Current) reached the region in the past. Tropical to warm subtropical species appear at 36 mbsf. The surface-water warming is associated with a decrease in upwelling, as indicated by a reduced abundance of *Globigerina bulloides.* The benthic foraminiferal fauna shows high diversity throughout the entire section. The record of diatom abundance points to a substantial increase in deposition during the upper Pliocene and lower Pleistocene intervals, reaching a maximum in upper Pliocene sediments, followed by a decrease within the Pleistocene interval at ~1 Ma. Overall abundances are low, or diatoms are absent, in upper Miocene and lower Pliocene sediments. The diatom content at Site 1082 probably reflects a varying nutrient supply that could be related to upwelling of nutrient-rich deeper waters and high biological productivity, especially in the upper Pliocene sediment. The diatom assemblage is similar to that at Site 1081 and consists mainly of a mixture of upwelling-indicator species.

The polarity of the remanent magnetization was determined from the magnetic declinations and inclinations of APC cores and from the magnetic inclinations of XCB cores after alternating-field (AF) demagnetization at 20 mT. All chrons from the Brunhes (C1n) to the onset of the C3An at ~6 Ma could be identified. A short reversal event (Cobb Mountain) was observed at all three holes within the Matuyama Chron. The Reunion event (2.14–2.15 Ma) appears at Hole 1082C between ~196 and 197 mbsf.

Well-developed cycles, in which concentrations of calcium carbonate and organic carbon vary between 1 and 85 wt% and <0.1 and 16.1 wt%, respectively, reflect fluctuations in the elevated marine production associated with the Benguela Current. Higher concentrations of organic carbon from 0 to 260 mbsf record higher productivities during the last 2 m.y. than earlier in the history of this upwelling system. The interstitial water chemical profiles record a relatively shallow (0–20 mbsf) region in which diagenetic degradation of organic matter consumes sulfate and produces increases in alkalinity, ammonium, and phosphate that ultimately exceed those found at nearby Site 1081 on the Walvis Ridge. These changes are accompanied by calcite dissolution and dolomite precipitation, which are recorded by increases in dissolved strontium and decreases in dissolved magnesium and calcium.

Physical sediment properties were determined both by high-resolution MST core logging and index properties measurements. Magnetic susceptibility and GRAPE signals reveal pronounced cyclicities, which were used for high-quality stratigraphic correlation in conjunction with digital color data.

Logging in Hole 1082A is characterized by a regular hole size (10- to 11-in diameter) with numerous small enlargements from 530 to 120 mbsf and by washout zones at the top and bottom of the logged interval. Thirteen dolomitic layers were identified in the downhole logs, characterized by very high velocity, resistivity, and density, and by low gamma-ray intensity. Dolomitic layers are present in the entire interval, but are particularly concentrated in the lower half. The core and log measurements of natural gamma-ray intensity are very similar and can be used for detailed correlations between the core and log data sets. In Hole 1082A, log depth is similar to core depth. The logging data from Sites 1081 and 1082 show a reliable correlation.

We expect that glacial/interglacial climatic cycles are well developed at Site 1082 in terms of productivity, carbonate dissolution, and terrigenous sedimentation cycles. In addition, the sediments from Site 1082 will document the supply of minerals and plant remains from land as a function of changing climate and sea level. Together with the results of DSDP Site 532, the record of ODP Site 1082 will allow the definition of offshore gradients and the high-resolution reconstruction of the intensity of the Benguela Current. We expect detailed information of the history of upwelling, both on the scale of glacial/interglacial cycles and sub-Milankovitch cycles. Trends will be compared with the records north and south of the Walvis Ridge to identify long-term changes in boundary conditions.

BACKGROUND AND OBJECTIVES

Sites 1082 (1290 m) and 1083 (2200 m), together with DSDP Sites 532 and 362 (1331 and 1325 m water depth, respectively) and Site 1081 (760 m water depth), form a transect that is central to the reconstruction of the history of the Benguela Current. Details on the background and objectives for this entire set of sites, including Site 1082, are given in the "Site 1081" chapter (this volume). This site is closest to the coast and is expected to contain a direct record of upwelling history in the Walvis Bay area. The DSDP sites are farther seaward of the upwelling center but contain an upwelling signal that was transported to this location by the Benguela Current and its filaments and eddies. Site 1082 has a similar water depth to that of DSDP Site 532 but lies about 120 km to the southeast, within the Northern Cape Basin.

Compared with DSDP Site 532, which shows evidence of sediment redeposition (seen as mud waves in seismic profiles), Site 1082 has a more continuous and less disturbed sequence. The difference in bottom-current strength is thought to be related to topographic enhancement at the southern slope of the Walvis Ridge, which forms a barrier to deep-water flow.

We expect that glacial/interglacial climatic cycles are well expressed at Site 1082 (as they are at DSDP Site 532) in terms of productivity, carbonate dissolution, and continental sedimentation cycles. From DSDP Site 532 results, we expect a general opal maximum in the late Pliocene to early Pleistocene and a silica reversal within the glacial/interglacial cycles at the end of the Miocene from high opal during glacials in the older sediments to high opal during interglacials in younger sediments. At the lower productivity levels of Site 1082, compared with Site 1081, we expect a higher carbonate content and better preservation of calcareous fossils, which will be useful in the pursuit of biostratigraphic and paleoceanographic studies, especially when comparing the responses of siliceous and calcareous plankton with climatic change. In addition, the sediments from

Site 1082 will document the supply of minerals and plant remains from land as a function of changing climate and sea level.

OPERATIONS

Hole 1082A (Proposed Site WB-B)

The 93-nmi voyage to Site 1082 was accomplished at an average speed of 11.6 kt. The vessel approached the Global Positioning System coordinates of the site and deployed a beacon at 0445 hr on 13 September. Hole 1082A was spudded with the APC at 0750 hr. The seafloor depth was established from the recovery of the first core at 1279.3 meters below sea level (mbsl). APC coring advanced without incident to 128.6 mbsf, with 104.9% recovery (Table 1; also see the expanded core summary table on CD-ROM, back pocket, this volume). Cores were oriented starting with Core 175-1082A-3H. Adara heat-flow measurements were taken at 45.8 mbsf (5H), 64.8 mbsf (7H), 83.8 mbsf (9H), and 102.8 mbsf (11H). The hole was deepened with the XCB to 600.6 mbsf (64X), which was the depth objective for this site. The penetration with the XCB was 472.0 m, with 77.8% recovery.

Logging Operations in Hole 1082A

In preparation for logging, an aluminum go-devil was dropped to ensure the opening of the lockable float valve, and the hole was flushed with a high-viscosity mud treatment. The drill string was then pulled up, and the bit was placed at the logging depth of 94.1 mbsf. Hole 1082A was logged with a full suite of sensors. For each run, the pipe was set at 94.1 mbsf and pulled back to 65.0 mbsf during logging. Logging operations began at 0200 hr on 15 September. The first log was conducted with the seismostratigraphic suite (25.8 m long). This suite was made up of the spectral gamma-ray (NGT), long-spacing sonic (LSS), phasor dual-induction (DIT), and Lamont-Doherty high-resolution temperature (TLT) sondes. This tool string was deployed in the pipe at 0255 hr and logged the hole up from 599.3 mbsf. The tool was recovered at 0700 hr. The second log was made with the lithoporosity suite (19.5 m long) and included the hostile environment natural gamma spectrometry (HNGS), accelerator porosity (APS), lithodensity (LDS), and TLT sondes. The tool string was deployed at 0800 hr and logged the hole up from 599.3 mbsf. The tool was pulled out of the pipe at 1225 hr. The third logging run was made with the FMS suite (12.10 m long) and included the NGT, general purpose inclinometer, and FMS sondes. This tool was deployed at 1325 hr and logged the hole up from 599.3 mbsf. The tool was recovered at 1700 hr. The fourth and last log was made with the magnetic susceptibility suite (11.8 m long) and included the NGT, magnetic susceptibility, and the nuclear resonance magnetometer sondes. The tool string was deployed in the pipe at 1730 hr and logged the hole up from 599.3 mbsf. It was retrieved at 2010 hr. The logging equipment was rigged down by 2100 hr, and the hole was filled with heavy mud. The drill string was then pulled out of the hole, and the bit cleared the seafloor at 0005 hr on 16 September.

Hole 1082B

The vessel was offset 30 m to the south, and Hole 1082B was spudded with the APC at 0110 hr on 16 September. The recovery of the first core established the seafloor depth at 1280.4 mbsl. APC coring advanced without incident to refusal at 127.0 mbsf, with 104.9% recovery (Table 1). Cores were oriented starting with Core 175-1082B-4H. The bit cleared the seafloor at 0855 hr on 16 September, thereby ending operations at Hole 1082B.

Table 1. Coring summary for Site 1082.

Core	Date (Sept 1997)	Time (UTC)	Interval (mbsf)	Length cored (m)	Length recovered (m)	Recovery (%)
175-1082A-						
1H	13	0800	0.0-7.8	7.8	7.89	101.2
2H	13	0830	7.8-17.3	9.5	9.62	101.3
3H	13	0900	17.3-26.8	9.5	9.91	104.3
4H	13	0925	26.8-36.3	9.5	9.96	104.8
5H	13	1005	36.3-45.8	9.5	10.27	108.1
6H	13	1030	45.8-55.3	9.5	10.07	106.0
7H	13	1115	55.3-64.8	9.5	10.22	107.6
8H	13	1145	64.8-74.3	9.5	10.52	110.7
9H	13	1235	74.3-83.8	9.5	10.32	108.6
10H	13	1320	83.8-93.3	9.5	10.62	111.8
11H	13	1405	93.3-102.8	9.5	10.27	108.1
12H	13	1440	102.8-112.3	9.5	10.39	109.4
13H	13	1515	112.3-121.8	9.5	7.99	84.1
14H	13	1615	121.8-128.6	6.8	6.83	100.4
15X	13	1725	128.6-138.3	9.7	6.75	69.6
16X	13	1800	138.3-147.9	9.6	7.09	73.9
17X	13	1835	147.9-157.6	9.7	4.95	51.0
18X	13	1910	157.6-167.2	9.6	5.51	57.4
19X	13	1940	167.2-176.9	9.7	5.59	57.6
20X	13	2015	176.9-186.5	9.6	6.66	69.4
21X	13	2050	186.5-196.2	9.7	7.02	72.4
22X	13	2155	196.2-205.9	9.7	5.16	53.2
23X	13	2230	205.9-215.5	9.6	7.34	76.5
24X	13	2300	215.5-225.2	9.7	7.58	78.1
25X	13	2340	225.2-234.8	9.6	6.28	65.4
26X	14	0020	234.8-244.4	9.6	9.63	100.3
27X	14	0045	244.4-254.0	9.6	7.77	80.9
28X	14	0105	254.0-263.6	9.6	8.19	85.3
29X	14	0140	263.6-273.3	9.7	9.61	99.1
30X	14	0205	273.3-282.9	9.6	7.28	75.8
31X	14	0230	282.9-292.5	9.6	6.25	65.1
32X	14	0255	292.5-302.1	9.6	7.17	74.7
33X	14	0320	302.1-311.7	9.6	7.58	79.0
34X	14	0345	311.7-321.4	9.7	6.02	62.1
35X	14	0510	321.4-327.5	6.1	7.25	118.9
36X	14	0610	327.5-331.0	3.5	1.10	31.4
37X	14	0640	331.0-340.6	9.6	6.06	63.1
38X	14	0705	340.6-350.3	9.7	8.68	89.5
39X	14	0735	350.3-359.9	9.6	6.24	65.0
40X	14	0800	359.9-369.5	9.6	6.61	68.9
41X	14	0825	369.5-379.2	9.7	8.84	91.1
42X	14	0915	379.2-388.8	9.6	7.87	82.0
43X	14	0950	388.8-398.4	9.6	7.36	76.7
44X	14	1020	398.4-408.1	9.7	6.77	69.8
45X	14	1050	408.1-417.7	9.6	6.98	72.7
46X	14	1115	417.7-427.3	9.6	6.46	67.3
47X	14	1140	427.3-437.0	9.7	5.76	59.4
48X	14	1225	437.0-446.7	9.7	5.80	59.8
49X	14	1300	446.7-456.3	9.6	9.25	96.4
50X	14	1335	456.3-465.9	9.6	7.81	81.4
51X	14	1405	465.9-475.1	9.2	6.95	75.5
52X	14	1440	475.1-484.7	9.6	7.40	77.1
53X	14	1515	484.7-494.4	9.7	7.25	74.7
54X	14	1550	494.4-504.1	9.7	9.26	95.5
55X	14	1630	504.1-513.8	9.7	9.63	99.3
56X	14	1715	513.8-523.4	9.6	9.45	98.4
57X	14	1755	523.4-533.1	9.7	9.33	96.2
58X	14	1840	533.1-542.8	9.7	8.93	92.1
59X	14	1915	542.8-552.4	9.6	7.30	76.0
60X	14	2025	552.4-562.0	9.6	8.78	91.5
61X	14	2105	562.0-571.7	9.7	8.53	87.9
62X	14	2150	571.7-581.3	9.6	8.12	84.6
63X	14	2230	581.3-590.9	9.6	8.80	91.7
64X	14	2315	590.9-600.6	9.7	9.13	94.1
Coring totals:				600.6	502.01	83.9
175-1082B-						
1H	16	120	0.0-3.7	3.7	3.70	100.0
2H	16	145	3.7-13.2	9.5	9.75	102.6
3H	16	205	13.2-22.7	9.5	9.99	105.2
4H	16	240	22.7-32.2	9.5	9.75	102.6
5H	16	310	32.2-41.7	9.5	10.10	106.3
6H	16	340	41.7-51.2	9.5	10.29	108.3
7H	16	410	51.2-60.7	9.5	9.64	101.5
8H	16	435	60.7-70.2	9.5	10.11	106.4
9H	16	505	70.2-79.7	9.5	10.17	107.1
10H	16	530	79.7-89.2	9.5	10.03	105.6
11H	16	605	89.2-98.7	9.5	10.05	105.8
12H	16	635	98.7-108.2	9.5	10.15	106.8
13H	16	705	108.2-117.7	9.5	10.08	106.1
14H	16	730	117.7-127	9.3	9.36	100.6
Coring totals:				127.0	133.17	104.9
175-1082C-						
1H	16	0905	0.0-3.5	3.5	3.56	101.7
2H	16	0930	3.5-13.0	9.5	8.06	84.8

Table 1 (continued).

Core	Date (Sept 1997)	Time (UTC)	Interval (mbsf)	Length cored (m)	Length recovered (m)	Recovery (%)
3H	16	0955	13.0-22.5	9.5	10.04	105.7
4H	16	1020	22.5-27.0	4.5	9.97	221.6
5H	16	1050	27.0-36.5	9.5	10.10	106.3
6H	16	1115	36.5-46.0	9.5	9.95	104.7
7H	16	1140	46.0-55.5	9.5	10.14	106.7
8H	16	1210	55.5-65.0	9.5	10.11	106.4
9H	16	1240	65.0-74.5	9.5	9.89	104.1
10H	16	1310	74.5-84.0	9.5	9.61	101.2
11H	16	1340	84.0-93.5	9.5	10.04	105.7
12H	16	1410	93.5-103.0	9.5	9.94	104.6
13H	16	1440	103.0-112.5	9.5	10.08	106.1
14H	16	1510	112.5-122.0	9.5	10.13	106.6
15H	16	1545	122.0-125.0	3.0	3.51	117.0
16H	16	1625	125.0-134.5	9.5	10.12	106.5
17H	16	1655	134.5-144.0	9.5	10.41	109.6
18H	16	1730	144.0-153.5	9.5	10.78	113.5
19H	16	1805	153.5-163.0	9.5	10.06	105.9
20H	16	1845	163.0-172.5	9.5	10.09	106.2
21H	16	1925	172.5-182.0	9.5	10.46	110.1
22H	16	1955	182.0-191.5	9.5	8.39	88.3
23H	16	2040	191.5-195.6	4.1	5.96	145.4
24H	16	2150	195.6-202.0	6.4	6.43	100.5
Coring totals:				202.0	217.83	107.8

Notes: UTC = Universal Time Coordinated. An expanded version of this coring summary table that includes lengths and depths of sections and comments on sampling is included on CD-ROM (back pocket, this volume).

Hole 1082C

Hole 1082C was spudded with the APC at 0855 hr on 16 September. The recovery of the first core established the seafloor depth at 1282.1 mbsl. APC coring advanced to 202.0 mbsf, with 107.8% recovery. The last two cores (175-1082C-23H and 24H) were partial strokes. Cores were oriented starting with Core 175-1082C-3H. The drill string was then retrieved with the bit clearing the seafloor at 2315 hr. The beacon was recovered, and the hydrophones and thrusters were retracted. The vessel was under way to Site 1083 at 0200 hr on 17 September.

SITE GEOPHYSICS

For a discussion of site geophysics at Site 1082, see "Site Geophysics" section, "Site 1081" chapter (this volume).

LITHOSTRATIGRAPHY

Description of Lithostratigraphic Units

Sediments from Site 1082 form two lithostratigraphic units (Fig. 1). Unit I is composed of moderately bioturbated, intercalated intervals of olive (5Y 4/3), olive-gray (5Y 4/2), dark olive-gray (5Y 4/1), and black (5Y 2.5/1) clays, which contain varying abundances of diatoms, nannofossils, foraminifers, and radiolarians. Three subunits are distinguished based on microfossil type and abundance: Subunits IA, IB, and IC. Unit II is composed of homogeneous, greenish gray (5GY 6/1), light greenish gray (5GY 7/1), and olive-gray (5Y 4/2) nannofossil ooze. Units and subunits at Site 1082 are correlative to those identified at Site 1081. Differences between these two sites are the higher sedimentation rates and the better temporal resolution at Site 1082 compared with Site 1081. Sediments from Site 1082 also have higher abundances of nannofossils than those from Site 1081.

Unit I

Interval: 175-1082A-1H-1, 0 cm, through 175-1082A-51X
Age: Holocene to early Pliocene
Depth: 0–475 mbsf

Subunit IA

Intervals: 175-1082A-1H-1, 0 cm, through 175-1082A-12H; 175-1082B-1H-1, 0 cm, through 175-1082B-13H; 175-1082C-1H-1, 0 cm, through 175-1082C-13H
Age: Holocene to Pleistocene
Depth: 0–112 mbsf

The uppermost subunit is composed of intercalated intervals of moderately bioturbated, olive (5Y 4/3) and olive-gray (5Y 4/2), nannofossil- and foraminifer-rich clay. Subunit IA contains intervals of different colored clays which range in thickness from 60 to 250 cm. They grade into each other over 20 to 30 cm (Fig. 2). Within Subunit IA some intervals contain nannofossil oozes (e.g., 175-1082A-6H-5, 90 cm, to 6H-6, 15 cm). Subunit IA generally has high carbonate and organic carbon contents, which average 42 and 6 wt%, respectively (see "Organic Geochemistry" section, this chapter). The contact between Subunits IA and IB is defined as the depth below which the diatom abundance shifts from diatom-bearing to diatom-rich. This transition is gradational and occurs between Cores 175-1082A-12H and 13H (112.3 mbsf), 175-1082B-13H and 14H, and 175-1082C-13H and 14H. The diatom abundance within the sediments begins to increase in Cores 175-1082A-8H, 175-1082B-8H, and 175-1082C-9H.

Subunit IB

Interval: 175-1082A-13H through 175-1082A-40X
Age: Pleistocene to late Pliocene
Depth: 112–369 mbsf

Subunit IB was intersected in all three holes, but its contact with Subunit IC is only observed between Cores 175-1082A-40X and 41X (359.9 mbsf). Subunit IB is composed of intercalated intervals of dark olive-gray (5Y 3/2) and olive (5Y 5/3) nannofossil- and diatom-rich clay and nannofossil-rich diatomaceous clay. Intervals of different colored clays range in thickness from 60 to 250 cm and grade into each other over 20 to 30 cm. Subunit IB contains several black (2.5Y 2.5/2) and olive-black (5Y 2.5/2), 35- to 150-cm-thick, clay intervals that have lower nannofossil abundances, higher abundances of organic matter, and coarse silt-sized, subangular mono- and polycrystalline quartz grains (see "Synthesis of Smear-Slide Analyses" section, this chapter). These intervals grade into the lighter colored clays over 20 to 40 cm (e.g., 175-1082A-16X-4, 90 cm, to 1082A-16X-CC, 50 cm; 175-1082A-18X-3, 90 cm, to 1082A-18X-4, 80 cm; 175-1082A-19X-4, 10 cm, to 1082A-19X-5, 15 cm; 175-1082A-19X-6, 23–59 cm; see visual core descriptions, Section 4, this volume). Subunit IB is darker in color and has a lower total reflectance than Subunit IA. Its color is thought to reflect higher organic carbon contents. Organic carbon concentrations range from 2 to 8 wt% and average 4 wt%. Calcium carbonate concentrations are lower than in Subunit IA, averaging 33 wt%.

The contact between Subunits IB and IC is marked by a change in the abundance of diatoms from diatom-rich to diatom-bearing clays, or clays with trace abundances of diatoms (see "Synthesis of Smear-Slide Analyses" and "Biostratigraphy and Sedimentation Rates" sections, this chapter). The boundary is located between Cores 175-1082A-40X and 41X (369.5 mbsf) and is gradational over several tens of meters. Nannofossils and foraminifers are present in higher abundances at Site 1082 than at Site 1081. Dolomitized clays are present in Subunit IB at intervals 175-1082A-15X-1, 0–13 cm (128.6 mbsf); 22X-3, 114–145 cm (200.7 mbsf); and 36X-1, 0–17 cm (327.5 mbsf).

Subunit IC

Interval: 175-1082A-41X through 175-1082A-51X
Age: early Pliocene to Miocene
Depth: 369–475 mbsf

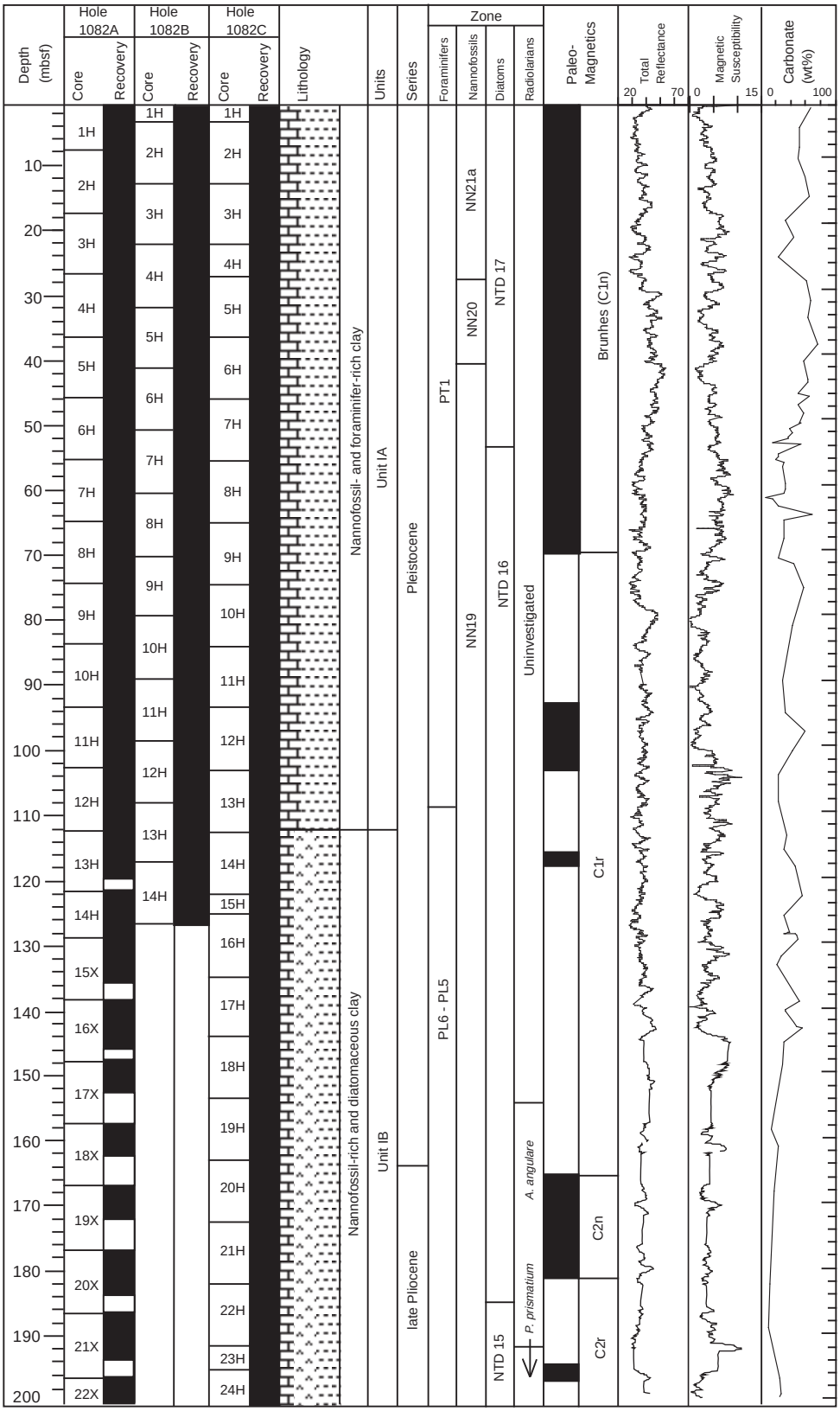

Figure 1. Composite stratigraphic section for Site 1082 showing core recovery in all holes, a simplified summary of lithology, age, total reflectance (400–700 nm), magnetic susceptibility, and calcium carbonate contents. (Continued next page.)

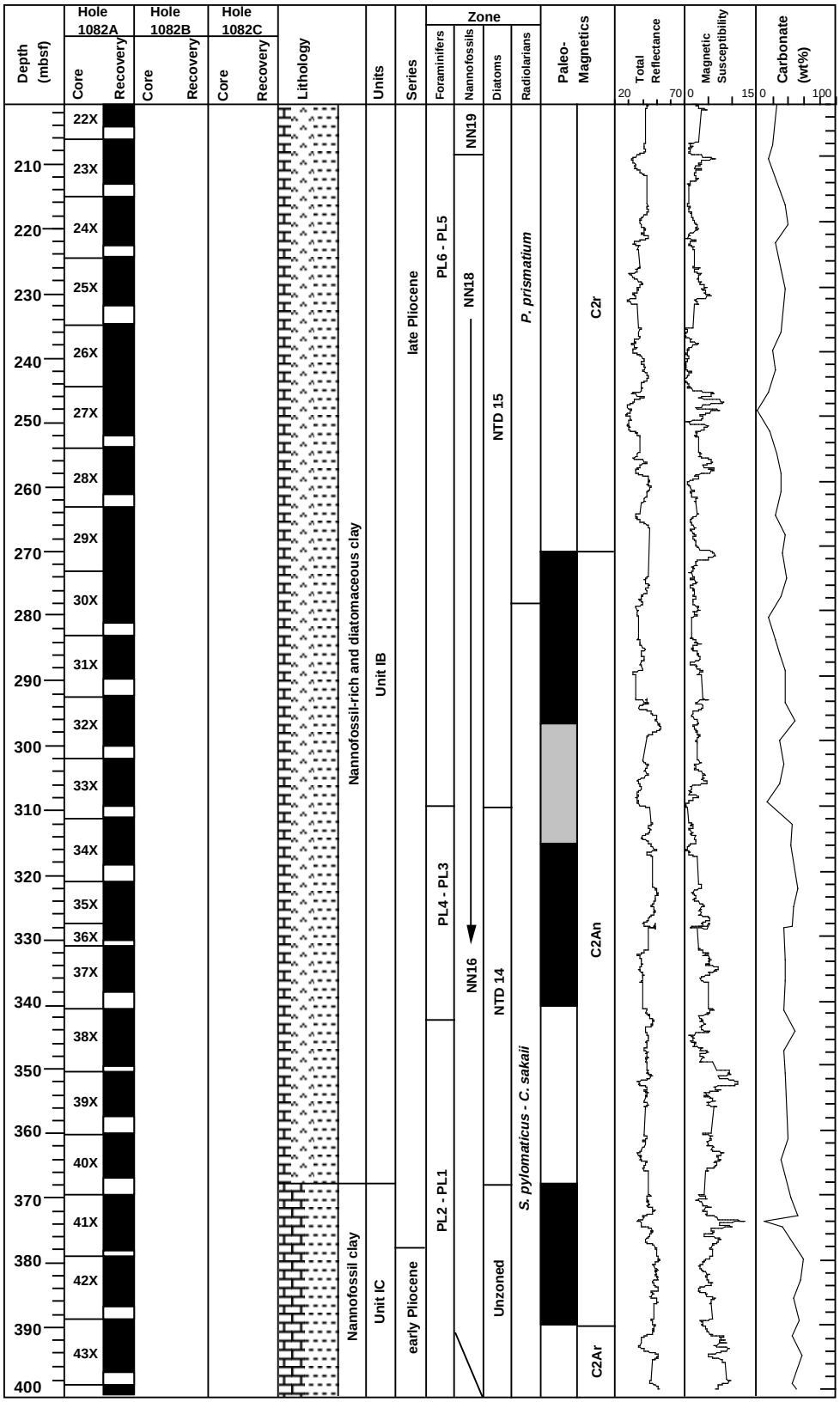

Figure 1 (continued).

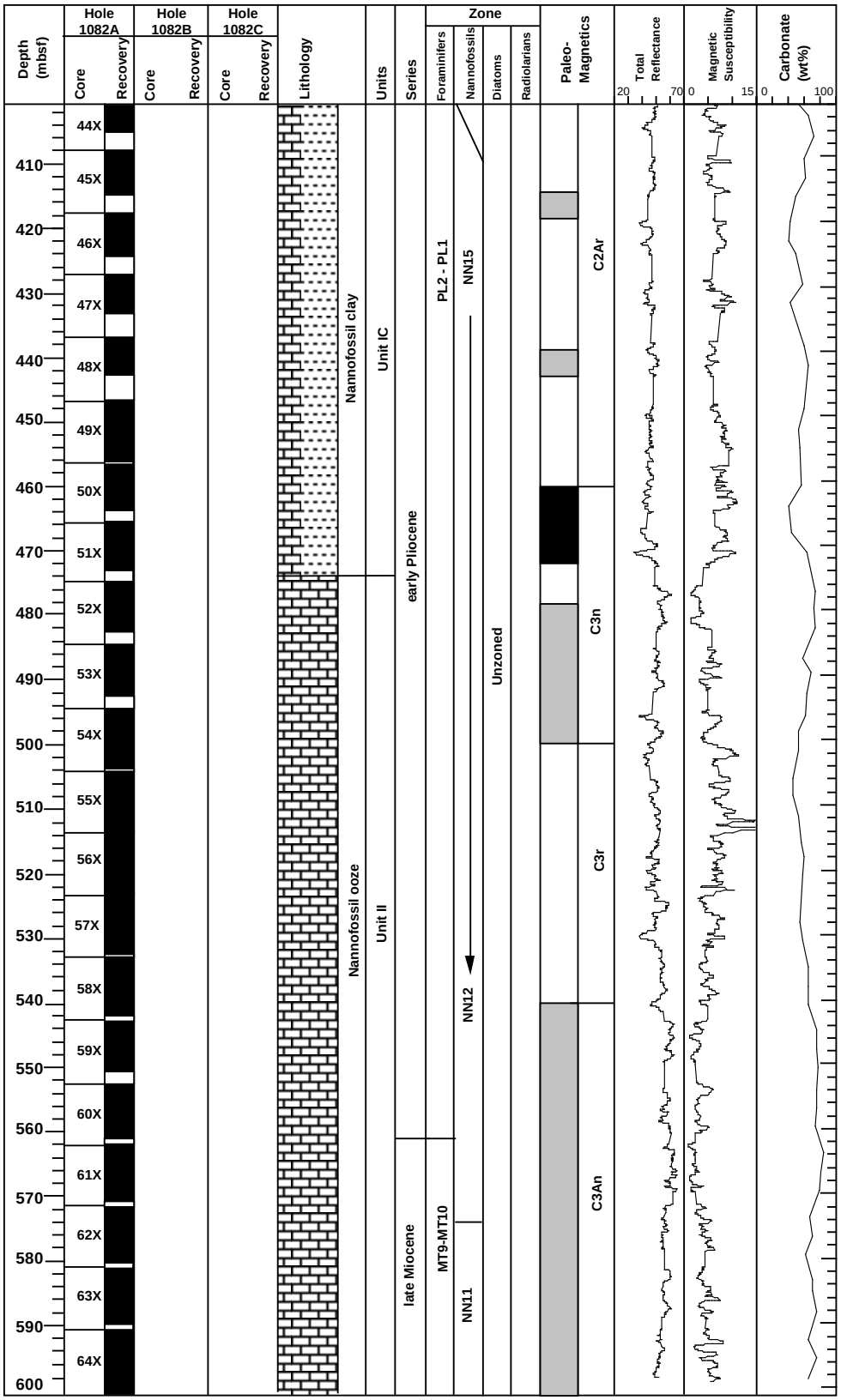

Figure 1 (continued).

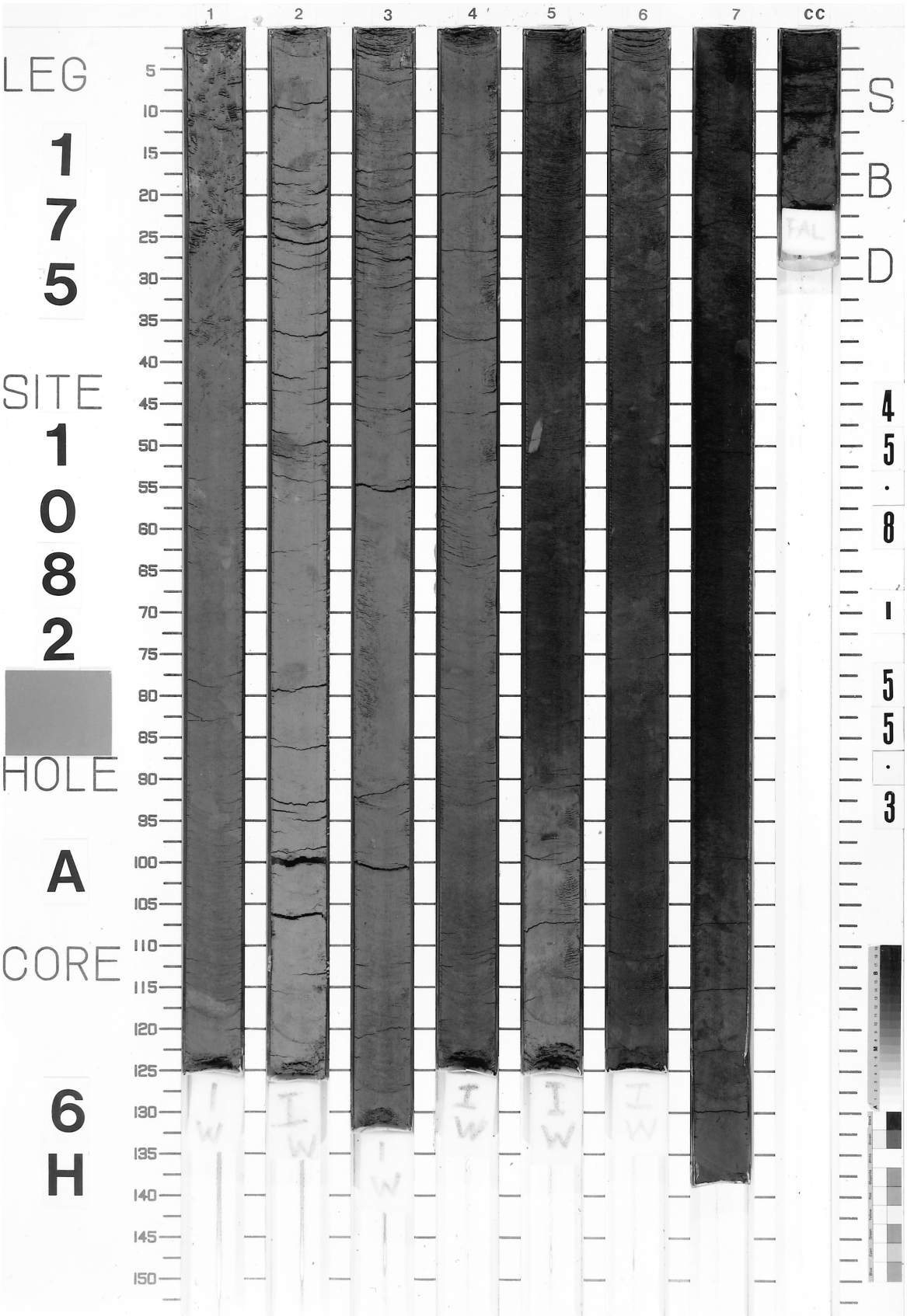

Figure 2. Photograph of color changes in Core 175-1082A-6H.

Subunit IC is composed of intercalated intervals of pale yellow (5Y 7/4), olive (5Y 4/3), and dark olive-gray (5Y 3/2) nannofossil-rich clay and nannofossil clay. Concentrations of calcium carbonate are high and average 51 wt%, whereas concentrations of organic carbon are lower than in Subunit IB, averaging 4 wt%. The contact with Unit II is marked by a significant increase in nannofossil abundance and is gradational over tens of meters. The boundary between the nannofossil clays and nannofossil oozes of Unit II occurs between Cores 175-1082A-51X and 52X (475 mbsf).

Unit II

Interval: 175-1082A-52X through 175-1082A-63X
Age: Miocene
Depth: 475–590 mbsf

Unit II is composed of olive (5Y 4/3) to olive-gray (5Y 4/2) nannofossil ooze. Unit II has high calcium carbonate contents, which average 67 wt%, but low organic carbon contents, which average 2 wt%.

Synthesis of Smear-Slide Analyses

Smear-slide analyses indicate that the detrital component of the sediments in all units and subunits consists of clay with rare silt-sized, angular and subangular feldspar and mono- and polycrystalline quartz grains. Muscovite and biotite are present in trace amounts. The grain size of identifiable detrital components is generally constant throughout all lithostratigraphic units. The relative proportion of detrital to biogenic particles is relatively constant throughout Unit I. The clastic fraction dominates Unit I, whereas biogenic carbonates are the most abundant component in Unit II. Authigenic minerals, such as glauconite and framboidal pyrite, are either rare or present in trace amounts only. Dolomite rhombs are observed in both Subunits IB and IC. The biogenic component is represented by varying abundances of foraminifers (whole and fragments), nannofossils, diatoms, radiolarians, sponge spicules, and silicoflagellates.

Smear-slide analyses of sediment from Subunit IA revealed abundant to common foraminifer fragments, common to very abundant nannofossils, rare siliceous sponge spicules, and trace amounts of radiolarians. Diatom abundances vary from common to barren. The relative abundances of the biogenic components change frequently within one core. Individual intervals are between 30 and 250 cm thick. The intercalated dark olive-brown and black clay intervals have distinctly lower abundances of biogenic components and occasionally show higher abundances of silt-sized mono- and polycrystalline quartz grains. The darkest layer shows amorphous brown aggregates of organic matter and is completely barren of microfossils.

In Cores 175-1082A-13H through 21X of Subunit IB, the abundances of diatoms are high, whereas nannofossils and foraminifer fragments are less abundant than those of Subunit IA. In Core 175-1082A-22X, nannofossil-rich sedimentary intervals are more frequent, and the abundances of nannofossils steadily increases in all the subsequent stratigraphically deeper intervals. Diatoms remain common down to Core 175-1082A-39H, below which they become rare. Foraminifer fragments are rare to common throughout Subunit IB but disappear at the bottom of this subunit. Radiolarians are present in trace amounts.

In Subunit IC, large carbonate aggregates become common components in all smear slides. These carbonates are most likely derived from the dissolution and recrystallization of foraminifer fragments and nannofossils. Nannofossils are the most abundant biogenic component in this subunit. Foraminifers are present in rare to trace abundances, whereas diatoms are largely absent. The transition to Unit II is marked by the depth below which nannofossils become the most abundant component in the smear slides.

Of all the sediments recovered from Site 1082, Unit II has the highest abundances of nannofossils. This unit also exhibits the smallest compositional variability. In addition to nannofossils, biogenic components include rare to frequent diatoms, siliceous spicules, foraminifers, and trace amounts of radiolarians. Recrystallized carbonate aggregates are common. In this unit, the detrital component is less abundant than the biogenic component, and angular quartz grains are present only in trace amounts.

X-ray Diffraction Analysis

X-ray diffraction (XRD) analysis of the upper 400 m of sediments from Hole 1082A reveals that the clastic fraction is dominated by the clay minerals smectite, kaolinite, illite, and muscovite (mica). Quartz, microcline, and albite are also major constituents in the clastic fraction. Pyrite is the only sulfide mineral identified as an accessory phase. Dolomite is identified in the lithified clay horizons. Detected spacings of dolomite indicate slightly larger crystal lattices and suggest a nonstoichiometric dolomite composition with slight relative calcium enrichment. The dolomite horizon at 327 mbsf (Sample 175-1082A-36X-1, 0–1 cm) contains 35 wt% dolomite (see "Organic Geochemistry" section, this chapter). Sediments adjacent to the dolomite horizon contain only trace amounts of dolomite. The detected biogenic components are calcite and opal. Calcite peak intensities are strongly correlated to measured calcium carbonate concentrations (r = 0.98). Opal concentrations were estimated from the height of the amorphous opal bulge according to the method of Eisma and van der Gaast (1971); the opal data are only qualitative because no standard opal sample for calibration was available on board. The

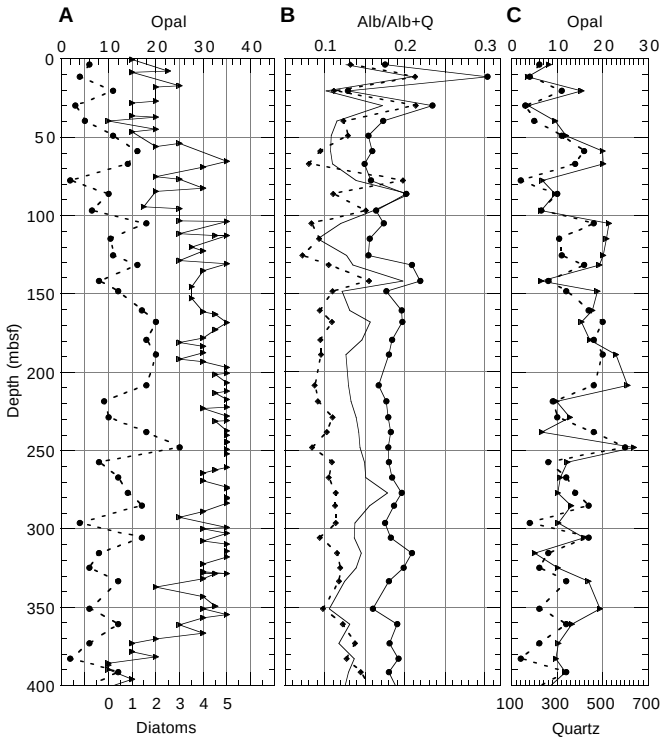

Figure 3. Mineral and opal data for the upper 400 m of Hole 1082A. **A.** Opal XRD counts (dashed line) compared with diatom abundance (solid line; see "Biostratigraphy and Sedimentation Rates" section, this chapter). **B.** Ratios of albite (solid line with filled circles), microcline (solid line), and muscovite to quartz (mineral/[mineral+quartz]; dashed line). **C**. Opal (dashed line) and quartz (XRD counts; solid line).

general trends in opal abundances reflect the variation in diatom abundance curves in Hole 1082A (Fig. 3A).

The downcore variations in intensity of quartz and opal are weakly negatively correlated with calcium carbonate (Fig. 4), as is also true for the feldspars and muscovite. The variations, however, are too large to be explained by differences in dilution by carbonate alone. To exclude this dilution effect, we compared the ratios of the minerals relative to quartz. In the upper part of the core, the amplitudes increase in two phases, and the correlations decrease in two steps: the first around 150 mbsf and the second around 40 mbsf.

The fine silt size of quartz and feldspar, as observed from the smear slides, may indicate an eolian origin. Muscovite originates from the southern Namib Desert (Jansen and van der Gaast, unpubl. data). The correlation of quartz intensities with opal (Fig. 3C) suggest that the minerals reflect a climatic system in which the force of the southeast trade winds controls both the upwelling and the eolian input. In the vicinity of the Pliocene/Pleistocene boundary (~155 mbsf), the various contributions of the eolian components started to become decoupled, which implies that the character of the transport mechanisms or the source areas must have changed. A similar change occurred around 400 ka (40 mbsf) when a second increase in amplitude took place. Both transitions are also reflected in the sediments of Hole 1081A from the Walvis Ridge (see "Lithostratigraphy" section, "Site 1081" chapter, this volume).

Spectrophotometry

General Trends

Color data were measured every 2 cm for Cores 175-1082A-1H through 9H. Cores 175-1082A-10H through 49X and all of Holes 1082B and 1082C were measured at 4-cm intervals. At Site 1082, total reflectance values range between 25% and 65% (Figs. 5, 6).

The general trends in total reflectance, calcium carbonate, and magnetic susceptibility can be correlated to the lithostratigraphic subunits of Hole 1082A (Fig. 5). Higher values in the total reflectance are observed in the nannofossil-rich clay of Subunits IA and IB

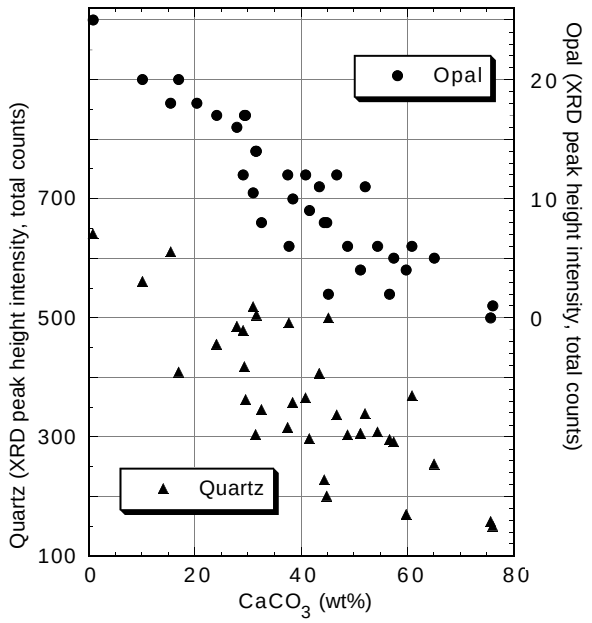

Figure 4. Crossplot of quartz and opal intensities (XRD counts) to calcium carbonate concentrations (see "Organic Geochemistry" section, this chapter) for the upper 400 m of Hole 1082A.

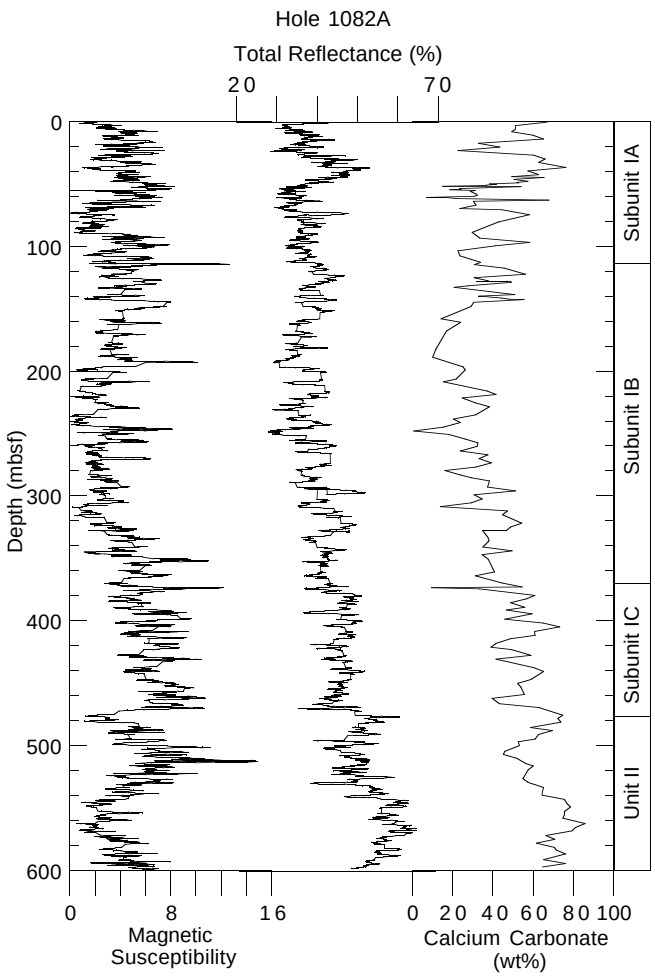

Figure 5. Stratigraphic variation in the total reflectance, calcium carbonate, and magnetic susceptibility at Hole 1082A. Lithostratigraphic subunits are indicated.

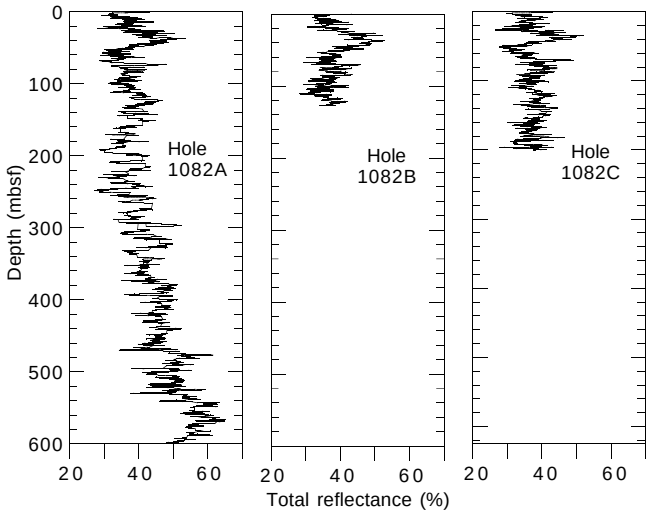

Figure 6. Stratigraphic variation in the total reflectance at Holes 1082A, 1082B, and 1082C.

as well as in Unit II, whereas lower values are associated with the diatom-rich clay of Subunit IB. Downcore variations in the total reflectance are positively correlated to the calcium carbonate content. This suggests that calcium carbonate controls the total reflectance of the sediment in the diatom-rich intervals. The negative correlation between total reflectance and magnetic susceptibility indicates the dilution of the clay component by the carbonate component.

Total reflectance records for the three holes at Site 1082 are very similar (Fig. 6). Sediment recovered in the upper 200 mbsf at Holes 1082A, 1082B, and 1082C is of Pleistocene age (see "Biostratigraphy and Sedimentation Rates" section, this chapter) and has high total reflectance values, with a maximum of 55% at about 40 mbsf. This depth interval corresponds to marine oxygen-isotopic Stages 9, 10, and 11 (see "Biostratigraphy and Sedimentation Rates" section, this chapter) and may be caused by better preservation of the carbonate shells and/or enhanced carbonate productivity. Higher total reflectance values are also observed at all three holes at the Brunhes/Matuyama magnetic reversal (76 mbsf; see "Paleomagnetism" section, this chapter) and appear to correspond to marine oxygen-isotopic Stage 19.

Fine-Scale Variations

Cores 175-1082A-5H through 7H contain several dark olive-brown and black clay layers intercalated in the pervasive olive-gray and olive clays (Fig. 2). In general, the bottom of the dark olive-brown layers is very sharp, whereas the upper boundary is gradational because of extensive bioturbation. The color cycles reflect sharp changes in concentrations of calcium carbonate, organic carbon, and total sulfur (Fig. 7A). The dark layers have high concentrations of organic carbon and total sulfur and low concentrations of calcium carbonate and biogenic opal. Over this depth interval, calcium carbonate is inversely related to organic carbon and total sulfur. The variation in total reflectance corresponds closely to changes in calcium carbonate content (Fig. 7B). These data strongly suggest that in these sediments the abundance of calcium carbonate exerts the strongest influence on total reflectance. This effect is further accentuated by the strong negative correlation between calcium carbonate and organic carbon, as high contents of organic carbon tend to decrease the total reflectance of sediments.

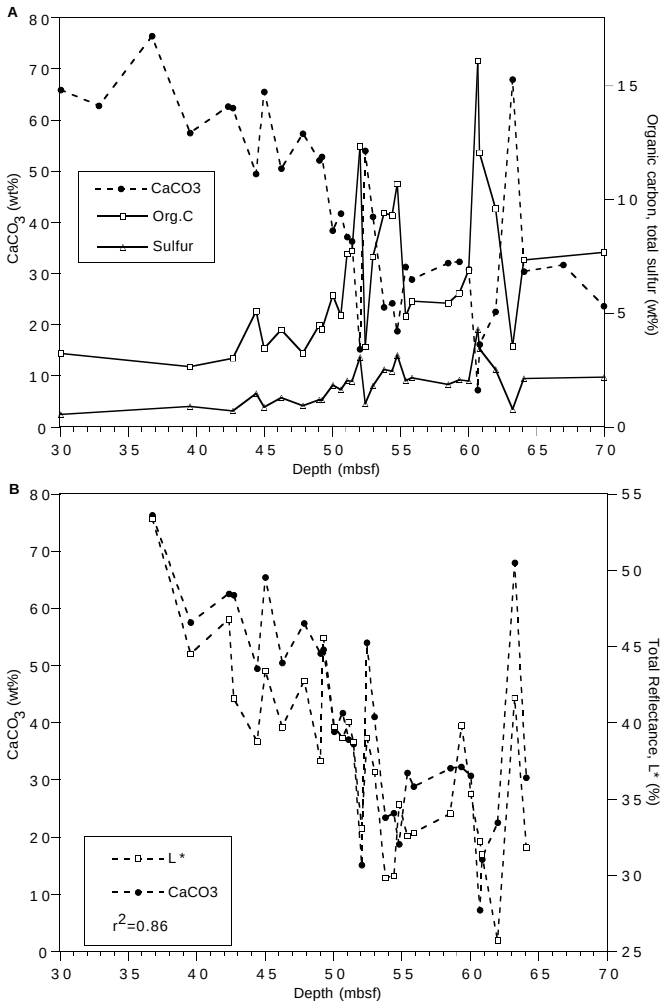

Figure 7. **A**. Depth variation in concentrations of organic carbon, calcium carbonate, and total sulfur for light and dark sediments for Cores 175-1082A-5H through 175-1082A-7H. **B**. Depth variation in concentrations of calcium carbonate content and total reflectance.

BIOSTRATIGRAPHY AND SEDIMENTATION RATES

Sediments recovered from Site 1082 represent a relatively continuous hemipelagic section spanning approximately the last 5.7 m.y. The micropaleontological studies were carried out on core-catcher samples from Hole 1082A. Additional samples from within the cores were examined to improve the biostratigraphic resolution. An integrated biostratigraphic framework composed of both calcareous and siliceous microfossils was established (Fig. 8, Table 2), resulting in a well-constrained age model for Site 1082. Sedimentation rates range from 7 to 20 cm/k.y. They are highest within the upper part of the upper Pliocene sediments as well as the lower part of the lower Pliocene sediments. A disturbed sequence resulting in an altered stratigraphic interval is identified between ~70 and 110 mbsf. Unlike at previous sites, preservation of calcareous microfossils is good throughout most of Site 1082. Siliceous microfossils indicate a subantarctic influence off Namibia during the late Pliocene.

Calcareous Nannofossils

Calcareous nannofossils were studied in core-catcher samples from Hole 1082A. Additional samples from within the cores were examined close to datum events to improve the stratigraphic resolution. Overall abundance ranges from abundant to very abundant within the entire section. A few samples are barren or poor in nannofossils either near an epoch boundary (Sample 175-1082A-19X-CC, close to the Pliocene/Pleistocene boundary) or within dolomite-rich layers (e.g., Sample 175-1082A-42X-CC). Preservation is moderate to poor between 170 and 250 mbsf in the upper part of the upper Pliocene sediment. Below and above this sequence, preservation is good to very good.

Site 1082 terminated in the uppermost upper Miocene sediment within Zone NN11. Based on the oldest identified datum, the bottom age is estimated at 5.8 ± 0.2 Ma. Within the sampling resolution, the sedimentation appears continuous throughout the entire section (Fig. 8). However, the absence of the index assemblage for the Small *Gephyrocapsa* acme interval (Gartner, 1977) between the last occurrences (LOs) of *Reticulofenestra asanoi* and *Helicosphaera sellii* probably points to a disturbed sequence from 70 to 115 mbsf.

Because of the scarcity of the Neogene *Discoaster, Amaurolithus, Ceratolithus,* and *Triquetrorhabdulus* index species, the nannofossil-based biostratigraphy for the Pliocene and upper Miocene parts of Site 1082 is constrained by three biohorizons only. Consequently,

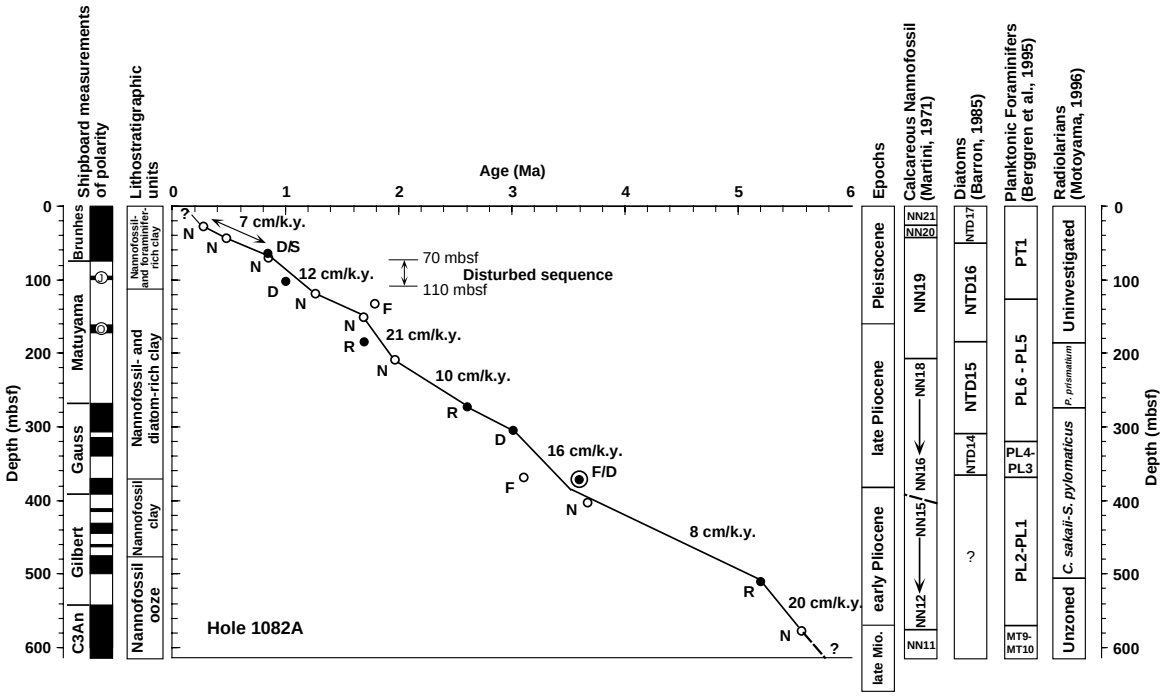

Figure 8. Age-depth plot and sedimentation rates estimated from calcareous microfossil (open circles; F = foraminifers and N = calcareous nannofossils) and siliceous microfossil (solid circles; D = diatoms, R = radiolarians, and S = silicoflagellates) datums at Hole 1082A.

Table 2. Microfossil datums at Hole 1082A.

Fossil group	Event	Age (Ma)	Zone (base) A	Zone (base) B	Core, section, interval (cm) Top	Core, section, interval (cm) Bottom	Depth (mbsf) Top	Depth (mbsf) Bottom	Depth (mbsf) Mean
					175-1082A-	175-1082A-			
N	FO *Emiliania huxleyi*	0.26	NN21a	CN15	3H-5, 100	3H-CC	23.90	27.16	25.53
N	LO *Gephyrocapsa caribbeanica* acme	0.26	NN21a	CN15	3H-5, 100	3H-CC	23.90	27.16	25.53
N	LO *Pseudoemiliania lacunosa*	0.46	NN20	CN14b	5H-3, 10	5H-5, 120	39.20	43.10	41.15
S	LO *Bachmannocena quadrangula*	0.80			6H-CC	7H-CC	55.82	65.47	60.65
N	LO *Reticulofenestra asanoi*	0.83			7H-CC	8H-5, 10	65.47	69.61	67.54
D	LO *Nitzschia fossilis*	0.92			6H-CC	7H-CC	55.82	65.47	60.65
D	LO *Rhizosolenia matuyama*	1.10			10H-CC	11H-CC	94.34	103.45	98.90
N	LO *Helicosphaera sellii*	1.25			13H-3, 80	13H-6, 20	115.22	118.86	117.04
D	LO *Rhizosolenia praebergonii* var. *robusta*	1.65			20X-CC	21X-CC	183.51	193.47	188.49
N	LO *Calcidiscus macintyrei*	1.67			16X-CC	17X-CC	145.34	152.80	149.07
D	LO *Proboscia barboi*	1.68			19H-CC	20H-CC	172.74	183.51	178.13
R	LO *Cycladophora pliocenica*	1.83			20X-CC	21X-CC	183.51	193.47	188.49
N	LO *Discoaster brouweri*	1.95	NN19	CN13a	22X-CC	23X-CC	201.31	213.19	207.25
D	LO *Thalassiosira convexa*	2.19			27X-CC	28X-CC	252.12	262.14	257.13
R	FO *Cycladophora davisiana*	2.70			29X-CC	30X-CC	273.16	280.53	276.85
D	FO *Rhizosolenia praebergonii*	3.12			34X-1, 40	34X-2, 100	312.10	314.20	313.15
N	LO *Sphenolithus* spp.	3.66			43X-CC	44X-CC	396.06	405.07	400.57
R	FO *Spongorus pylomaticus*	5.20			54X-CC	55X-CC	503.56	513.60	508.58
N	LO *Discoaster quinqueramus*	5.54	NN12	CN10a	61X-CC	62X-CC	570.48	579.77	575.13

Notes: Fossil group: N = calcareous nannofossils; S = silicoflagellates; D = diatoms; and R = radiolarians. FO = first occurrence and LO = last occurrence. Zonal codes refer to the standard calcareous nannofossil zonations of (A) Martini (1971) and (B) Okada and Bukry (1980).

Zones NN18 down to NN16, as well as Zones NN15 down to NN12, are lumped into two coarse biostratigraphic intervals.

Zone NN21

The Subzone NN21b, which describes the last 0.09 m.y., was not recognized in the uppermost core of Site 1082. The 0.26 Ma datum event (Zone NN21/NN20 boundary) was identified at the mean depth of 25.5 mbsf between Samples 175-1082A-3H-5, 100 cm, and 3H-CC.

Zone NN20

This interval of 0.2-m.y. duration terminates at 41.1 mbsf (between Samples 175-1082A-5H-3, 10 cm, and 5H-5, 120 cm), which is the mean depth of the LO of the *Pseudoemiliania lacunosa* datum event.

Zone NN19

In addition to the zonal boundary events, three biohorizons were identified within this interval. These are the LO of *Reticulofenestra*

asanoi (0.83 Ma) at 67.5 mbsf; LO of *Helicosphaera sellii* (1.25 Ma) at 117 mbsf; and LO of *Calcidiscus macintyrei* (1.67 Ma) at 149 mbsf. The highest Pleistocene accumulation rates (>12 cm/k.y.) for Site 1082A are found within the upper part of this zone. As discussed above, the suggested presence of a disturbed sequence between 70 and 115 mbsf might explain this change in accumulation rate pattern.

Zones NN18, NN17, and NN16

The top of Zone NN18 is defined by the disappearance of the last *Discoaster* species, *D. brouweri* (between Samples 175-1082A-22X-CC and 23X-CC). This species is found consistently within the Neogene interval of Hole 1082. A single specimen of *D. pentaradiatus*, the marker species for the Zone NN18/NN17 boundary, was identified in Sample 28X-CC, therefore providing a minimum age of 2.45 Ma for the associated core depth (262 mbsf). *Reticulofenestra pseudoumbilica*, whose LO defines the Zone NN16/NN15 boundary (3.82 Ma), is commonly found as reworked within the lower half of the Zone NN18-NN17-NN16 part of Site 1082A. The LO of *Sphenolithus* spp.(between Samples 175-1082A-43X-CC and 44X-CC), a synchronous event dated at 3.66 Ma (lowermost part of Zone NN16), is therefore used at Site 1082 to approximate the Zone NN16/NN15 boundary.

Zones NN15, NN14, NN13, and NN12

This interval extends from 3.84 to 5.54 Ma. Although the sparse occurrence of index species prevents us from identifying biohorizons, some investigated samples can be confidently placed within more restricted stratigraphic intervals. Samples 175-1082A-50X-CC through 52X-CC contain common specimens of *A. delicatus (*LO within Zone NN13), with sparse occurrences of *D. pansus* and *A. tricorniculatus* (range: Zones NN14, NN13, and NN12). These samples, therefore, belong to Zones NN13 and/or NN12 (5.02–5.54 Ma). Sample 175-1082A-53X-CC contains sparse *C. armatus*, a species with a range restricted to Zone NN12 (5.23–5.54 Ma).

Zone NN11

The Zone NN12/NN11 boundary is defined by the LO of *D. quinqueramus*, a datum identified near the base of Hole 1082A between Samples 175-1082A-61X-CC and 62X-CC. *D. berggrenii*, the synonym species to *D. quinqueramus*, is present in Sample 175-1082A-63X-CC, thereby confirming the stratigraphic position of the bottom cores of Hole 1082A.

Planktonic Foraminifers

Analysis of planktonic foraminifers indicates that a relatively continuous uppermost Miocene to Pleistocene section was recovered. Foraminifers are generally common to abundant in the Pleistocene sediments and common in the lower Pliocene sediments; however, the upper Pliocene sediments have low abundance or are barren. Trace amounts of *Globorotalia inflata* dominate the fauna between Samples 175-1082A-15X-CC and 40X-CC. Although dissolution affects abundance at Hole 1082A, the overall foraminiferal abundances are higher than at Site 1081, which contains long intervals that are either barren or contain only pyritized planktonic foraminifers. The zonation is coarse because of the generally low abundance of tropical to subtropical species that are used to define the Pliocene zonations and because of dissolution.

The uppermost sample (175-1082A-1H-CC, 7.8 mbsf) is dominated by *Globigerina bulloides* and *Globorotalia inflata*. *Orbulina universa* is abundant, and *Globoratalia truncatulinoides*, *Globigerinella siphonifera*, *Globigerina quinqueloba*, and *Neogloboquadrina pachyderma* (sinistral and dextral) are present (Table 3). *G. bulloides* and *G. inflata* are the dominant components of the assemblage within Sample 175-1082A-8H-CC and indicate upwelling, although downcore faunal variations indicate that warm surface water (Angola Current) penetrated the region in the past. For example, the tropical-warm subtropical species *Globorotalia crassaformis* and *Globorotalia menardii* are present in Sample 175-1082A-4H-CC (Table 3). This surface-water warming is associated with a decrease in upwelling, as indicated by a reduced abundance of *G. bulloides* in this sample.

Table 3. Relative abundance, presence or absence, and overall abundance of Pleistocene planktonic foraminifers at Hole 1082A.

Core, section, interval	Depth (mbsf)	Overall abundance	*Orbulina universa*	*Globigerina bulloides*	*Globorotalia inflata*	*Neogloboquadrina pachyderma* (dextral)	*Globorotalia crassaformis*	*Globorotalia truncatulinoides*	*Globorotalia tosaensis*	*Globorotalia scitula*	*Globorotalia menardii*	*Neogloboquadrina dutertrei*	Dissolution
175-1082A-													
1H-CC	7.8	5	A	D	D			P					5
2H-CC	17.4	5	A	A	A	A		P				P	5
3H-CC	27.2			D	D								
4H-CC	36.7		A	A	D			P		P		P	
5H-CC	46.5	4		A	D			P				P	5
6H-CC	55.8	5		D				P				P	5
7H-CC	65.5	5		A	D			P					5
8H-CC	75.3	5		D	D					P			5
14H-CC	128.6	5	A	A			A	P	P	P	P		5
15X-CC	135.3	2			D								3
16X-CC	145.3	3	A	A	D								4

Notes: D = dominant (>30%) and A = abundant (10%–30%) components of the assemblage are shown. Presence (P) and absence (A) are also shown for select species. Overall abundance is given as 2 = rare; 3 = few; 4 = common; and 5 = abundant. Dissolution is grouped as 2 = some dissolution; 4 = moderate dissolution; and 5 = no dissolution.

The detection of the upper Pliocene/lower Pleistocene and lower/upper Pliocene boundaries was complicated by dissolution. The samples at the boundaries (as determined by other fossil groups) are barren of foraminifers; however, the samples above and below the boundaries, although affected by dissolution, contain sufficient specimens to evaluate the zonations of the other microfossil groups.

The Pliocene/Pleistocene boundary is generally recognized by the first-appearance datum (FAD) of *G. truncatulinoides*. This FAD occurs in Sample 175-1082A-14H-CC (128.6 mbsf); however, the overall abundance is low in Samples 175-1082A-15X-CC through 20X-CC, and the fauna is dominated by the dissolution-resistant foraminifer *G. inflata*. The absence of *G. truncatulinoides* in Samples 15X-CC through 20X-CC, therefore, may be the result of dissolution, and so *G. truncatulinoides* is not a reliable marker for the boundary at this site. Calcareous nannofossil and paleomagnetic data place the boundary in Core 19H.

Abundance is low in Samples 175-1082A-15X-CC through 26X-CC, but it increases in Sample 175-1082A-27X-CC (252.1 mbsf) in association with a lithologic change. *G. bulloides* is present within a warm-water fauna (e.g., *G. ruber* and *O. universa*). Abundance decreases again in Sample 175-1082A-28X-CC, as does diversity. The fauna in Samples 28X-CC through 30X-CC is nearly monospecific in the >250-µm fraction (*G. inflata* dominates) and barren in the 150- to

250-µm fraction, suggesting dissolution. Sample 175-1082A-31X-CC is barren.

Pliocene sediments from Site 1082 are difficult to zone because many of the index species are not present. Samples 175-1082A-27X-CC through 34X-CC (252.1–317.7 mbsf) are middle to upper Pliocene sediments, based on the presence of *G. crassaformis viola* and the absence of *G. truncatulinoides*. *G. crassaformis viola* is present in Sample 27X-CC through 34X-CC and ranges from Zone N21 to early Zone N22 (Kennett and Srinivasan, 1983). Zones N21–N22 of Blow (1969) are approximately correlative with Zones PL5, PL6, and early Pt1 of Berggren et al. (1995). The evolutionary first appearance (FO) of *G. inflata* occurs in the North Atlantic at 2.3 Ma, although it has been recorded earlier in the Southern Ocean (at ~3.4 Ma; see Brunner, 1991), and provides a possible means of further differentiating the zonation. The FO of *G. inflata* occurs in Sample 34X-CC (317.7 mbsf). If the FAD is at 2.3 Ma, this limits Sample 34X-CC to Zone PL6. If the earlier FO in the Southern Ocean is, however, at 3.4 Ma and is not caused by drilling disturbance or some other form of reworking (Brunner, 1991), then Sample 34X-CC can be constrained to Zones PL5 or PL6 based on the presence of *G. crassaformis viola*. Other species present in this interval include *N. pachyderma*, *G. acostaensis*, *G. puncticulata*, and *G. crassaformis crassaformis*.

The lower/upper Pliocene boundary is difficult to identify at this site. *Dentoglobigerina altispira*, *Globorotaloides hexagona*, *Gs. extremus*, and *Gs. apertura* are present in Sample 175-1082A-40X-CC (366.5 mbsf), which constrains the age to late Miocene–late Pliocene. The first definite appearance of *G. margaritae* (lower Pliocene) is in Sample 175-1082A-41X-CC (378.3 mbsf), although there is a transitional form in Sample 40X-CC (366.5 mbsf). Thus, the boundary between the early (Zones PL1 and PL2) and late (Zones PL3–PL6) Pliocene occurs above Sample 41X-CC (378.3 mbsf). The occurrence of *G. theyeri* (early Pliocene) provides further evidence that Sample 41X-CC is restricted to early Pliocene Zones PL1 and PL2. The FO of *G. margaritae* occurs in Sample 175-1082A-61X-CC (570.48 mbsf), indicating that the sample is of early Pliocene age. *G. cibaoensis* (late Miocene to early Pliocene) is also present in that sample.

The Pliocene/Miocene boundary is placed between Samples 175-1082A-62X-CC and 61X-CC. Sample 62X-CC is assigned to the Miocene Zones N16–N19 based on the presence of *G. nepenthes* (Zones N14–N19), *G. extremus* (Zones N16–N21), and *N. acostaensis* (Zones N16–N20). Although Zones N16–19 of Blow (1969) are correlative with Zones Mt 9, Mt10, and PL1 of Berggren et al. (1995), the absence of *G. margaritae* (ZOne PL1) restricts Samples 62X-CC and 175-1082A-63X-CC to Zones Mt9 and Mt10. The presence of *G. conoidea* in Sample 63X-CC is in agreement with the late Miocene zonation.

Benthic Foraminifers

Sediments recovered from Hole 1082A contain abundant benthic foraminifers throughout (Table 4, back-pocket foldout, this volume). The preservation is good throughout, except for a few samples that exhibit moderate to good preservation. Two samples (175-1082A-42X-CC (386.97 mbsf) and 48X-CC (442.70 mbsf)) were lithified; consequently, the benthic foraminifers could not be counted.

The benthic foraminiferal fauna shows high diversity throughout Hole 1082A. The uppermost core catcher (Sample 175-1082A-1H-CC; 7.84 mbsf) is dominated by *Bulimina aculeata* (–40%) and contains *Bulimina exilis*, *Cassidulina laevigata*, and *Uvigerina auberiana* (Table 4; Fig. 9). *Bulimina aculeata* shows very low abundance farther downhole, except for two peaks (Samples 175-1082A-15X-CC [135.30 mbsf; –18%] and 20X-CC [183.51 mbsf; –32%]).

The uppermost lithostratigraphic Subunit IA (nannofossil and foraminifer-rich clay; see "Lithostratigraphy" section, this chapter) between 0 and 112 mbsf is characterized by high relative abundances of *Bulimina marginata*, *Uvigerina hispidocostata*, *Cassidulinoides* cf. *bradyi*, *Cassidulina laevigata*, and the *Praeglobobulimina/Globobulimina* group (Table 4; Fig. 9). These species are more or less restricted to lithostratigraphic Subunit IA, whereas *Bulimina exilis*, which is a significant contributor to this faunal assemblage, also occurs farther down in the section.

Lithostratigraphic Subunit IB (diatom-rich clay) covers the interval between 369 and 112 mbsf and is dominated by *Bulimina exilis* and *Uvigerina auberiana*. Other significant species are *Globocassidulina subglobosa*, *Pullenia bulloides*, *Bulimina mexicana*, *Cibicidoides wuellerstorfi*, and *Gavelinopsis lobatulus* (Table 4; Fig. 9). Most of these species are more or less absent in the lithostratigraphic unit above but present in the underlying lithostratigraphic units—except for *Globocassidulina subglobosa*, which seems to be restricted to lithologic Subunit IB. Some species have short-term peaks in their relative abundance within this lithostratigraphic unit and are more or less absent elsewhere: *Bulimina truncana* shows a single peak (–32%) right at the top of this unit (128.58 mbsf); the genus *Stilostomella* has peaks at 112.84 mbsf (–73%) and 280.53 mbsf (–59%); and *Uvigerina hispida* has a peak at 328.60 mbsf (–8%; see Table 4; Fig. 9).

Lithostratigraphic Subunit IC (nannofossil clay, 475–369 mbsf) and Unit II (nannofossil ooze; bottomhole, 475 mbsf) contain similar benthic foraminiferal assemblages. The dominant species is *Bolivina subaenarensis* with contributions from *Sigmoilinopsis schlumbergeri*, *Melonis barleeanum*, *Sphaeroidina bulloides*, *Bulimina mexicana*, and *Cibicidoides bradyi* (Table 4; Fig. 9). The species *Cibicidoides pachyderma* and *Epistominella exigua* are essentially restricted to lithostratigraphic Unit II.

Radiolarians

Core-catcher Samples 175-1082A-18X-CC through 64X-CC were examined for radiolarians to assess the Pliocene to Miocene biostratigraphy. Radiolarians are present in most of the samples from Hole 1082A (Table 5). In the upper sequence (18X-CC through 40X-CC), radiolarians are generally abundant and well preserved. In the lower sequence (41X-CC through 64X-CC), radiolarians are rare and show signs of dissolution, although it was possible by the sample preparation to concentrate the sample enough to produce high abundances of radiolarians in the assemblage slides. Radiolarian fauna indicates an early Pleistocene to late Miocene age for the investigated sequence. No apparent reworking has been identified.

The radiolarian zones used for this hole are those of Moore (1995) and Motoyama (1996). There are some difficulties in applying the established tropical and Antarctic zonations (Sanfilippo et al., 1985; Lazarus, 1992) because of the absence of index species such as *Pterocanium prismatium*, *Spongaster pentas*, *Diartus hughesi*, *Helotholus vema*, and *Amphymenium challengerae*. The radiolarian faunas are similar to those from time-equivalent samples from Hole 1081A.

Although the diagnostic species *Anthocyrtidium angulare* and *P. prismatium* are absent throughout the core, Samples 175-1082A-18H-CC, 19X-CC, and 20X-CC are approximately assigned to the Pleistocene *A. angulare* Zone of Moore (1995) based on the presence of *Lamprocyrtis neoheteroporos* and the absence of *Cycladophora pliocenica*, which became extinct at 1.78 Ma in the Antarctic Ocean (Caulet, 1991).

The LO of *C. pliocenica* is placed in Sample 175-1082A-21X-CC, approximating the Pliocene/Pleistocene boundary between Samples 20X-CC and 21X-CC; thus, the upper boundary of the *A. angulare* Zone, originally defined by the LO of *P. prismatium*, should be placed at about Sample 21X-CC.

The FO of *Cycladophora davisiana*, in Sample 175-1082A-29X-CC, indicates an age of 2.7 Ma and the lower boundary of the *P. prismatium* Zone.

Spongorus pylomaticus first occurs in Sample 175-1082A-54X-CC, giving an age of 5.2 Ma and a Miocene/Pliocene boundary for the horizon just below this sample. Samples 175-1082A-21X-CC through 54X-CC, which are below the FO of *C. davisiana* and above

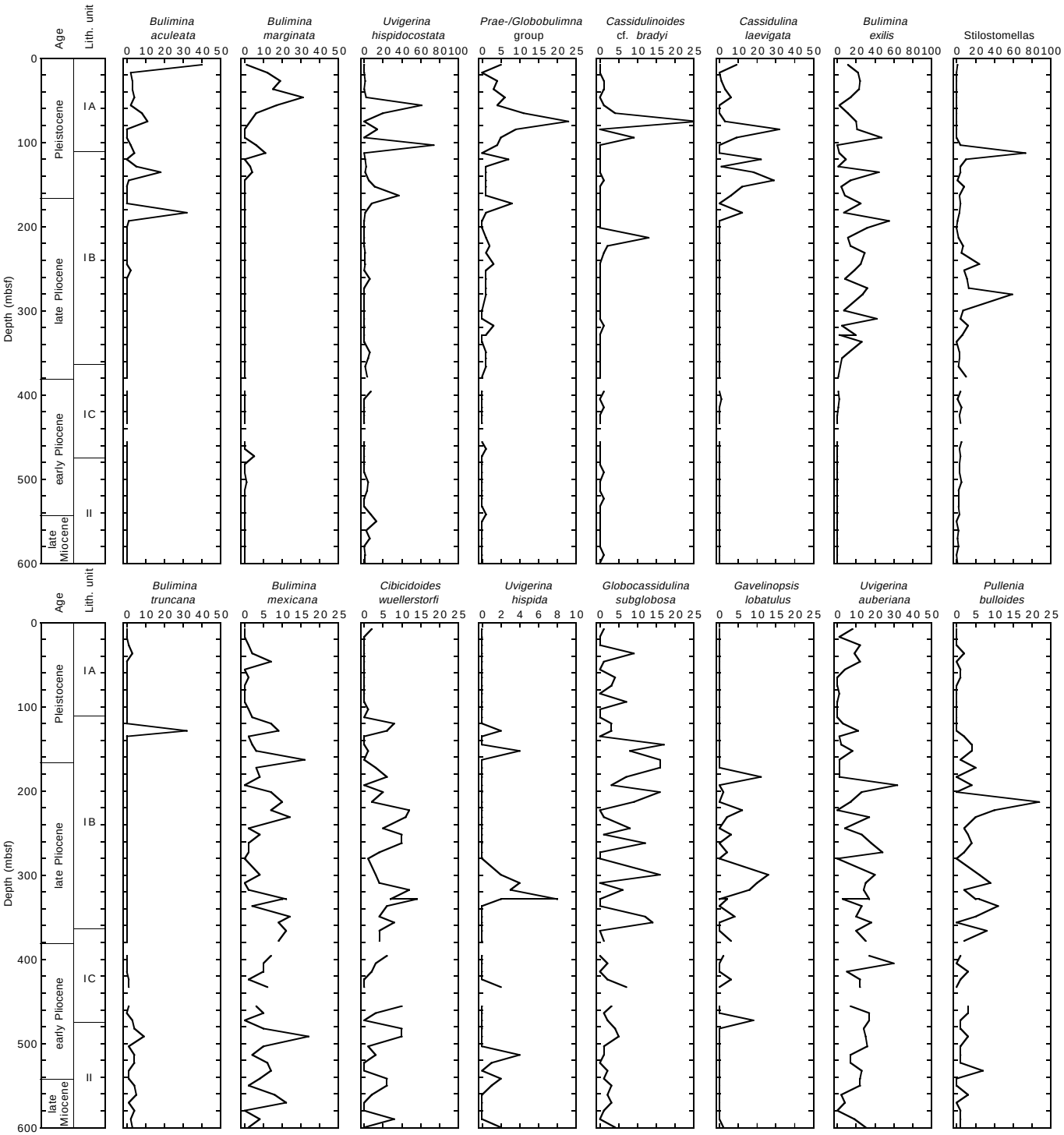

Figure 9. Relative abundances (in percentages) for selected benthic foraminiferal species. See "Lithostratigraphy" section (this chapter) for description of lithostratigraphic units. (Continued next page.)

the FO of *S. pylomaticus*, can be correlated to a zonal sequence from the lower part of the *Cycladophora sakaii* Zone to the *S. pylomaticus* in the North Pacific (Motoyama, 1996).

In the sequence below Sample 54X-CC, the fauna consists mainly of Spumellaria, and age-diagnostic forms are sparse. Therefore, no zones were defined for Samples 175-1082A-55X-CC through 64X-CC. The presence of *Stichocorys peregrina* probably indicates that the deeper sample (62X-CC) is no older than ~9 Ma in age because its FO approximates that age in the high-latitude Southern Ocean (Lazarus, 1992); however, the FO of this species is at ~7 Ma in the tropical region.

Stichocorys peregrina seems to prefer tropical to temperate oceanographic condition (see "Biostratigraphy and Sedimentation Rates" section, "Site 1081" chapter, this volume). In Hole 1082A, *S. peregrina* disappears in Sample 175-1082A-39X-CC, far below the FO of *C. davisiana* (2.7 Ma). The presence of *S. peregrina* through

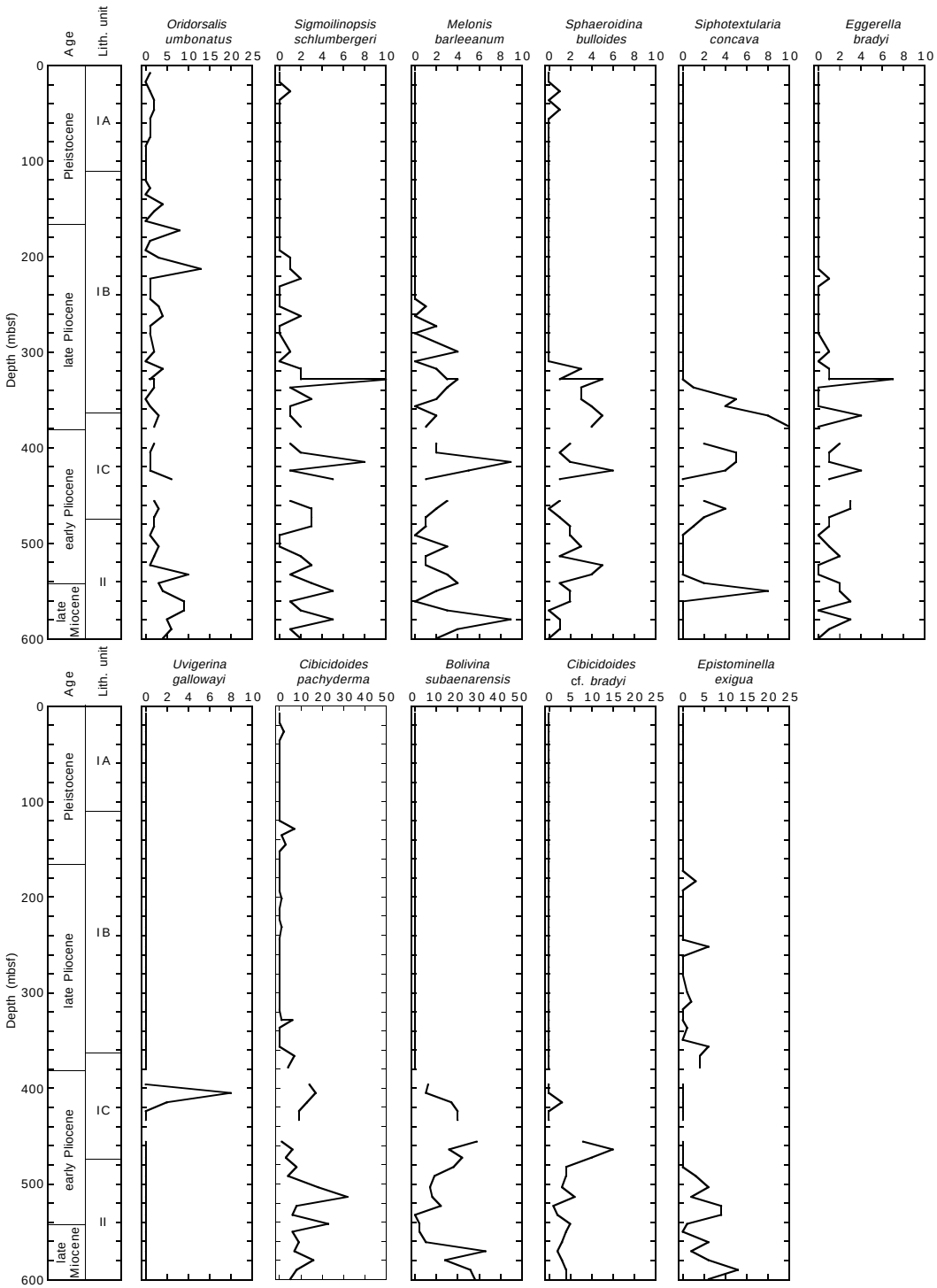

Figure 9 (continued).

the lower sequence indicates temperate oceanographic conditions, and its terminal event indicates a cessation of temperate conditions from the Walvis Basin region. Simultaneously, the Antarctic species *C. pliocenica* first appears in Sample 39X-CC; it ranges up to Sample 21X-CC, indicating invasion of cooler waters into the study region from higher southern latitudes, which agrees with diatom observations (see below).

Diatoms

Diatom counts and identification were carried out using smear slides and acid-treated, sieved (63 µm) material from core-catcher samples from Hole 1082A. Additional samples from within the cores were examined close to datum events to improve the stratigraphic resolution and refine floral changes (Table 6). Diatom preservation is

Table 5. Stratigraphic distribution of radiolarians at Hole 1082A.

Age	Zone	Core, section, interval	Depth (mbsf)	Abundance	Preservation	*Amphirhopalum ypsilon*	*Cycladophora cornutoides*	*Cycladophora davisiana*	*Eucyrtidium calvertense*	*Eucyrtidium teuscheri*	*Eucyrtidium acuminatum*	*Lamprocyclas hannai*	*Lamprocyrtis heteroporos*	*Lamprocyrtis neoheteroporos*	*Pterocanium praetextum eucolpum*	*Pterocanium trilobum*	*Spongurus pylomaticus*	*Axoprunum angelinum*	*Didymocyrtis tetrathalamus tetrathalamus*	*Phormostichoartus corbula*	*Cycladophora pliocenica*	*Theocorythium trachelium*	*Cycladophora sakaii*	*Phormostichoartus fistula*	*Didymocyrtis penultima*	*Stichocorys peregrina*	*Dictyophimus* sp. B	*Saturnalis circularis*	*Stichocorys delmontensis*
		175-1082A-																											
Pleistocene	*A. angulare*	18X-CC	163.06	A	G	+	+	P	P	P	+	P	+	P	P	P	P												
Pleistocene	*A. angulare*	19X-CC	172.74	A	G	P		P	P	P	+	P	P	P		P	P	+	P										
Pleistocene	*A. angulare*	20X-CC	183.51	C	G		P	P	P	P		P	P		+	P				+									
Pliocene	*P. prismatium*	21X-CC	193.47	A	G			P	P	P			P	P		P		+		+	P								
Pliocene	*P. prismatium*	22X-CC	201.31	A	G	+		P	P	P		P	P			P	P	P	P		+	P							
Pliocene	*P. prismatium*	23X-CC	213.19	A	G	+	P	P	P	P	+	P	P	P	+	P	P	P	P	P									
Pliocene	*P. prismatium*	24X-CC	223.03	A	G		P	P	P	P	+	P				P	P	P	+	P									
Pliocene	*P. prismatium*	25X-CC	231.46	A	G	+	P	P	+	P		P				P	P	P		+			+						
Pliocene	*P. prismatium*	26X-CC	244.38	A	G		P			+		P	P	P		P		P											
Pliocene	*P. prismatium*	27X-CC	252.12	A	G	P	P	P	+	P	+	P				P	+	P		+			P						
Pliocene	*P. prismatium*	28X-CC	262.14	A	G			P		P		P	P			P	+	+					P						
Pliocene	*P. prismatium*	29X-CC	273.16	C	G			P		P		P		P		P	P						P						
Pliocene	*C. sakaii-S. pylomaticus*	30X-CC	280.53	A	G	P	P		P	P		P	P			P	P	P					P						
Pliocene	*C. sakaii-S. pylomaticus*	31X-CC	289.10	A	G	P			P	P		P	P			P	P	P		P	P		P						
Pliocene	*C. sakaii-S. pylomaticus*	32X-CC	299.62	A	M	P	P			P		P	P	P	+	P	P	P		P	P		P						
Pliocene	*C. sakaii-S. pylomaticus*	33X-CC	309.63	R	M		P			P		P	+							+	P		+						
Pliocene	*C. sakaii-S. pylomaticus*	34X-CC	317.67	A	M	P	P			P	+		P		P	P	P				P		P	P					
Pliocene	*C. sakaii-S. pylomaticus*	36X-CC	328.55	A	G	+			P	P		P	P			+		+	+	+	P		+						
Pliocene	*C. sakaii-S. pylomaticus*	35X-CC	328.60	A	G		P		P	P	+		P			P			+	P	P								
Pliocene	*C. sakaii-S. pylomaticus*	37X-CC	337.01	A	G					P		P	P				P	P			P				+				
Pliocene	*C. sakaii-S. pylomaticus*	38X-CC	349.23	A	G		P			P	P	P			+	P	P	+	+	P	P								
Pliocene	*C. sakaii-S. pylomaticus*	39X-CC	356.49	A	M		P		P	P		P	P			P	P	P		P	P					+			
Pliocene	*C. sakaii-S. pylomaticus*	40X-CC	366.46	A	G		P		P	P		P	P	P			P	P	+	P						P			
Pliocene	*C. sakaii-S. pylomaticus*	41X-CC	378.29	A	M				P	P		P	P			P	P	P	+	P						P			
Pliocene	*C. sakaii-S. pylomaticus*	42X-CC	386.97	A	M				P	P		P	P	+	P	P	P									P	+		
Pliocene	*C. sakaii-S. pylomaticus*	43X-CC	396.06	A	M				P	P		P	P				P	P											
Pliocene	*C. sakaii-S. pylomaticus*	44X-CC	405.07	A	G				P	P		P	P			P	P	P		P						P	+		
Pliocene	*C. sakaii-S. pylomaticus*	45X-CC	414.98	A	M				P	P		P	P				P									P	+		
Pliocene	*C. sakaii-S. pylomaticus*	46X-CC	424.11	A	M				P			P				P	P	P		P							P		
Pliocene	*C. sakaii-S. pylomaticus*	47X-CC	432.96	A	M				P			P	P	P		P	P									P			
Pliocene	*C. sakaii-S. pylomaticus*	48X-CC	442.70	A	M		+		P	P		P	P	+		P	P	P		+						P			
Pliocene	*C. sakaii-S. pylomaticus*	49X-CC	455.85	A	M				P	P		P	P	+			P									P			
Pliocene	*C. sakaii-S. pylomaticus*	51X-CC	472.75	A	M				P	P		P	P	P			P	P								P			
Pliocene	*C. sakaii-S. pylomaticus*	52X-CC	482.40	A	G				P			P	P				P	P	+						+	P		+	+
Pliocene	*C. sakaii-S. pylomaticus*	53X-CC	491.85	A	M					P		P	P				P	P								P			
Pliocene	*C. sakaii-S. pylomaticus*	54X-CC	503.56	A	M				P			P	P				P	P								P		+	+
Miocene	Unzoned	55X-CC	513.60	A	M				P	P		P						P							+	P		P	
Miocene	Unzoned	56X-CC	523.15	A	M				P			P	+			P		P							P	P		P	P
Miocene	Unzoned	57X-CC	532.68	A	M				P			P						P								P		P	
Miocene	Unzoned	58X-CC	541.98	F	P																								
Miocene	Unzoned	59X-CC	550.05	B																									
Miocene	Unzoned	60X-CC	561.13	A	M				P			P	P					P										P	
Miocene	Unzoned	61X-CC	570.48	A	M				P			P	P					P								P		+	
Miocene	Unzoned	62X-CC	579.77	C	P				P									P						+		+			
Miocene	Unzoned	63X-CC	590.05	A	M				P							+		P										+	
Miocene	Unzoned	64X-CC	599.98	A	P				P			P						P										P	

Notes: Occurrence is indicated by P = present and + = one specimen per slide. Abundance: A = abundant; C = common; R = rare; and B = barren. Preservation: G = good; M = moderate; and P = poor. Zone: *A. angulare* = *Anthocyrtidium angulare; C. sakaii* = *Cycladophora sakaii; P. prismatium* = *Pterocanium prismatium; S. pylomaticus* = *Spongurus pylomaticus.*

moderate throughout Hole 1082A. As was the case at Site 1081, the record of diatom abundance points to a substantial increase in deposition during the late Pliocene and early Pleistocene (from ~366 to 110 mbsf), reaching a maximum in the late Pliocene, followed by a decrease within the Pleistocene about 1 Ma (~100 mbsf). Overall abundances are low (trace to few) or diatoms are absent in upper Miocene and lower Pliocene sediments (Table 6). We may assume that the diatom content at Hole 1082A reflects a varying nutrient supply that could be related to upwelling of nutrient-rich deeper waters and high biological productivity, especially in the late Pliocene (Fig. 10).

The diatom biostratigraphic zones used for this hole are those of Barron (1985). Zones could not be applied to Samples 175-1082A-40X-CC through the end of the hole because of the scarcity of diatom valves and concomitant lack of biostratigraphic markers (Table 6). As was the case at Site 1081, we recorded two middle- to high-latitude cold-water indicator species, *Proboscia* (= *Simonseniella) curvirostris* in Sample 175-1082A-8H-CC (at approximately the Brunhes/Matuyama boundary) and *P. barboi* in Samples 175-1082A-20X-CC through 30X-CC (~1.8–2.8 Ma; see Fig. 10). The presence of these species may indicate periods of intensified Benguela Current transport, an assumption that is also supported by the presence of the Antarctic radiolarian *C. pliocenica* (see above).

The diatom assemblage is similar to that at Site 1081 and consists mainly of a mixture of upwelling-indicator (*Chaetoceros* resting

Table 6. Overall diatom abundance estimated from smear slides for Hole 1082A.

Core, section, interval (cm)	Depth (mbsf)	Overall abundance	Dominant assemblage	Diatom stratigraphic zone
175-1082A-				
1H-1, 55	0.55	1.0		
1H-CC	7.84	2.5	Upwelling	
2H-2, 80	8.60	1.0		
2H-CC	17.37	3.0	Upwelling	
3H-1, 60	17.90	2.0		NTD17
3H-CC	27.16	2.0	Upwelling	
4H-1, 117	27.97	1.0		
4H-CC	36.71	1.0		
5H-1-70	37.00	2.0		
5H-3, 70	39.80	0.0		
5H-7, 30	45.00	2.0		
5H-CC	46.52	1.0		
6H-5, 110	46.90	1.0		
6H-CC	55.82	2.0		
7H-3, 70	54.00	3.0		
7H-CC	65.47	5.0	**Upw**. + neritic +oceanic	
8H-4, 90	68.91	4.0		
8H-CC	75.27	2.0		[*P. curvirostris*]
9H-2, 90	76.70	3.0		
9H-6, 90	82.50	4.0		
9H-CC	84.50	2.0		
10H-5, 90	89.44	3.0		
10H-CC	94.34	1.5		
11H-2, 70	95.50	3.0		
11H-CC	103.45	3.0	Upw. + oceanic	
12H-2, 70	103.84	5.0		
12H-7, 133	111.52	3.0		NTD16
12H-CC	112.84	4.5	Upw. + oceanic	
13H-1, 70	113.00	5.0		
13H-CC	120.24	3.5	Upw. + oceanic	
14H-1, 80	122.60	4.0		
14H-CC	128.58	3.0	Upw. + oceanic	
15X-2, 110	130.82	5.0		
15X-CC	135.30	4.0	Upw. + oceanic	
16X-CC	145.34	3.5	Upw. + oceanic	
17X-1, 90	148.80	5.0		
17X-CC	152.80	3.5	**Upw.** + oceanic	
18X-1, 40	158.00	5.0		
18X-3, 132	161.57	4.0		
18X-CC	163.06	4.5	Upwelling	
19X-2, 70	168.21	5.0		
19X-CC	172.74	4.5	Upw. + oceanic	
20X-2, 70	178.19	4.0		
20X-4, 74	180.98	3.0		
20X-CC	183.51	4.0	Upw. + oceanic	[*P. barboi*]
21X-2, 80	187.72	4.0		
21X-5, 80	191.77	3.0		
21X-CC	193.47	4.0	Upw. + oceanic	
22X-1, 90	197.10	5.0		
22X-4, 42	200.74	5.0		
22X-CC	201.31	4.5	**Upw.** + oceanic	
23X-1, 90	206.80	5.0		
23X-6, 90	212.11	5.0		
23X-CC	213.19	4.5	Upw. + oceanic	
24X-2, 60	217.61	5.0		
24X-5, 120	222.49	5.0		
24X-CC	223.03	4.0		
25X-2, 120	227.88	5.0		
25X-4, 120	230.88	5.0		
25X-CC	231.46	4.5	**Upw.** + oceanic	
26X-2, 80	237.10	5.0		
26X-4, 80	240.10	5.0		NTD15
26X-CC	244.38	5.0	Upw. + oceanic	
27X-1, 30	244.70	5.0		
27X-4, 26	249.16	5.0		
27X-CC	252.12	5.0	**Upw.** + oceanic	
28X-5, 100	260.90	5.0		
28X-CC	262.14	4.5	Upw. + oceanic	
29X-1, 90	264.50	4.0		
29X-4, 120	269.30	4.0		
29X-CC	273.16	5.0	Upwelling	
30X-1, 70	274.00	5.0		
30X-5, 55	279.85	5.0		
30X-CC	280.53	5.0	**Upw.** + oceanic	[*P. barboi*]
31X-1, 40	283.30	5.0		
31X-5, 110	288.66	4.0		
31X-CC	289.10	4.0	Upw. + oceanic	
32X-1, 20	292.70	3.0		
32X-5, 70	299.20	5.0		
32X-CC	299.62	4.0	**Upw.** + oceanic	
33X-1, 60	302.70	5.0		
33X-4, 120	307.84	4.0		
33X-CC	309.63	5.0	Upw. + **oceanic**	
34X-2, 100	314.20	5.0		
34X-CC	317.67	5.0	Upw. + **oceanic**	
35X-1, 80	322.20	4.0		
35X-4, 130	327.20	4.0		
35X-CC	328.60	5.0	**Upw.** + oceanic	
36X-1, 45 cm	327.95	4.0		
36X-CC	328.55	4.5	Oceanic	NTD14
37X-2, 50	331.69	4.0		
37X-CC	337.00	2.0	Upw. + oceanic	
38X-2, 80	342.90	4.0		
38X-CC	349.23	4.5	Oceanic	
39X-2, 40	350.70	4.0		
39X-4, 70	354.32	5.0		
39X-CC	356.49	4.0	Upw. + oceanic	
40X-2, 78	361.10	3.0		
40X-CC	366.46	4.0	Upw. + **oceanic**	
41X-1, 56	370.06	2.0		
41X-3, 73	373.23	1.0		
41X-CC	378.29	1.0		No zone assigned
42X-2, 80	381.50	2.0		
42X-5, 40	385.60	0.0		
42X-CC	386.97	0.0		
43X-1, 120	390.00	0.0		
43X-CC	396.06	1.0		
44X-2, 70	400.60	0.0		
44X-CC	405.07	1.0		
45X-2, 30	409.90	0.0		
45X-CC	414.98	1.0		
46X-1, 80	418.50	0.0		
46X-CC	424.11	1.0		
47X-2, 53	429.33	0.0		
47X-CC	432.96	1.0		
48X-1, 140	438.40	0.0		
48X-CC	442.70	0.0		
49X-2, 72	448.96	0.0		
49X-CC	455.85	0.0		
50X-3, 90	459.66	0.0		
50X-CC	464.01	0.0		
51X-3, 110	470.00	0.0		
51X-CC	472.75	1.0		
52X-4, 59	479.78	0.0		
52X-CC	482.40	0.0		
53X-3, 82	488.52	3.0	Upw. + oceanic	
53X-CC	491.85	2.0	Upwelling	
54X-1, 40	494.80	1.0		
54X-CC	503.56	1.0		
55X-5, 110	510.85	2.0		
55X-CC	513.60	1.0	Upw. + oceanic	
56X-4, 13	517.56	1.0		
56X-CC	523.15	0.0		
57X-CC	532.68	1.0		
58X-CC	541.98	0.0		
59X-CC	550.05	0.0		
60X-CC	561.13	0.0		
61X-CC	570.48	0.0		
62X-CC	579.77	0.0		
63X-CC	590.05	0.0		
64X-CC	599.98	0.0		

Notes: Overall abundance is given as 0 = barren; 1 = trace; 2 = rare; 3 = few; 4 = common; and 5 = abundant. The dominant assemblage in each core catcher and the characteristic diatom stratigraphic zone are given. Note the occurrence of *Proboscia* (= *Simonseniella*) *curvirostris* in Sample 175-1082A-8H-CC and of *P. barboi* in Samples 20X-CC through 30X-CC.

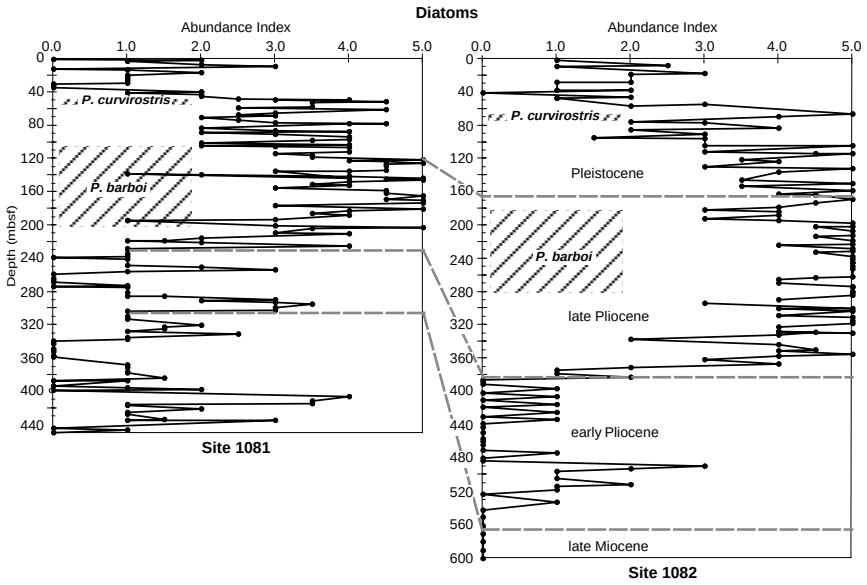

Figure 10. Comparison of the diatom abundance index (0 = barren, 1 = trace, 2 = rare, 3 = few, 4 = common, and 5 = abundant) between Sites 1081 and 1082. Note similar pattern at both sites, with highest values in the late Pliocene. The hatched areas = periods of cold-water influence indicated by the presence of *P. curvirostris* and *P. barboi*.

spores and *Thalassionema nitzschioides* var. *nitzschioides*) and oceanic species (e.g., *Azpeitia nodulifer, A. tabularis, Hemidiscus cuneiformis,* and *Thalassiothrix* spp.). Upwelling-related species are common during highest abundance times in the upper Pliocene sediment within Subunit IB (see "Lithostratigraphy" section, this chapter; Table 6).

PALEOMAGNETISM

The investigation of magnetic properties at Site 1082 included the measurement of bulk susceptibility of whole-core sections and the natural remanent magnetization (NRM) of archive-half sections. Discrete samples were taken from Hole 1082A. Because of time restrictions, only parts of the discrete samples taken from XCB cores were measured on the ship. The Tensor tool was used to orient Cores 175-1082A-3H through 14H, Cores 175-1082B-4H through 14H, and Cores 175-1082C-3H through 24H (Table 7).

Natural Remanent Magnetization and Magnetic Susceptibility

Measurements of NRM were made on all archive-half core sections from Holes 1082A, 1082B, and 1082C. APC sections from Hole 1082A were demagnetized by AF at 10 and 20 mT; XCB sections from Hole 1082A and all sections from Holes 1082B and 1082C were demagnetized by AF at 20 mT only. Magnetic susceptibility measurements were made on whole cores from all holes as part of MST analysis (see "Physical Properties" section, this chapter).

Above 470 mbsf, the intensity of NRM after 20-mT demagnetization fluctuates between 10^{-2} and 10^{-4} A/m, except for the upper 80 mbsf where it ranges between 10^{-2} and 10^{-3}. Below ~470 mbsf, it sharply decreases to between 10^{-4} and 10^{-5} A/m (Fig. 11, second panel). Variations of magnetic susceptibility, generally between 0 and 10 $\times 10^{-5}$ (SI volume units), do not follow those of the remanent intensity (Fig. 11, first panel). Susceptibility is low between 200 and 320 mbsf and high between 350 and 540 mbsf. Diamagnetic materials including water, opal, calcium carbonate, or the plastic core liner (void intervals) could be responsible for the slightly negative susceptibility values.

A magnetic overprint was generally removed by 20-mT demagnetization and a primary NRM was measured for all APC cores (Fig. 11). For XCB cores, however, a significant magnetic overprint re-

Table 7. Tensor tool–orientation data for cores from Holes 1082A, 1082B, and 1082C.

Core	MTF (°)	Inclination angle
175-1082A-		
3H	54	0.74
4H	323	0.85
5H	8	0.64
6H	110	1.07
7H	91	1.25
8H	74	1.15
9H	307	0.98
10H	169	1.06
11H	112	1.41
12H	246	1.01
13H	11	1.25
14H	320	1.05
175-1082B-		
4H	31	0.48
5H	144	0.23
6H	292	0.35
7H	61	0.27
8H	223	0.35
9H	120	0.42
10H	92	0.47
11H	310	0.54
12H	312	0.64
13H	165	0.54
14H	50	0.82
175-1082C-		
3H	69	0.88
4H	27	0.72
5H	248	0.76
6H	16	0.86
7H	162	0.50
8H	202	0.50
9H	72	0.62
10H	350	0.67
11H	321	0.52
12H	93	0.26
13H	358	0.92
14H	241	0.54
15H	220	0.73
16H	217	0.70
17H	200	0.77
18H	221	0.73
19H	202	0.57
20H	273	0.46
21H	330	0.35
22H	138	0.55
23H	47	0.17
24H	199	0.15

Notes: The orientation parameter (MTF) is the angle in degrees between magnetic north and the double line marked on the center of the working half of the core. The local declination anomaly is 15°W.

mained after AF demagnetization. Declinations cluster around –30°, independent of the orientation of the sediments, even where the sediments are extensively biscuited (Fig. 11A). This phenomenon is similar to that observed at Site 1081 (see "Paleomagnetism" section, "Site 1081" chapter, this volume), where the magnetic overprint was attributed to the coring process. Inclinations, however, show two groupings with distinct polarity biases after 20-mT demagnetization, although the directions are strongly scattered. The scattering is most severe below an intensity decrease at about 470 mbsf. One grouping, with a bias range of 40° to 60° in inclination, is interpreted as reversed polarity, and the other grouping, with a bias range of –30° to 0° in inclination, is interpreted as normal polarity. Overall, however, the inclinations are biased downward, probably because of a downward-oriented magnetic overprint. Normal-polarity intervals (the Olduvai Subchron, discussed later) occurring from ~165 to 182 mbsf in XCB cores from Hole 1082A and from 164 to 182 mbsf in APC cores from Hole 1082C lend support to the polarity interpretations based on inclinations from XCB cores (Fig. 11). Preliminary measurements of discrete samples between 370 and 470 mbsf from Hole 1082A yielded results similar to the half-core measurements.

Magnetostratigraphy

We identified the polarity of the NRM from the magnetic declinations and inclinations of APC cores and from the inclinations of XCB cores. The magnetostratigraphic interpretation is summarized in Table 8 and displayed in Figure 12.

There are two possible interpretations (models) for the polarity-chron assignment between ~300 and 460 mbsf (Table 8). The major difference between the two is the position of the top of Chron C2Ar (the Gauss/Gilbert boundary), which is at 390 mbsf in Model 1 and at 340 mbsf in Model 2. According to Model 1, the sedimentation rate was significantly higher in the earlier part of the Gauss Chron, between ~3.0 and 3.5 Ma, whereas it was lower between ~3.5 and 4.2 Ma (Fig. 12). In Model 2, the sedimentation rate is rather constant between ~2.6 and 4.2 Ma, but higher between ~4.2 and 4.8 Ma. Model 1 fits the biostratigraphy better than Model 2 (see "Biostratigraphy and Sedimentation Rates" section, this chapter) and is thus adopted here.

The Cobb Mountain event (1.201–1.211 Ma) was identified by an intensity decrease and a directional shift at all three holes. The Reunion event at Hole 1082C also accompanies an intensity decrease and a change in direction. Hole 1082B did not reach the depth at which this event would be expected. The Reunion event may also be recorded in XCB cores from Hole 1082A; a change in the inclination and a decrease in the intensity at ~200 mbsf is consistent with the depth observed at Hole 1082C.

A complete transitional record of the Brunhes/Matuyama polarity change was identified at Hole 1082C, where the measurement was carried out at 2-cm intervals instead of the routine 5-cm intervals. The transitional interval spans 0.4 m (70.5–70.9 mbsf). In the other two holes, part (at Hole 1082A) or all (at Hole 1082B) of the transition record unfortunately was missing because of a coring gap.

Relative Paleointensity During the Brunhes Chron

The intensity of NRM can be controlled by the strength of the geomagnetic field, the concentration of magnetic minerals that carry the NRM, and other rock-magnetic characteristics of sediments including composition, grain-size, and interaction of magnetic minerals. If the sediments are uniform rock-magnetically and the concentration of magnetic minerals is represented by some rock-magnetic parameters (e.g., magnetic susceptibility, anhysteretic remanent magnetization, and isothermal remanent magnetization), variations of remanent intensity after normalization by the rock-magnetic parameters can be interpreted as relative changes of past geomagnetic-field strength (paleointensity; King et al., 1983). The paleointensity during the last 200 k.y. is relatively well understood (Yamazaki and Ioka, 1994; Guyodo and Valet, 1996), and efforts have been made to establish a paleointensity curve for the Brunhes Chron (Kent and Opdyke, 1977; Valet and Meynadier, 1993; Yamazaki et al., 1995). Figure 13 shows the relative remanent intensity at Hole 1082A during the Brunhes Chron after normalization by the magnetic susceptibility. Variations of the relative intensity are similar to the documented characteristics of the paleointensity during the Brunhes Chron; that is, the quasi-cyclic intensity lows at ~100-k.y. intervals and a peak in the intensity just after the Brunhes/Matuyama polarity transition (Valet and Meynadier, 1993; Yamazaki et al., 1995). Our results suggest that sediments at this site could be useful for the study of detailed paleointensity changes, although the assumptions mentioned above must be thoroughly tested by rock-magnetic analyses before the variations can be interpreted as paleointensity of the geomagnetic field.

COMPOSITE SECTION

Based upon correlations among MST measurements of magnetic susceptibility, GRAPE density, and Minolta spectrophotometer measurements, the completeness of the stratigraphic sequence was documented for the upper 141 mcd at Site 1082. Development of this composite depth section follows the procedure described in the"Explanatory Notes" chapter (this volume). All data used for constructing the composite section were measured at 2-cm intervals in Cores 175-1082A-1H through 8H and at 4-cm intervals for the remainder of Hole 1082A, as well as for Holes 1082B and 1082C.

Magnetic susceptibility, GRAPE density, and color reflectance (chromaticity b*) parameters were all used to develop interhole correlations to verify core gaps, though the composite is primarily based upon magnetic susceptibility. Natural gamma ray (NGR) emissions and *P*-wave velocity were also measured on the MST; however, the coarseness (32-cm measurement interval) for NGR and low signal-to-noise ratio for *P*-wave velocity precluded their use in constructing the composite section. Measurement quality decreased downhole and required extensive filtering of the data because of core disturbance and gas voids. The filtering procedure is described in the "Composite Section" section, "Site 1075" chapter, this volume.

Hole-to-hole splices constraining intercore gaps for this site were excellent over the entire composite section of 141 mcd (Fig. 14). A composite record below 141 mcd was not possible because the bottom of Hole 1082B was reached and recovery was relatively poor for the XCB-cored portion of Hole 1082A. Although not part of the composite section, magnetic susceptibility and chromaticity data are plotted below 150 mcd in Figure 14.

At Hole 1082C, an interval of 5 m was double-cored in Cores 175-1082C-3H and 4H. Based on magnetic susceptibility, we found an excellent correlation of the lower 5 m of Core 3H to the upper 5 m of Core 4H, as well as to adjacent Core 175-1082A-3H, despite the double coring of Hole 1082C. It should be noted that according to the driller's depth (in mbsf) recorded in the core log, Core 175-1082C-4H overlaps Core 5H by 5 m.

Gaps between successive cores of the same hole average between 1 and 2 m at Site 1082. Gaps are not necessarily actual coring gaps. They may result from the stretching of the mcd scale compared with the mbsf scale as a result of core expansion alone. Between Cores 175-1082C-1H and 2H, a large 4.5-m gap exists.

Continuous overlap of the composite section of Holes 1082A–C enables the construction of a single spliced record constructed from magnetic susceptibility and color reflectance (chromaticity b*; Fig. 15). The splice is composed primarily of Holes 1082A and 1082B and can be used as a sampling guide to ensure a continuous stratigraphic sequence. Tie points between cores of adjacent holes used to

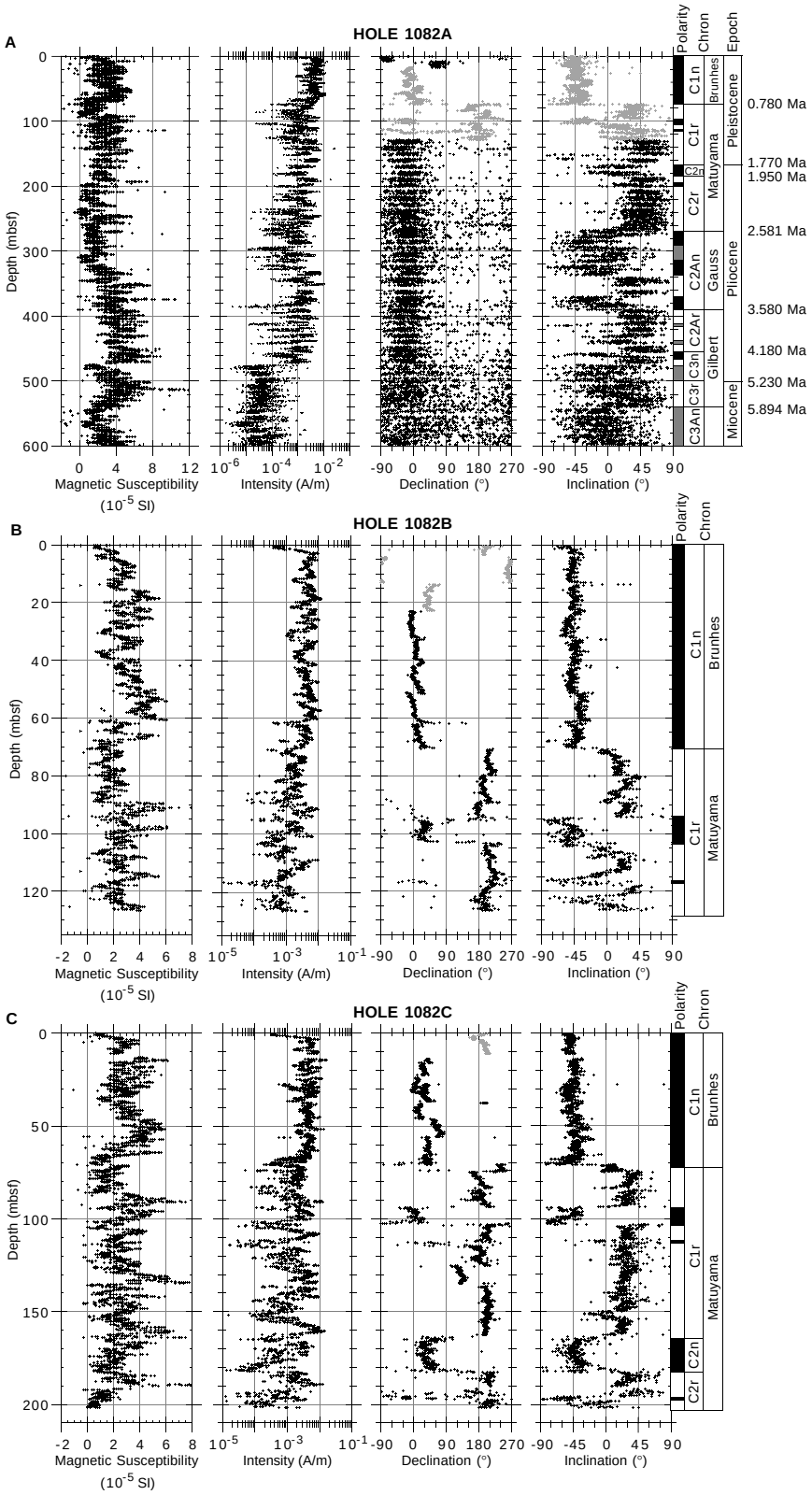

Figure 11. Magnetic susceptibility (SI) and NRM intensity, declination, inclination, and magnetostratigraphic interpretation after 20-mT demagnetization for (**A**) Hole 1082A, (**B**) Hole 1082B, and (**C**) 1082C. Black symbols = Tensor corrected; gray symbols = uncorrected. Polarity shading: black = normal, white = reversed, and gray = ambiguous.

Table 8. Magnetostratigraphic interpretations for Site 1082.

Polarity chron	Age (Ma)	Depth (mbsf) Hole 1082A, Model 1	Hole 1082A, Model 2	Hole 1082B	Hole 1082C	Polarity epoch
C1n	0.00-0.78	0-74		0-71	0-71	Brunhes
C1r.1r	0.78-0.99	74-97		71-95	71-94	Matuyama
C1r.1n	0.99-1.07	97-105		95-105	94-103	Jaramillo
C1r.2r-1n	1.20-1.21	118		118	117	Cobb Mountain
C2n	1.77-1.95	165-182			164-182	Olduvai
C2r.1n	2.14-2.15	196				Reunion
C2An.1n (top)	2.58-3.04	270				Gauss
C2An.1r (top)	3.04-3.11	295-315?	295?			Kaena
C2An.2r (top)	3.22-3.33	340	-			Mammoth
C2An.3n (top)	3.33-3.58	368	315?			
C2Ar (top)	3.58	390	340			Gilbert
C3n.1n (top)	4.18	415	368-390			Cochiti
C3n.2n (top)	4.48	440?	415			Nunivak
C3n.3n (top)	4.80	460				Sidufjall
C3n.4n (top)	4.98	475				Thvera
C3r (top)	5.23	500				
C3An.1n (top)	5.89	540				

Note: Time scale used is that of Berggren et al. (1995).

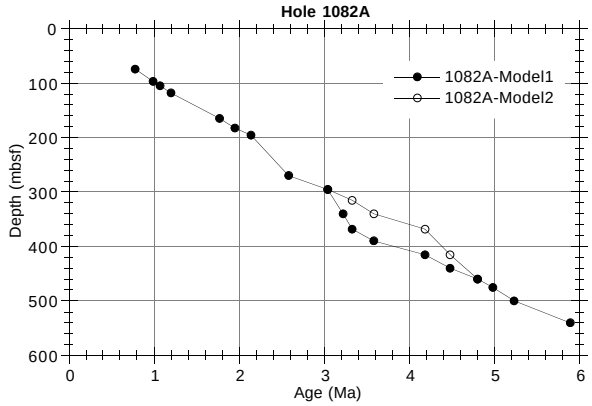

Figure 12. Age-depth plots for Hole 1082A, based on magnetostratigraphic interpretations from Table 8.

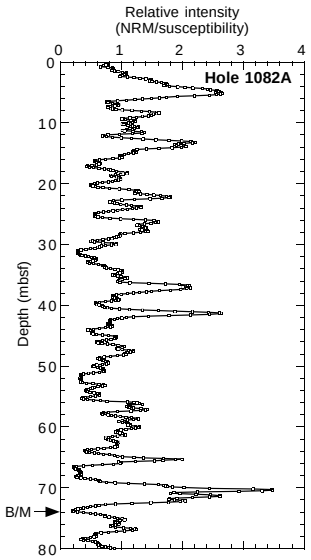

Figure 13. Relative remanent intensity at Hole 1082A during the Brunhes Chron after normalization by magnetic susceptibility. B/M = Brunhes/Matuyama boundary.

construct the splice are given in Table 9. Below 141 mcd, the relative core depths were not adjusted but were simply appended to the composite depth scale.

Because depth adjustments to the whole core are based upon correlation of sedimentary features over a ±2-m window, intracore features outside this window may be offset as a result of core distortions. Thus, some features in the composite record (Fig. 14) may not be aligned between adjacent holes of the composite section. Offsets of the mcd scale relative to the mbsf scale are given in Table 10. These measurements indicate that the composite section is expanded by ~10% relative to the mbsf scale (Fig. 16).

INORGANIC GEOCHEMISTRY

Fifty-seven interstitial water samples were gathered from Hole 1082A over a depth range from 1.4 to 586 mbsf. Whole-round samples were sampled at a frequency of one sample per section for the upper 55 mbsf, one sample per core from 55 to 107 mbsf, and every third core thereafter to total depth (Table 11). As with Site 1081, also a deeply drilled site in the same general region as Site 1082, we are able to relate the interstitial water chemistry to a variety of diagenetic processes that reflect not only remineralization of organic matter in the shallower sediments, but also compositional changes in the deeper sediments. As an overall comparison between the two sites, the interstitial water chemistry at Site 1082 records the greater supply of organic matter, along with a pronounced contrast in many dissolved species distributions between lithostratigraphic Units I and II.

Alkalinity, Sulfate, and Ammonium

Downcore profiles of alkalinity, sulfate, and ammonium (Fig. 17) through the upper ~100 mbsf record the degradation of organic matter. Sulfate is completely consumed within the upper 25 mbsf, which is approximately twice as quickly as at Site 1081. Through this uppermost depth interval, alkalinity values increase sharply, and the concentration of ammonium also shows the greatest relative increase. Alkalinity and ammonium eventually reach maxima that are two to three times those observed at Site 1081.

After reaching a broad maximum from ~90 to 250 mbsf, alkalinity decreases steadily to a minimum value of 16.8 mM at the bottom of the hole. Through this deeper interval, ammonium concentrations also reach maximum values before decreasing toward the boundary between lithostratigraphic Subunit IC and Unit II. This decrease most likely indicates cation exchange reactions during clay diagenesis.

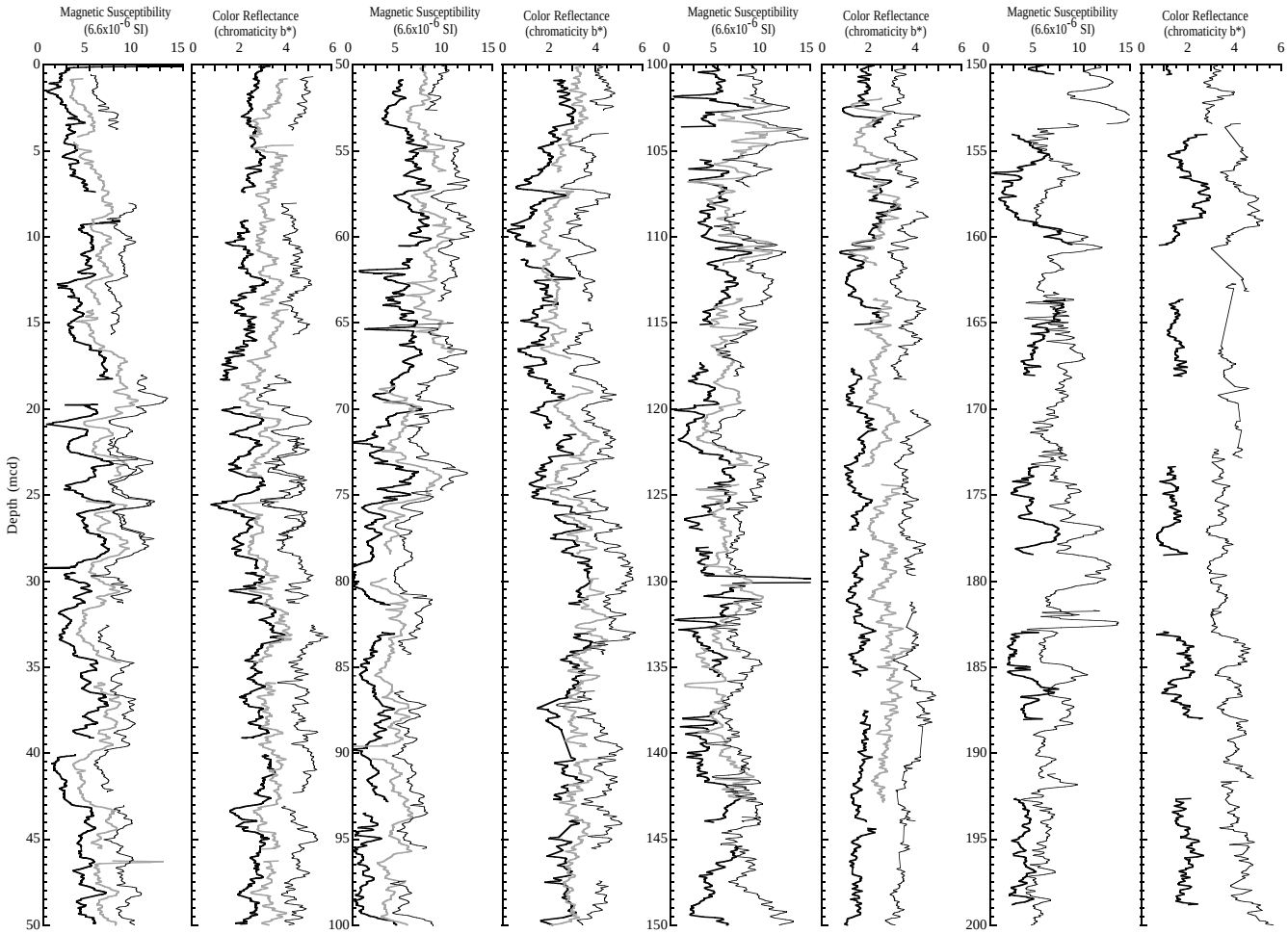

Figure 14. Composite section for Site 1082. Magnetic susceptibility and the color reflectance (chromaticity b*) data are plotted for Holes 1082A (thick black line), 1082B (gray line), and 1082C (thin black line). The downhole logs are shown in meters composite depth (mcd). Offsets have been applied to data for Holes 1082B and 1082C for clarity in viewing the composite sections.

Moreover, within lithostratigraphic Unit II, ammonium concentrations increase dramatically to values greater than the maximum observed stratigraphically higher in lithostratigraphic Subunit IB. Because TOC concentrations in Unit II are lower than those in Subunits IA and IB (see "Organic Geochemistry" section, this chapter), this increase in dissolved ammonium is surprising. It may be related to the smaller amount of clay in the nannofossil ooze of Unit II, compared with the nannofossil clay of Subunit IC (see "Lithostratigraphy" section, this chapter). Presumably, the smaller proportional amount of clay decreases the amount of ammonium that can be removed by ion exchange reactions.

Calcium, Magnesium, and Strontium

Concentration profiles of Ca^{2+}, Mg^{2+}, and Sr^{2+} reflect processes of carbonate dissolution and precipitation (Fig. 18). Dissolved Sr^{2+} increases monotonically to the middle of lithostratigraphic Subunit IB at ~280 mbsf, before increasing the rate of increase to the bottom of the sequence. The deeper gradual increase records continual dissolution of biogenic calcite. Within the uppermost nearly 50 mbsf, dissolved Ca^{2+} and Mg^{2+} concentrations decrease by essentially the same amount (~8 mM), suggesting that dolomite is precipitating and removing dissolved Ca^{2+} and Mg^{2+} in equal proportions. The dissolved Ca^{2+} profile at Site 1082 is very similar to that previously observed at Site 1081, whereas the decrease in dissolved Mg^{2+} at Site 1082 is more gradual than that at Site 1081. Because dissolved Ca^{2+} is increasing through the sequence from 50 mbsf to the bottom of the sequence at both sites, the contrast in dissolved Mg^{2+} between the two sites likely reflects differences in Mg^{2+} uptake by clay minerals.

Silica and Phosphate

Dissolved silica increases in concentration rapidly from representative bottom-water values to a maximum of ~1200 µM at 50 mbsf (Fig. 19), recording the dissolution of biogenic opal. A slight minimum (~1000 µM) occurs at 100 mbsf, corresponding to a low in the first-order abundance index of diatom distributions (see "Biostratigraphy and Sedimentation Rates" section, this chapter). From 100 to nearly 520 mbsf, dissolved silica concentrations increase gradually. Interestingly, dissolved silica does not show a maximum within lithostratigraphic Subunit IB (nannofossil and diatom-rich clay; see "Lithostratigraphy" section, this chapter), despite the greater potential source of biogenic silica in this subunit. Dissolved silica decreases in concentration through lithostratigraphic Unit II, the nannofossil ooze, likely reflecting the decrease in diatom abundance through this

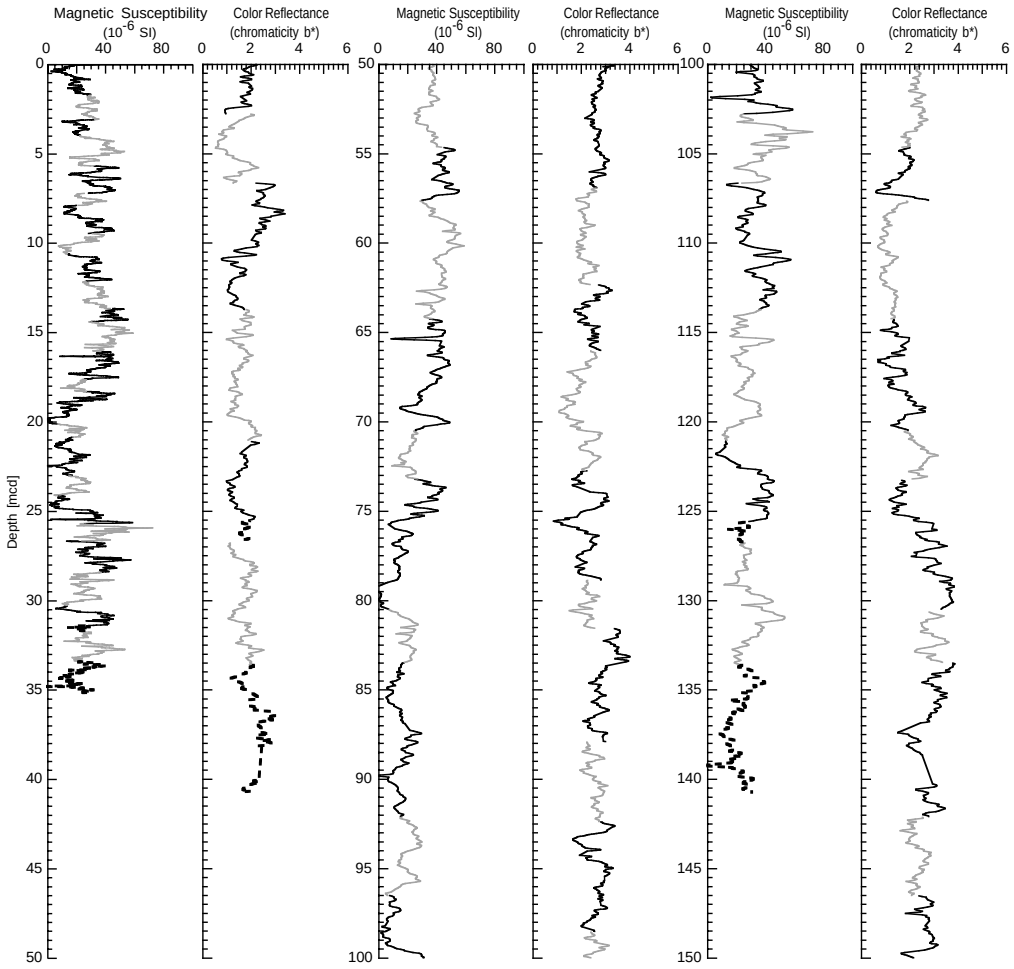

Figure 15. Spliced records for magnetic susceptibility and color reflectance (chromaticity b*) plotted in meters composite depth (mcd). Cores from three holes at Site 1082 have been used for the spliced record: solid black line = Hole 1082A, gray line = Hole 1082B, and dashed line = Hole 1082C.

Table 9. List of splice tie points used to create the continuous "spliced" stratigraphic sequence for Site 1082.

Hole, core, section, interval (cm)	Depth (mbsf)	Composite depth (mcd)	Whether tied	Hole, core, section, interval (cm)	Depth (mbsf)	Composite depth (mcd)	Offset (m)
1082A-1H-5, 90	6.90	6.90	Tie to	1082B-2H-2, 93	6.14	6.90	0.76
1082B-2H-6, 36	11.56	12.32	Tie to	1082A-2H-3, 32.5	11.13	12.32	1.19
1082A-2H-5, 120	14.80	15.99	Tie to	1082B-3H-2, 31.5	15.03	15.99	0.96
1082B-3H-6, 108	21.78	22.74	Tie to	1082A-3H-3, 26.5	20.37	22.74	2.37
1082A-3H-7, 78	26.48	28.85	Tie to	1082B-4H-3, 61	26.32	28.85	2.53
1082B-4H-5, 32	29.02	31.55	Tie to	1082A-4H-2, 70.5	28.91	31.55	2.64
1082A-4H-7, 4	35.24	37.88	Tie to	1082B-5H-2, 55.5	34.27	37.88	3.61
1082B-5H-5, 56	38.76	42.37	Tie to	1082A-5H-2, 92.5	38.63	42.37	3.74
1082A-5H-7, 8	44.78	48.52	Tie to	1082B-6H-2, 84	44.04	48.52	4.48
1082B-6H-6, 96	50.16	54.64	Tie to	1082A-6H-3, 102.5	49.63	54.64	5.01
1082A-6H-5, 120	52.60	57.61	Tie to	1082B-7H-1, 35.5	51.57	57.61	6.04
1082B-7H-5, 100	58.20	64.24	Tie to	1082A-7H-3, 2.5	58.33	64.24	5.91
1082A-7H-7, 30	64.60	70.51	Tie to	1082B-8H-2, 42.5	62.63	70.51	7.88
1082B-8H-4, 12	65.32	73.20	Tie to	1082A-8H-3, 24.5	66.76	73.20	6.44
1082A-8H-8, 4	74.05	80.49	Tie to	1082B-9H-1, 52	70.72	80.49	9.77
1082B-9H-3, 48	73.68	83.45	Tie to	1082A-9H-1, 52	74.82	83.45	8.63
1082A-9H-7, 36	83.46	92.09	Tie to	1082B-10H-2, 31.5	81.53	92.09	10.56
1082B-10H-5, 24	85.94	96.50	Tie to	1082A-10H-3, 114.5	86.89	96.50	9.61
1082A-10H-8, 12	93.16	102.77	Tie to	1082B-11H-1, 90.5	90.11	102.77	12.66
1082B-11H-4, 28	93.98	106.64	Tie to	1082A-11H-1, 118.5	94.49	106.64	12.15
1082A-11H-6, 92	101.57	113.72	Tie to	1082B-12H-1, 22.5	98.93	113.72	14.79
1082B-12H-6, 4	106.24	121.03	Tie to	1082A-12H-4, 72	106.56	121.03	14.47
1082A-12H-7, 92	111.11	125.58	Tie to	1082C-13H-4, 92	108.42	125.58	17.16
1082C-13H-5, 60	109.60	126.76	Tie to	1082B-13H-2, 94.5	110.65	126.76	16.11
1082B-13H-7, 28	117.48	133.59	Tie to	1082C-14H-2, 120	115.20	133.59	18.39
1082C-14H-7, 84	122.34	140.73					

Note: The tie points are listed in standard ODP meters below seafloor (mbsf) and meters composite depth (mcd).

Table 10. Offsets applied to cores from Holes 1082A, 1082B, and 1082C.

Core	Depth (mbsf)	Offset (m)	Composite depth (mcd)
175-1082A-			
1H	0.0	0.00	0.00
2H	7.8	1.19	8.99
3H	17.3	2.37	19.67
4H	26.8	2.64	29.44
5H	36.3	3.74	40.04
6H	45.8	5.01	50.81
7H	55.3	5.91	61.21
8H	64.8	6.44	71.24
9H	74.3	8.63	82.93
10H	83.8	9.61	93.41
11H	93.3	12.15	105.45
12H	102.8	14.47	117.27
13H	112.3	15.66	127.96
14H	121.8	15.66	137.46
15X	128.6	15.66	144.26
16X	138.3	15.66	153.96
17X	147.9	15.66	163.56
18X	157.6	15.66	173.26
19X	167.2	15.66	182.86
20X	176.9	15.66	192.56
21X	186.5	15.66	202.16
22X	196.2	15.66	211.86
23X	205.9	15.66	221.56
24X	215.5	15.66	231.16
25X	225.2	15.66	240.86
26X	234.8	15.66	250.46
27X	244.4	15.66	260.06
28X	254.0	15.66	269.66
29X	263.6	15.66	279.26
30X	273.3	15.66	288.96
31X	282.9	15.66	298.56
32X	292.5	15.66	308.16
33X	302.1	15.66	317.76
34X	311.7	15.66	327.36
35X	321.4	15.66	337.06
36X	327.5	15.66	343.16
37X	331.0	15.66	346.66
38X	340.6	15.66	356.26
39X	350.3	15.66	365.96
40X	359.9	15.66	375.56
41X	369.5	15.66	385.16
42X	379.2	15.66	394.86
43X	388.8	15.66	404.46
44X	398.4	15.66	414.06
45X	408.1	15.66	423.76
46X	417.7	15.66	433.36
47X	427.3	15.66	442.96
48X	437.0	15.66	452.66
49X	446.7	15.66	462.36
50X	456.3	15.66	471.96
51X	465.9	15.66	481.56
52X	475.1	15.66	490.76
53X	484.7	15.66	500.36
54X	494.4	15.66	510.06
55X	504.1	15.66	519.76
56X	513.8	15.66	529.46
57X	523.4	15.66	539.06
58X	533.1	15.66	548.76
59X	542.8	15.66	558.46
60X	552.4	15.66	568.06
61X	562.0	15.66	577.66
62X	571.7	15.66	587.36
63X	581.3	15.66	596.96
64X	590.9	15.66	606.56
175-1082B-			
1H	0.0	0.73	0.73
2H	3.7	0.76	4.46
3H	13.2	0.96	14.16
4H	22.7	2.53	25.23
5H	32.2	3.61	35.81
6H	41.7	4.48	46.18
7H	51.2	6.04	57.24
8H	60.7	7.88	68.58
9H	70.2	9.58	79.78
10H	79.7	10.56	90.26
11H	89.2	12.66	101.86
12H	98.7	14.79	113.49
13H	108.2	16.11	124.31
14H	117.7	16.11	133.81
175-1082C-			
1H	0.0	0.49	0.49
2H	3.5	4.46	7.96
3H	13.0	4.94	17.94
4H	22.5	–0.89	21.61
5H	27.0	5.47	32.47
6H	36.5	6.50	43.00
7H	46.0	7.90	53.90
8H	55.5	9.40	64.90
9H	65.0	9.66	74.66
10H	74.5	11.82	86.32
11H	84.0	13.34	97.34
12H	93.5	14.91	108.41
13H	103.0	16.97	119.97
14H	112.5	18.63	131.13
15H	122.0	18.63	140.63
16H	125.0	18.63	143.63
17H	134.5	18.63	153.13
18H	144.0	18.63	162.63
19H	153.5	18.63	172.13
20H	163.0	18.63	181.63
21H	172.5	18.63	191.13
22H	182.0	18.63	200.63
23H	191.5	18.63	210.13
24H	195.6	18.63	214.23

Note: The offsets transform ODP standard depth values in meters below seafloor (mbsf) to meters composite depth (mcd).

portion of the sequence (see "Biostratigraphy and Sedimentation Rates" section, this chapter).

Dissolved phosphate concentrations increase with depth within Subunit IA, recording the remineralization of organic matter. The slight inflection change in the increase found between ~20 and 40 mbsf corresponds with a similar pattern in the alkalinity profile and may reflect a change in organic matter concentration or composition. After reaching a sharply defined maximum of 161 µM at 69 mbsf, dissolved phosphate decreases relatively smoothly to ~400 mbsf, below which concentrations are <10 µM. Within the upper reaches of lithostratigraphic Subunit IB, there appears to be a zone of increased dissolved phosphate removal (shaded region in Fig. 19).

Sodium and Potassium

The concentration of dissolved Na^+ increases from seawater values to maximum values at depth (Fig. 20). This increase may be recording the release of Na^+ from clay minerals. The concentration of K^+ (Fig. 20) shows some variability in the uppermost 50 mbsf before remaining essentially constant to ~300 mbsf, below which the concentration of dissolved K^+ decreases dramatically. This decrease only broadly corresponds with the lithologic boundary between lithostratigraphic Subunits IB and IC. This broad pattern in dissolved K^+ is similar to that observed at Site 1081, although at Site 1081 there was no relationship among the lithostratigraphic unit distributions. Because this decrease in dissolved K^+ occurs over a depth range similar to the one in which ammonium concentrations decrease, we interpret these concentration profiles as reflecting deep ion exchange reactions with clay.

Salinity and Chloride

Salinity is greater at Site 1082 than at Site 1081, reflecting the greater amounts of alkalinity, ammonium, Mg^{2+}, silica, phosphate, Na^+, and K^+, particularly through the uppermost 300 mbsf (Fig. 21). Concentrations of dissolved Cl^- record several maxima and minima through the uppermost 50 mbsf, perhaps recording variations in bottom-water content during glacial (and interglacial?) periods. From 130 mbsf to the bottom of the hole, dissolved Cl^- concentrations steadily increase.

ORGANIC GEOCHEMISTRY

Calcium carbonate and organic carbon concentrations were measured on sediment samples from Hole 1082A (Table 12). Organic

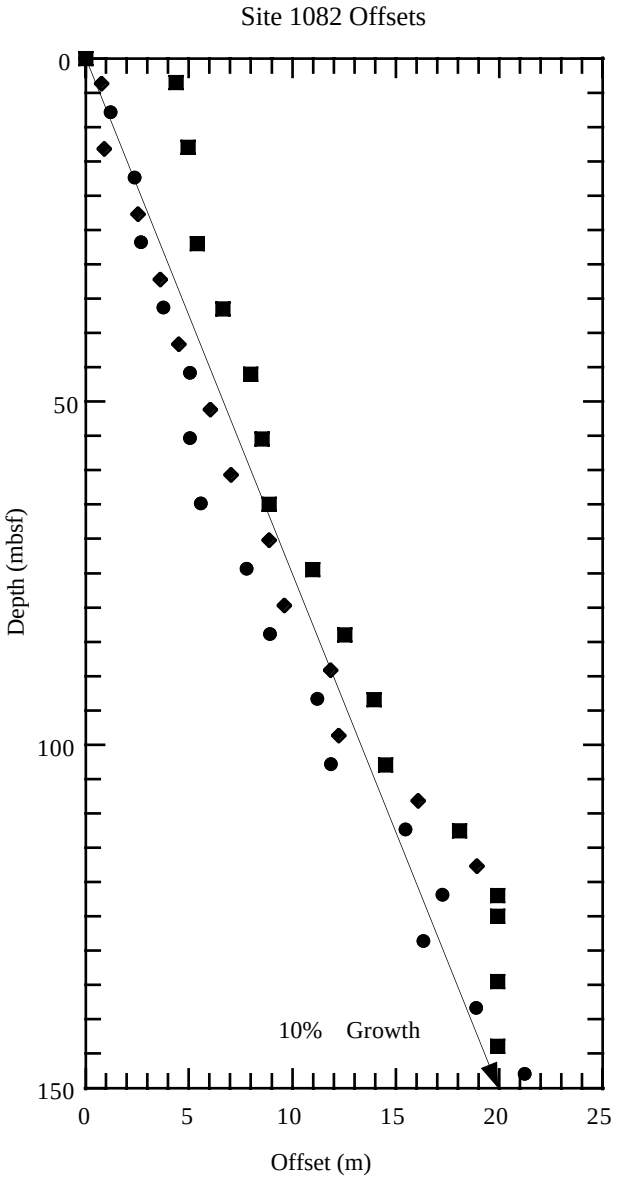

Figure 16. Core offsets applied to Site 1082 plotted against standard ODP meters below seafloor (mbsf). A linear 10% growth of meters composite depth (mcd) compared with mbsf is indicated by an arrow for orientation. Offsets are plotted for Holes 1082A (circles), 1082B (diamonds), and 1082C (squares).

matter atomic carbon/nitrogen (C/N) ratios and Rock-Eval pyrolysis analyses were employed to determine the type of organic matter contained within the sediments. Elevated amounts of gas were encountered, and routine monitoring of the sedimentary gases was done for drilling safety.

Inorganic and Organic Carbon Concentrations

Concentrations of carbonate carbon in Site 1082 sediments range between 10.3 and 0.1 wt%, corresponding to 85.8 and 1.0 wt% $CaCO_3$ (Table 12). The carbonate concentrations vary in two ways: (1) closely spaced changes related to light–dark color fluctuations and (2) a general downhole decrease followed by an increase in concentrations (Fig. 22). Sediments at this site are divided into an upper lithostratigraphic unit, which has three subunits, and a lower unit (see "Lithostratigraphy" section, this chapter). Subunit IA, a Pleistocene nannofossil- and foraminifer-rich clay, averages 42 wt% $CaCO_3$. Subunit IB is a Pliocene–Pleistocene diatom-rich clay that averages 33 wt% $CaCO_3$. Subunit IC is a Pliocene nannofossil clay that contains an average of 52 wt% $CaCO_3$. Unit II, a Miocene–Pliocene nannofossil ooze, averages 67 wt% $CaCO_3$. The variations in concentrations reflect varying combinations of changes in delivery of calcareous material, dilution by noncalcareous components, and carbonate dissolution fueled by oxidation of organic matter.

TOC determinations were done on selected samples of Hole 1082A sediments to estimate the amounts of organic matter in the different lithostratigraphic units (Table 12). Like $CaCO_3$ concentrations, TOC concentrations change in both short-term and longer term patterns (Fig. 23). Dark-colored sediments have higher TOC values than light-colored layers. TOC concentrations also differ in Hole 1082A lithostratigraphic units, averaging 6.16 wt% in Subunit IA, 4.07 wt% in Subunit IB, 2.31 wt% in Subunit IC, and 0.71 wt% in Unit II. The high TOC concentrations in the subunits of Unit I are a consequence of the elevated paleoproductivity of the Benguela Current upwelling system, which has delivered abundant organic matter to the sediments, and the high accumulation rate of sediments (see "Biostratigraphy and Sedimentation Rates" section, this chapter), which enhances preservation of the organic matter.

Organic Matter Source Characterization

Organic C/N ratios were calculated for sediment samples from the different Site 1082 lithostratigraphic units using TOC and total nitrogen concentrations (Table 12). The C/N ratios vary from 18.2 to <1 (Fig. 24). Most of these C/N ratios are intermediate between unaltered algal organic matter (5–8) and fresh land-plant material (25–35; e.g., Emerson and Hedges, 1988; Meyers, 1994). The low C/N ratios occur in samples that are poor in organic carbon; these values may be biased by the tendency of clay minerals to absorb ammonium ions generated during the degradation of organic matter (Müller, 1977). The means of the C/N ratios in each lithostratigraphic unit are as follows: Subunit IA, 14.9; Subunit IB, 14.1; Subunit IC, 11.8; and Unit II, 6.8. Because of their setting under a major upwelling system and offshore from a coastal desert, it is likely that these organic carbon–rich sediments contain mostly marine-derived organic matter with only a minor contribution of detrital continental organic matter. The C/N ratios that are higher than fresh algal organic matter indicate that preferential loss of nitrogen-rich, proteinaceous matter and consequent elevation of C/N ratios occurred during settling of organic matter to the seafloor. Such early diagenetic alteration of C/N ratios is often seen under areas of elevated marine productivity such as upwelling systems (Meyers, 1997).

A Van Krevelen–type plot of the hydrogen index (HI) and oxygen index (OI) values indicates that the sediments contain type II (algal) organic matter (Fig. 25) that has been altered by microbial processing during early diagenesis. Well-preserved type II organic matter has high HI values (Peters, 1986); these values can be lowered by microbial oxidation (Meyers, 1997). In general, Hole 1082A sediments having lower Rock-Eval TOC values also have lower HI values (Fig. 26). This relationship confirms that the marine organic matter has been subject to partial oxidation, which simultaneously lowers TOC and HI values (Meyers, 1997). Further evidence of substantial amounts of in situ organic matter degradation exists in the large decreases in sulfate and increases in alkalinity and ammonia in the interstitial waters of Site 1082 sediments (see "Inorganic Geochemistry" section, this chapter).

The sediment samples have low Rock-Eval T_{max} values (Table 13), showing that their organic matter is thermally immature with respect to petroleum generation (Peters, 1986) and therefore is unlikely to contain much detrital organic matter derived from erosion of ancient sediments from Africa.

Table 11. Interstitial water composition for Hole 1082A.

Core, section, interval (cm)	Depth (mbsf)	pH	Alkalinity (mM)	Salinity	Cl^- (titr) (mM)	Cl^- (IC) (mM)	SO_4^{2-} (mM)	Na^+ (mM)	Mg^{2+} (mM)	Ca^{2+} (mM)	K^+ (mM)	H_4SiO_4 (µM)	NH_4^+ (µM)	PO_4^{3-} (µM)	Sr^{2+} (µM)
175-1082A-															
1H-1, 140-150	1.40	7.54	2.016	35.0	549	549	29.00	468	53.43	10.85	12.22	430	221	5	91
1H-2, 140-150	2.90	7.82	3.507	35.0	551	545	28.04	470	53.06	11.09	12.52	489	381	6	92
1H-3, 140-150	4.40	7.75	4.587	35.5	553	551	27.60	476	52.19	10.12	11.97	716	578	9	91
1H-4, 140-150	5.90	7.89	6.246	35.0	553	550	25.67	471	53.59	10.47	11.96	654	776	14	91
1H-5, 153-163	7.53	8.04		35.0	551	553	23.33		52.52	9.50	12.45	732	1,210	23	90
2H-1, 140-150	9.20	8.19	11.556	35.0	554	552	21.29	473	52.74	8.55	12.49	879	1,530	31	91
2H-2, 140-150	10.70	8.14	12.853	35.0	553	555	19.13	472	52.19	7.91	12.30	709	1,605	36	91
2H-3, 130-140	12.10	8.14	16.849	35.0	554	555	17.29	474	52.52	7.40	12.17	938	1,890	42	93
2H-4, 130-140	13.50	8.32	20.342	35.0	555	554	14.45	479	50.37	6.69	11.39	872	2,105	47	93
2H-5, 130-140	14.90	8.25	24.587	35.0	556	553	11.91	491	46.59	4.94	10.70	853	2,283	53	96
2H-6, 130-140	16.30	8.45	25.999	35.0	557	552	8.69	488	46.39	4.49	10.90	938	2,712	59	98
3H-1, 125-140	18.55	8.40	32.239	35.0	559	551	4.10	485	47.73	4.02	10.68	867	3,090	72	105
3H-2, 125-140	19.95	8.34	37.008	35.0	558	553	1.76	490	46.13	2.96	10.79	872	3,519	73	106
3H-3, 125-140	21.35	8.12	36.216	35.0	558	550	0.72	487	45.44	3.15	11.00	919	4,424	93	113
3H-4, 125-140	22.75	7.35	40.825	35.0	559	550	0.13	493	45.34	2.84	11.03	976	4,733	88	116
3H-5, 125-140	24.15	8.34	43.852	35.0	561	555	0.23	492	47.86	2.98	11.14	959	4,710	89	120
3H-6, 125-140	25.55	8.51		35.0	559	552	0.00		46.06	3.16	11.53	1016	5,971	92	120
4H-1, 125-140	28.05	7.35	45.156	35.0	559	542	0.15	493	46.64	3.28	11.42	1061	6,519	86	125
4H-2, 125-140	29.45	8.15	46.793	35.0	559	552	0.13	491	49.09	2.91	11.32	1004	6,257	90	125
4H-3, 125-140	30.85	7.97	48.302	35.0	555	554	0.00	492	46.61	3.39	11.67	1103	7,114	89	126
4H-4, 125-140	32.25	7.88	43.509	35.0	556	551	0.00	489	45.96	3.02	12.09	1096	7,852	87	125
4H-5, 125-140	33.65	7.96	47.269	35.0	555	553	0.00	494	45.41	2.75	12.27	1061	8,448	82	123
4H-6, 125-140	35.05	7.94	48.064	35.0	556	551	0.00	495	45.80	2.60	11.92	1092	8,400	89	124
5H-1, 125-140	37.55	7.55	43.423	35.0	558	552	1.31	496	44.68	3.22	11.53	1075	8,590	90	99
5H-2, 125-140	38.95	8.23	45.763	35.0	558	550	0.66	496	45.45	2.97	11.86	1137	9,733	88	114
5H-3, 125-140	40.35	7.91	48.316	35.0	556	552	0.93	500	44.41	2.61	12.43	1144	11,210	90	116
5H-4, 125-140	41.75	7.46	47.784	35.0	557	554	0.00	498	44.76	2.75	12.34	1174	10,781	98	120
5H-5, 125-140	43.15	7.35	39.002	35.5	557	553	0.06	485	46.25	2.89	12.23	1075	11,352	95	122
5H-6, 125-140	44.55	8.15	55.135	35.5	557	552	0.13	501	45.94	3.10	12.85	1163	12,733	102	125
6H-1, 125-140	47.05	7.96	55.255	35.5	558	554	0.00	502	45.83	3.40	12.85	1115	12,281	119	126
6H-2, 125-140	48.45	7.94	54.050	35.5	553	552	0.00	492	47.57	3.57	12.97	1125	12,019	116	125
6H-3, 125-140	49.85	8.29	55.272	35.5	549	551	0.00	493	45.89	3.07	13.50	1111	13,829	115	119
6H-4, 125-140	51.25	7.91	57.647	35.5	545	531	0.00	489	47.44	2.93	13.31	1139	13,948	129	125
6H-5, 125-140	52.65	7.32	61.405	35.5	551	552	0.00	498	47.55	3.26	13.37	1122	14,281	131	124
6H-6, 125-140	54.05	7.23	59.400	35.5	551	551	0.00	497	46.86	3.42	13.60	1167	14,210	137	129
7H-3, 135-150	59.65	7.60	68.916	36.0	552	566	0.33	502	49.33	3.68	13.19	1115	14,948	146	131
8H-4, 135-150	69.36	7.15		36.5	551	555	0.00		49.93	3.70	12.77	1049	16,448	161	142
9H-3, 115-130	78.45	7.62	72.381	36.5	553	554	0.01	508	48.47	3.53	13.26	1066	18,614	155	145
10H-4, 115-130	88.39	7.46	74.318	36.5	552	549	0.00	510	47.89	3.74	12.71	1025	17,733	151	153
11H-3, 120-135	97.50	7.02	72.443	36.5	550	548	0.30	513	44.23	3.95	13.62	1089	18,590	145	154
12H-4, 120-135	107.04	7.86	69.061	36.0	549	546	0.00	506	45.22	4.07	13.48	1103	21,400	147	164
15X-2, 135-150	131.07	7.28	75.106	35.5	547	550	0.03	518	40.49	4.66	13.78	1217	23,995	124	183
18X-2, 135-150	160.10	7.38	75.592	36.0	547	548	0.02	521	39.06	4.86	14.12	1217	24,829	106	197
21X-3, 135-150	189.77	7.56	72.590	36.0	550	553	0.08	526	36.13	5.27	13.99	1212	25,567	103	211
24X-3, 135-150	219.61	6.97	71.262	36.0	549	549	0.00	525	35.98	5.32	12.97	1255	23,138	109	228
27X-3, 135-150	248.75	7.89	71.935	36.0	553	556	0.06	530	35.25	5.89	13.34	1286	25,281	87	244
30X-3, 135-150	277.65	7.86	61.543	35.5	559	555	1.56	528	35.56	5.70	13.39	1271	24,210	66	208
33X-3, 139-154	306.49	7.89	61.730	35.5	563	565	0.09	539	31.01	5.57	13.18	1399	25,567	53	286
37X-3, 135-150	334.04	7.91	55.398	35.5	564	574	0.04	534	29.88	6.18	13.74	1323	24,305	36	304
40X-5, 135-150	365.04	7.86	50.650	35.5	565	565	0.00	536	26.89	6.40	12.95	1501	24,019	25	344
43X-3, 135-150	392.34	7.87	39.724	35.0	569	571	0.00	537	23.89	5.75	12.43	1290	22,400	11	352
46X-2, 135-150	420.55	7.21	35.876	35.0	572	575	0.08	534	23.97	7.05	11.52	1321	20,924	8	405
50X-4, 135-150	461.61	7.02	31.369	34.5	578	584	0.15	535	23.51	8.50	10.62	1222	18,043	5	482
53X-3, 135-150	489.05	7.20		34.0	585	592	0.00		23.97	7.82	10.39	1401	16,995	6	448
56X-4, 135-150	518.78	6.96	24.010	35.0	589	601	0.00	543	21.07	8.90	9.31	1470	27,257	4	574
60X-4, 135-150	557.59	6.96	19.971	35.0	595	601	0.12	539	24.29	9.83	7.90	1231	25,424	4	580
63X-4, 135-150	586.15	6.95	16.788	35.0	598	607	0.00	536	24.54	11.12	7.33	1189	23,852	3	626

Notes: Cl^- (titr) = analyzed by titration and Cl^- (IC) = analyzed by ion chromatography. Empty cells = not analyzed.

Headspace Gases

Relatively high amounts of hydrogen sulfide, methane, and CO_2 were found in sediments from Site 1082. The odor of hydrogen sulfide was noted in Cores 175-1082A-2H through 13H (1.5–120 mbsf), and detectable concentrations of this gas were occasionally found throughout Hole 1082A (Table 14). Total gas pressures became great enough in sediments below Core 175-1082A-2H (17 mbsf) to require perforating the core liner to relieve the pressure and prevent excessive core expansion.

Methane (C_1) first appears in headspace gas samples of Hole 1082A sediments at 4.5 mbsf. Concentrations become significant in sediments below 20 mbsf (Fig. 27). As at Site 1081, high methane/ethane (C_1/C_2) ratios and the absence of major contributions of higher molecular weight hydrocarbon gases (Table 14) indicate that the gas is biogenic, as opposed to thermogenic, in origin. A biogenic origin of methane is supported by the disappearance of interstitial sulfate at approximately the same sub-bottom depth where methane concentrations begin to rise (see "Inorganic Geochemistry" section, this chapter), inasmuch as Claypool and Kvenvolden (1983) observe that the presence of interstitial sulfate inhibits microbial methanogenesis in marine sediments.

Natural gas analyses determined that the most abundant gas was CO_2 and that headspace concentrations of this gas remained high deep in Hole 1082A (586 mbsf; Fig. 28). Cragg et al. (1992) report the existence of viable microbes to depths of ~500 mbsf in the sediments of the Japan Sea. The abundance of biogenic gases in sediments from Site 1082 suggests the presence of viable microbial communities to similar sub-bottom depths on the Walvis Ridge.

PHYSICAL PROPERTIES

Index properties (gravimetric wet bulk density, porosity, and moisture content) were generally determined on one or two samples (volume = ~10 cm^3) per working-half section on all cores from Hole

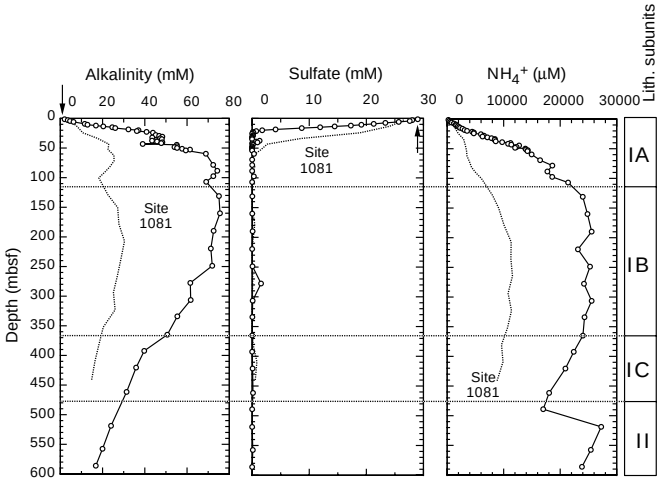

Figure 17. Downcore profiles of dissolved alkalinity, sulfate, and ammonium at Site 1082 (solid lines with open circles). Lithostratigraphic subunits shown on right-hand bar. Profile measured at Site 1081 (dotted lines) is shown for comparison. Arrows = mean ocean-bottom-water values taken from Millero and Sohn (1992).

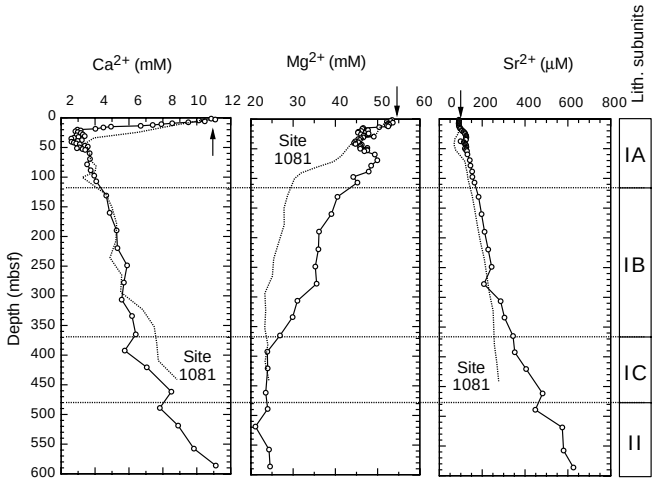

Figure 18. Downcore profiles of Ca^{2+}, Mg^{2+}, and Sr^{2+} at Site 1082 (solid lines with open circles). Lithostratigraphic subunits shown on right-hand bar. Profile measured at Site 1081 (dotted lines) is shown for comparison. Arrows = mean ocean-bottom-water values taken from Millero and Sohn (1992).

1082A using Method C (see "Explanatory Notes" chapter, this volume).

Other shipboard physical properties measurements included determination of compressional (*P*-wave) ultrasonic velocity, density, magnetic susceptibility, and natural gamma radiation with the MST system on whole-round sections of cores from each hole (see "Explanatory Notes" chapter, this volume).

Compressional (*P*-wave) velocity and undrained vane shear strength measurements were conducted on the working half of every section from Hole 1082A. Sampling resolution was one or two sample points per section. For the discrete *P*-wave measurements, the modified Hamilton Frame was used to determine ultrasonic velocities. Thermal conductivity was measured on every second section in every core from Hole 1082A.

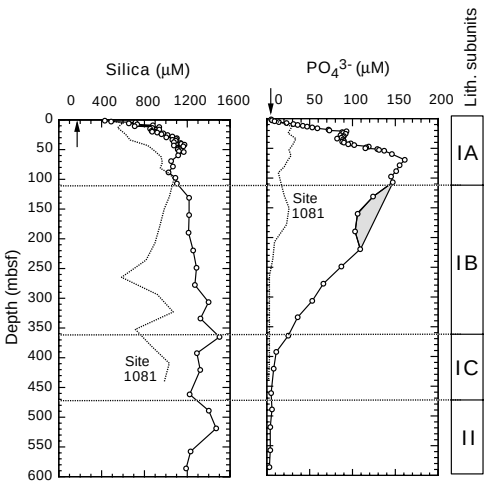

Figure 19. Downcore profiles of dissolved silica and phosphate at Site 1082 (solid lines with open circles). Profile measured at Site 1081 (dotted lines) is shown for comparison. Lithostratigraphic subunits shown on right-hand bar. Shaded region = depth zone of increased dissolved phosphate removal. Arrows = mean ocean-bottom-water values taken from Millero and Sohn (1992).

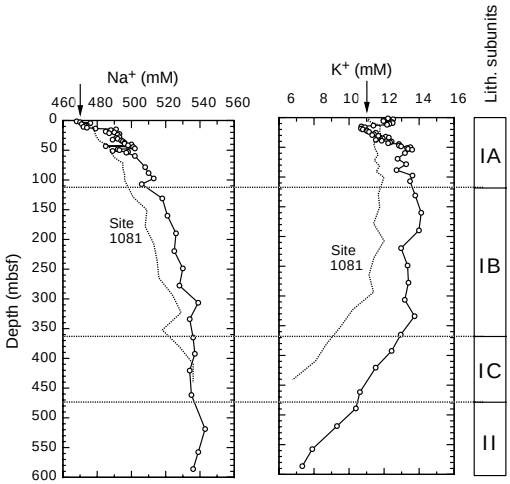

Figure 20. Downcore profiles of dissolved Na^+ and K^+ at Site 1082 (solid lines with open circles). Profile measured at Site 1081 (dotted lines) is shown for comparison. Lithostratigraphic subunits shown on right-hand bar. Arrows = mean ocean-bottom-water values taken from Millero and Sohn (1992).

Multisensor Track

P-wave velocities (Fig. 29), GRAPE density (Fig. 30), and magnetic susceptibility (Figs. 31A) were determined every 2 cm for the first nine cores (0–90 mbsf); natural gamma radiation was measured with a sampling period of 30 s at 30-cm resolution during that depth interval (Figs. 31B). MST data are included on CD-ROM (back pocket, this volume). Below 90 mbsf, the resolution was reduced to 32 cm for the latter, whereas the other sensors were run at 4-cm resolution. Compressional velocities were recorded at a threshold of 100 incremental units to exclude weaker signals from the profile. No signals

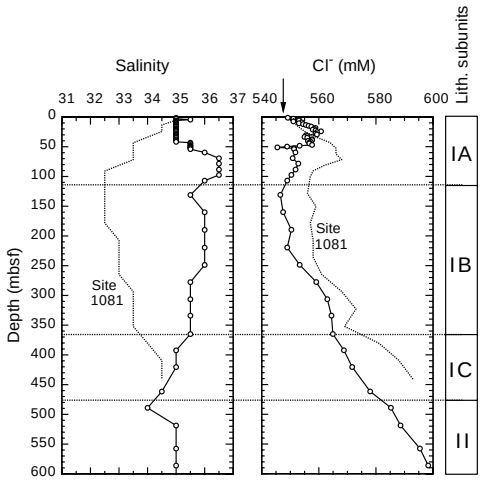

Figure 21. Downcore profiles of salinity and dissolved Cl^- at Site 1082 (solid lines with open circles). Profile measured at Site 1081 (dotted lines) is shown for comparison. Lithostratigraphic subunits shown on right-hand bar. Arrow = mean ocean-bottom-water value taken from Millero and Sohn (1992).

were recorded with the MST *P*-wave logger below 30 mbsf because of numerous cracks and voids within the cored sediments (Fig. 29). MST *P*-wave values appear to be systematically lower than discrete velocity values, but they reveal some correlation.

Magnetic susceptibility (Figs. 31A) and natural gamma radiation (Figs. 31B) correlate well over the entire depth range of 600 m, although on a smaller depth scale, differences between the two profiles are apparent. GRAPE density and index properties wet bulk density fit very well together (Fig. 30), although the index properties values are generally higher. This difference can be attributed to gas expansion affecting most parts of each core and reducing the total sediment volume measured with the GRAPE. All physical properties data sets reveal clear and pronounced cyclicities, opening opportunities for future high-resolution studies. However, thorough editing will be required to correct for sediment deformation caused by gas expansion, to combine parallel holes, and to prepare data for time-series analysis methods.

Velocities

Discrete velocities range from 1520 to 1605 m/s between 0 and 48 mbsf. The *P*-wave logger of the MST generated lower values down to 30 mbsf, where signal attenuation becomes too high to determine first arrivals (Fig. 29). The discrete velocity profile correlates well with the undrained vane shear strength values, which may give an indication of the sediment deformation during core retrieval caused by gas expansion (Figs. 29).

Index Properties

Results of discrete measurements of wet bulk density, porosity, and moisture content are presented in Figures 32A, 32B, and 32C, respectively (also see Table 15 on CD-ROM, back pocket, this volume). The density values vary between 1250 and 1800 kg/m^3. The overall trend of the wet bulk density profile shows increasing values because of compaction. However, a smooth long-term variability exists in the advanced APC section. A decrease in wet bulk density can be identified (e.g., from 40 to 80 mbsf), indicating a major compositional change.

In general, porosity and moisture profiles show the expected inverse correlation with the density curve. Porosities decrease from 82% in the top section to 50% at 530 mbsf (Fig. 32B), and moisture content varies between 65% at the top of Hole 1082A and 30% to 530 mbsf (Fig. 32C).

Thermal Conductivity

The thermal conductivity profile (Figs. 31C) at Hole 1082A was measured in every second core section (see "Explanatory Notes" chapter, this volume). The profile shows a better degree of similarity with the magnetic susceptibility (Figs. 31A) than with the natural gamma radiation profile (Figs. 31B).

Vane Shear Strength

Undrained vane-shear measurements were performed in the bottom part of each core section. The profile between 0 and 200 mbsf shows a gradual increase in vane shear from the top of Hole 1082A to 100 mbsf, followed by a decrease in shear strength. The low shear-strength values below 118 mbsf are probably related to the change from APC to XCB drilling. XCB cores are generally biscuited and contain a surplus of pore fluid as an effect of the drilling process. Figure 31A–D shows a comparison of shear strength with magnetic susceptibility, natural gamma radiation, and thermal conductivity. Local maxima in shear strength are usually found in the middle of each section. Lower values coincide with the top and the bottom of each section where gas expansion may have changed the sediment structure most.

DOWNHOLE LOGGING

Hole 1082A was logged with a full suite of sensors to continuously characterize the sedimentary changes, to correlate and compare the lithostratigraphy with that for Hole 1081A, and to provide data for core-log integration (coring disturbance) and correlation with the seismic profile using synthetic seismograms.

Logging Operations

Hole 1082A was logged with four different tool strings. The first tool string (seismostratigraphy) included the NGT, DIT, and TLT sondes. The second tool string (lithoporosity) included the NGT, neutron porosity, gamma density, and TLT sondes. The third tool string (FMS, 2 passes) included the NGT, inclinometry, and FMS sondes. The fourth tool string (GHMT) included the NGT, magnetic susceptibility, and vertical component magnetometer sondes. The logs were run uphole from 600 mbsf (total depth) to pipe at 64 mbsf; the two first runs were logged to the seafloor. Natural gamma radiation is the only parameter measurable through the pipe, but it should be interpreted only qualitatively in this interval. For each run, the pipe was set at 93 mbsf and pulled up to ~64 mbsf during logging. The wireline logging heave compensator was started immediately upon entering the hole.

Data Quality and General Results

Hole 1082A is characterized by a regular hole diameter size of ~10 to 11 in with numerous small enlargements from 530 to 120 mbsf (see caliper measurements; Fig. 33). Above and below this interval, the hole conditions are degraded, and some of the downhole measurements are affected by wide enlargements at the bottom and by wash-

Table 12. Percentages of inorganic and total carbon, total nitrogen, and total sulfur in sediment samples from Hole 1082A.

Core, section, interval (cm)	Depth (mbsf)	IC (wt%)	$CaCO_3$ (wt%)	TC (wt%)	TOC (wt%)	TN (wt%)	TS (wt%)	C/N (atomic)
175-1082A-								
Subunit IA - Pleistocene nannofossil- and foraminifer-rich clay								
1H-1, 46-47	0.46	8.03	66.9					
1H-3, 46-47	3.46	6.16	51.3	11.83	5.67	0.58	0.65	11.5
1H-5, 46-47	6.46	6.13	51.1					
2H-1, 46-47	8.26	5.92	49.3					
2H-3, 46-47	11.26	7.19	59.9	10.37	3.18	0.29	0.52	13.1
2H-5, 46-47	14.06	7.82	65.2					
3H-1, 46-47	17.76	3.95	32.9					
3H-3, 46-47	20.56	5.22	43.5	8.89	3.67	0.35	1.09	12.2
3H-5, 46-47	23.36	2.72	22.7					
4H-1, 46-47	27.26	7.24	60.3					
4H-3, 46-47	30.06	7.90	65.8	11.14	3.24	0.27	0.56	14.2
4H-5, 46-47	32.86	7.53	62.7					
5H-1, 46-47	36.76	9.16	76.3					
5H-3, 46-47	39.56	6.90	57.5	9.55	2.65	0.24	0.91	12.9
5H-5, 46-47	42.36	7.51	62.5					
5H-5, 80-81	42.70	7.48	62.3	10.50	3.02	0.26	0.70	13.8
5H-6, 112-113	44.42	5.94	49.5	11.03	5.10	0.40	1.48	14.7
5H-7, 30-31	45.00	7.85	65.4	11.30	3.45	0.29	0.87	14.1
6H-1, 46-47	46.26	6.06	50.5	10.34	4.28	0.38	1.29	13.1
6H-2, 65-66	47.85	6.89	57.4	10.13	3.25	0.29	0.94	13.2
6H-3, 46-47	49.06	6.25	52.1	10.73	4.48	0.36	1.20	14.6
6H-3, 65-66	49.25	6.34	52.8	10.63	4.29	0.36	1.20	13.9
6H-4, 6-7	50.06	4.61	38.4	10.40	5.79	0.47	1.85	14.4
6H-4, 65-66	50.65	5.00	41.7	9.90	4.90	0.41	1.64	13.9
6H-4, 110-111	51.10	4.45	37.1	12.06	7.61	0.56	2.04	15.8
6H-5, 7-8	51.47	4.35	36.3	12.08	7.73	0.56	2.01	16.1
6H-5, 65-66	52.05	1.82	15.2	14.15	12.33	0.87	3.07	16.6
6H-5, 104-105	52.44	6.48	53.9	10.00	3.53	0.31	1.04	13.3
6H-6, 20-21	53.00	4.93	41.1	12.41	7.48	0.52	1.81	17.0
6H-6, 100-101	53.80	2.81	23.4	12.23	9.41	0.67	2.54	16.5
6H-7, 20-21	54.40	2.91	24.2	12.20	9.30	0.66	2.46	16.5
6H-7, 60-61	54.80	2.25	18.7	12.95	10.70	0.93	3.16	13.4
7H-1, 9-10	55.39	3.75	31.2	8.61	4.86	0.39	2.04	14.5
7H-1, 56-57	55.86	3.46	28.8	8.99	5.53	0.46	2.16	14.2
7H-3, 23-24	58.53	3.84	32.0	9.29	5.45	0.42	1.88	15.2
7H-3, 104-105	59.34	3.88	32.3	9.76	5.89	0.45	2.08	15.4
7H-4, 23-24	60.03	3.69	30.8	10.59	6.89	0.50	2.02	16.3
7H-4, 89-90	60.69	0.87	7.2	16.95	16.08	1.04	4.30	18.2
7H-4, 103-104	60.83	1.94	16.1	13.99	12.05	0.83	3.44	17.0
7H-5, 69-70	61.99	2.70	22.5	12.31	9.61	0.64	2.54	17.6
7H-6, 45-46	63.25	8.15	67.9	11.71	3.55	0.28	0.79	15.1
7H-6, 129-130	64.09	3.64	30.4	10.98	7.34	0.52	2.14	16.6
8H-3, 46-47	66.97	3.80	31.6					
8H-5, 46-47	69.97	2.84	23.6	10.52	7.68	0.54	2.19	16.7
8H-5, 119-120	70.70	5.33	44.4					
9H-1, 46-47	74.76	6.98	58.2					
9H-5, 46-47	80.56	5.14	42.9	10.68	5.53	0.40	1.17	16.3
10H-5, 46-47	89.00	3.58	29.8	6.93	3.35	0.27	1.28	14.4
11H-1, 46-47	93.76	4.04	33.7					
11H-3, 46-47	96.76	7.01	58.4	12.44	5.44	0.40	1.26	16.1
11H-5, 46-47	99.61	4.96	41.3					
12H-2, 46-47	103.60	2.71	22.6	6.36	3.64	0.32	1.74	13.2
12H-3, 46-47	104.97	2.91	24.3					
12H-5, 46-47	107.65	2.84	23.6					
Subunit IB - Pliocene-Pleistocene diatom-rich clay								
13H-1, 46-47	112.76	4.09	34.1					
13H-3, 46-47	114.88	3.72	31.0	8.09	4.37	0.40	1.77	12.9
13H-5, 46-47	117.59	5.47	45.6					
14H-1, 46-47	122.26	6.77	56.4	9.39	2.62	0.24	0.95	12.9
14H-3, 46-47	125.26	3.69	30.7	6.71	3.02	0.26	1.23	13.7
14H-4, 140-141	127.70	4.54	37.8	9.48	4.94	0.39	1.47	14.9
14H-4, 149-150	127.79	4.37	36.4	10.20	5.83	0.42	1.55	16.4
14H-5, 10-11	127.90	4.39	36.5	10.29	5.90	0.44	1.68	15.8
14H-5, 20-21	128.00	4.03	33.5	9.45	5.43	0.42	2.00	15.1
14H-5, 30-31	128.10	3.82	31.8	9.42	5.60	0.41	1.61	15.8
14H-5, 40-41	128.20	5.63	46.9	8.53	2.91	0.27	0.96	12.5
14H-5, 50-51	128.30	5.86	48.8					
15X-1, 46-47	129.06	5.90	49.1	8.84	2.94	0.27	1.24	12.9
15X-3, 46-47	131.68	3.35	27.9	7.22	3.87	0.33	1.41	13.6
15X-4, 45-47	132.77	2.49	20.8					
16X-1, 46-47	138.76	6.12	51.0	9.80	3.68	0.31	1.02	13.7
16X-2, 10-11	139.90	3.96	33.0					
16X-2, 25-26	140.05	4.05	33.7	10.28	6.23	0.45	1.52	16.1
16X-3, 46-47	141.76	5.33	44.4					
16X-3, 130-131	142.60	5.80	48.3	8.27	2.47	0.23	0.55	12.7
16X-3, 145-146	142.75	6.67	55.5	8.94	2.28	0.21	0.72	12.6
16X-5, 46-47	144.76	3.68	30.6					
17X-1, 46-47	148.36	3.50	29.1	8.89	5.40	0.43	1.59	14.8
18X-1, 46-47	158.06	1.71	14.3	6.73	5.02	0.44	1.84	13.2
18X-3, 46-47	160.71	2.89	24.1					
19X-2, 46-47	167.97	2.04	17.0	6.27	4.23	0.35	1.56	14.0
20X-5, 46-47	182.20	1.42	11.9	5.93	4.51	0.35	1.72	14.9
21X-3, 46-47	188.88	1.22	10.2	6.02	4.80	0.41	1.91	13.6
22X-1, 46-47	196.66	3.03	25.2					
22X-3, 46-47	199.28	3.17	26.4	6.10	2.94	0.24	0.86	14.1
23X-1, 46-47	206.36	2.61	21.8					
23X-3, 46-47	208.52	1.85	15.4	9.66	7.81	0.54	2.06	17.0
24X-1, 46-47	215.96	4.48	37.3					
24X-3, 46-47	218.72	4.99	41.6	7.95	2.96	0.28	0.97	12.4
24X-5, 46-47	221.75	2.98	24.8					
25X-1, 46-47	225.66	3.79	31.5	10.43	6.64	0.49	1.63	16.0
25X-3, 46-47	228.64	4.61	38.4					
26X-1, 46-47	235.26	3.78	31.5					
26X-3, 46-47	238.26	2.46	20.5	5.85	3.39	0.26	0.86	15.0
26X-5, 46-47	241.26	2.86	23.8					
27X-1, 46-47	244.86	1.85	15.4	8.36	6.51	0.48	2.01	15.7
27X-3, 46-47	247.86	0.10	0.8					
27X-5, 46-47	250.83	2.18	18.2					
28X-1, 46-47	254.46	3.17	26.4					
28X-3, 46-47	257.46	3.90	32.5	7.51	3.61	0.30	1.10	14.0
28X-5, 46-47	260.36	3.87	32.2					
29X-1, 46-47	264.06	2.86	23.8					
29X-3, 46-47	267.06	4.50	37.5					
29X-5, 46-47	270.06	3.98	33.2	7.61	3.62	0.34	1.40	12.5
30X-1, 46-47	273.76	4.71	39.2					
30X-3, 46-47	276.76	3.78	31.5					
30X-5, 46-47	279.76	1.94	16.2	5.66	3.72	0.29	1.12	15.2
31X-1, 46-47	283.36	2.91	24.2					
31X-3, 46-47	285.38	3.55	29.6					
31X-5, 46-47	288.02	4.60	38.3	7.94	3.33	0.29	0.99	13.5
32X-1, 46-47	292.96	4.48	37.3					
32X-3, 46-47	295.96	6.15	51.2	8.13	1.99	0.19	0.66	12.4
32X-5, 46-47	298.96	3.70	30.8					
33X-1, 46-47	302.56	4.18	34.8					
33X-3, 46-47	305.56	3.53	29.4					
33X-5, 46-47	308.60	1.67	13.9	5.10	3.43	0.26	1.71	15.4
34X-1, 46-47	312.16	5.67	47.3					
34X-3, 46-47	315.18	5.39	44.9	7.42	2.03	0.18	0.60	13.4
35X-1, 46-47	321.86	6.51	54.3					
35X-3, 46-47	324.86	5.86	48.8	8.25	2.39	0.22	0.64	12.9
35X-5, 46-47	327.86	5.59	46.5					
36X-1, 46-47	327.96	4.21	35.1					
37X-3, 46-47	333.15	4.52	37.6	8.88	4.36	0.33	1.19	15.3
37X-5, 46-47	336.15	4.57	38.1					
38X-1, 46-47	341.06	4.22	35.2	7.16	2.94	0.26	0.96	13.0
38X-3, 46-47	344.06	5.95	49.6					
38X-5, 46-47	347.06	4.17	34.7					
39X-1, 45-46	350.75	4.53	37.8	7.68	3.15	0.28	0.94	13.0
40X-2, 46-47	360.78	4.90	40.9					
40X-5, 46-47	364.15	3.75	31.2	7.61	3.87	0.32	1.17	14.2
Subunit IC - Pliocene nannofossil clay								
41X-1, 46-47	369.96	5.37	44.7					
41X-3, 46-47	372.96	6.54	54.4	11.30	4.76	0.70	2.58	8.0
41X-3, 120-121	373.70	1.17	9.7					
41X-4, 46-47	374.46	4.01	33.4					
42X-1, 46-47	379.66	7.30	60.8	8.97	1.66	0.19	1.19	10.4
42X-3, 46-47	382.66	6.81	56.7					
42X-5, 46-47	385.66	5.85	48.7					
43X-1, 46-47	389.26	6.70	55.9					
43X-3, 46-47	391.45	5.61	46.7	9.11	3.50	0.29	1.05	14.0
43X-5, 46-47	394.45	7.15	59.5					
44X-1, 45-46	398.85	5.52	46.0					
44X-3, 46-47	401.86	7.81	65.0	9.17	1.36	0.15	0.55	10.9
44X-5, 46-47	404.86	8.80	73.3					
45X-1, 46-47	408.56	7.28	60.6					
45X-3, 46-47	411.56	7.32	61.0	9.09	1.77	0.17	0.15	12.1
45X-5, 46-47	414.40	5.83	48.6	7.91	2.08	0.21	0.85	11.4
46X-1, 46-47	418.16	4.99	41.6	8.75	3.76	0.30	1.10	14.6
46X-3, 46-47	421.16	4.70	39.1	6.74	2.04	0.20	0.95	11.6
46X-5, 46-47	423.10	5.91	49.3					
47X-1, 46-47	427.76	7.06	58.8	8.97	1.91	0.17	0.58	13.1
47X-3, 46-47	430.76	4.98	41.5	8.52	3.54	0.28	1.28	14.8
48X-1, 46-47	437.46	7.24	60.3	8.67	1.43	0.15	0.59	11.3
48X-3, 46-47	440.46	7.81	65.1	8.62	0.80	0.12	0.44	7.5
49X-1, 46-47	447.16	7.07	58.9					
49X-3, 46-47	450.22	6.27	52.2	7.70	1.43	0.17	0.98	9.9
49X-5, 46-47	453.30	6.47	53.9	8.23	1.76	0.18	0.88	11.4
50X-3, 46-47	459.22	6.69	55.7	8.94	2.25	0.20	0.60	13.0
50X-5, 46-47	462.22	4.76	39.7	6.76	2.00	0.23	1.00	10.3
51X-1, 46-47	466.36	5.20	43.3	9.33	4.14	0.28	1.15	17.4
51X-3, 46-47	469.36	7.55	62.9	9.02	1.47	0.15	0.27	11.3
Unit II - Miocene-Pliocene nannofossil ooze								
52X-1, 46-47	475.56	8.96	74.7					
52X-3, 46-47	478.15	8.68	72.3	9.65	0.98	0.12	0.56	9.8
52X-5, 46-47	481.15	8.86	73.8	9.48	0.62	0.11	0.12	6.7
53X-1, 104-105	485.74	7.06	58.8	7.82	0.76	0.12	0.44	7.6
53X-3, 46-47	488.16	8.35	69.6					
53X-5, 46-47	491.16	7.55	62.9	8.03	0.48	0.11	0.15	5.1
54X-1, 46-47	494.86	7.31	60.9					
54X-3, 46-47	497.04	6.30	52.5	7.27	0.96	0.14	0.25	8.2
54X-5, 46-47	500.04	6.40	53.3	8.56	2.16	0.19	0.29	13.4
55X-1, 46-47	504.56	5.52	46.0	6.60	1.07	0.13	0.43	9.7
55X-3, 46-47	507.21	5.42	45.2					
55X-5, 46-47	510.21	6.23	51.9					
56X-1, 46-47	514.26	6.78	56.5	7.14	0.37	0.10	0.30	4.2
56X-3, 46-47	516.39	7.22	60.2					

Table 12 (continued).

Core, section, interval (cm)	Depth (mbsf)	IC (wt%)	$CaCO_3$ (wt%)	TC (wt%)	TOC (wt%)	TN (wt%)	TS (wt%)	C/N (atomic)
56X-5, 46-47	519.39	6.91	57.5	8.31	1.41	0.14	0.46	11.3
57X-3, 46-47	526.49	6.59	54.9	7.78	1.19	0.14	0.27	9.7
57X-5, 46-47	529.49	6.92	57.7	8.72	1.79	0.20	0.81	10.7
58X-1, 46-47	533.56	7.83	65.2					
58X-3, 46-47	536.56	7.75	64.6	8.46	0.71	0.09	0.13	9.5
58X-5, 46-47	539.56	7.74	64.5	8.30	0.56	0.09	0.21	7.2
59X-1, 47-48	543.27	9.07	75.5	9.44	0.37	0.07	0.10	6.1
59X-3, 49-50	546.29	9.23	76.9	9.41	0.18	0.06	0.14	3.5
59X-5, 48-49	549.24	9.43	78.6					
60X-1, 21-22	552.61	9.08	75.6	10.09	0.66	0.11	0.29	7.0
60X-3, 50-51	555.24	9.09	75.7					
60X-5, 45-46	558.19	8.98	74.8	9.49	0.51	0.08	0.23	7.8
61X-1, 46-47	562.46	10.31	85.8					
61X-3, 46-47	565.36	9.73	81.1	9.77	0.04	0.06	0.23	0.7
61X-5, 46-47	568.33	9.52	79.3	9.55	0.03	0.06	0.21	0.6
62X-1, 46-47	572.16	7.98	66.5	8.21	0.23	0.08	0.63	3.4
62X-3, 46-47	575.16	8.49	70.7					
62X-5, 46-47	578.16	7.39	61.5	7.64	0.25	0.09	1.00	3.3
63X-1, 46-47	581.76	8.46	70.5					
63X-3, 46-47	583.76	8.58	71.5	8.98	0.40	0.10	0.27	4.9
63X-5, 46-47	586.76	9.13	76.1					
64X-1, 46-47	591.36	7.83	65.2					
64X-3, 38-40	594.28	9.14	76.1					
64X-5, 42-44	597.32	7.75	64.6	8.26	0.51	0.11	0.55	5.6

Notes: IC = inorganic carbon; $CaCO_3$ = calcium carbonate; TC = total carbon; TOC = total organic carbon; TN = total nitrogen; TS = total sulfur; and C/N = carbon/nitrogen ratio. TOC concentrations are calculated from the difference between IC and TC concentrations. C/N ratios are calculated from TOC and TN concentrations and are given as atom/atom ratios.

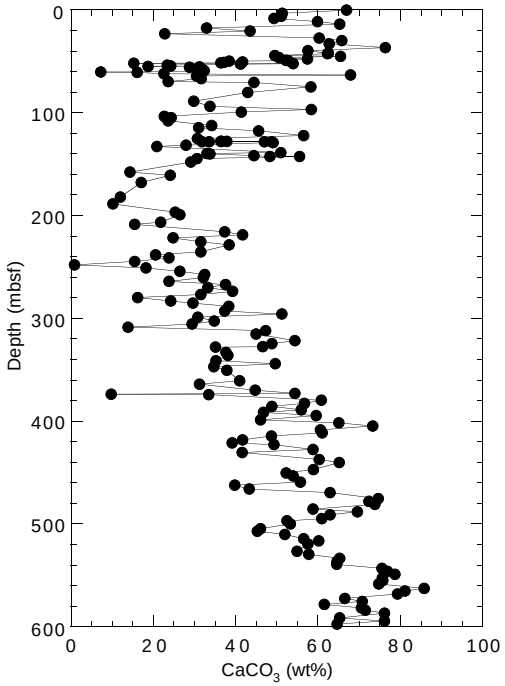

Figure 22. Concentrations of $CaCO_3$ in sediments from Hole 1082A.

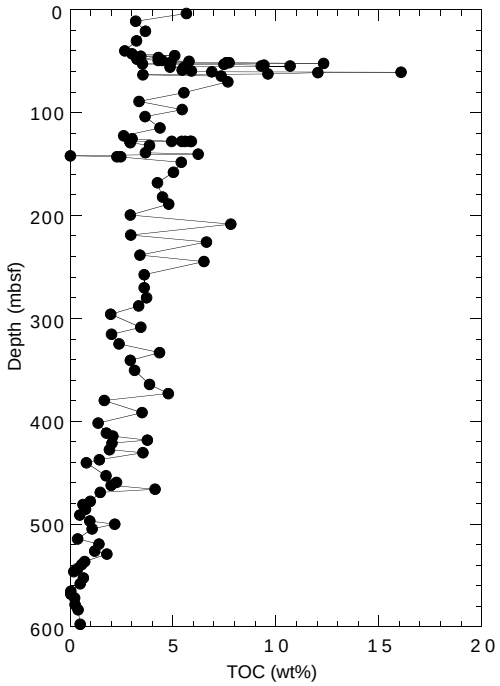

Figure 23. Concentrations of TOC in sediments from Hole 1082A.

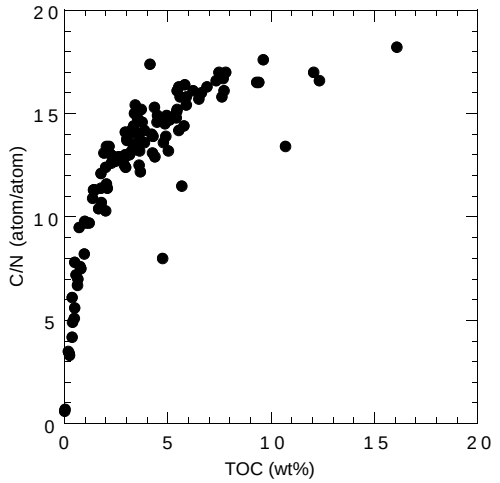

Figure 24. Comparison of organic matter C/N ratios and TOC concentrations of sediments from Hole 1082A. The correspondence between increases in both parameters indicates that preservation of marine organic matter during early diagenesis is important to enhancing the organic carbon richness of sediments on the Walvis Ridge.

out zones at the top of the logged interval. Consequently, only the logging measurements in the 530–120 mbsf interval are of reliable quality.

The lithologic succession recovered from Hole 1082A is controlled mainly by changes in the nature and intensity of biogenic production vs. the type and amount of detrital input and is characterized by large changes in sediment composition and compaction, which should be reflected in the log physical properties measurements. The lithostratigraphic boundaries defined from core observation and smear-slide studies (see "Lithostratigraphy" section, this chapter) partially fit with the main features observed in the downhole measurements. The boundary between lithostratigraphic Subunits ID and IC at 475 mbsf is identified in the log data as a sharp increase in gamma-ray intensity (potassium and thorium), magnetic susceptibility, and uranium (U) content (Fig. 33). At the boundary between Subunits ID and IC, the downhole measurements show a 30-m-thick interval from 500 to 470 mbsf characterized by low gamma-ray intensity, resistivity, magnetic susceptibility, and U content and by high velocity and density. In the middle of this layer (~490 mbsf), the signals are dominated by the presence of two thick dolomitic layers. Similarly, the increased opal content of Subunit IB is reflected in the downhole measurements above 320 mbsf. This depth is marked by a major

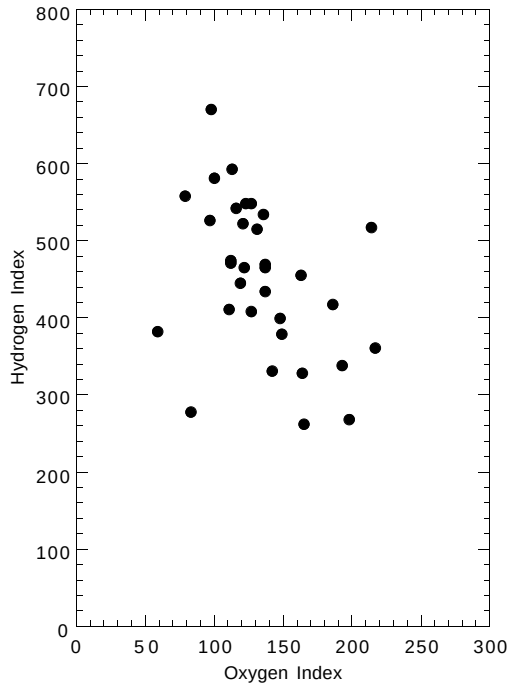

Figure 25. Rock-Eval Van Krevelen–type diagram of sediments from Hole 1082A. Organic matter appears to be type II algal material that has been variably oxidized. HI = milligrams of hydrocarbons per gram of organic carbon; OI = milligrams of CO_2 per gram of organic carbon.

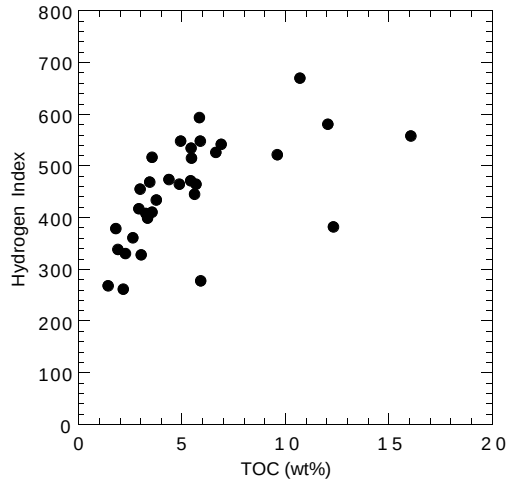

Figure 26. Comparison of Rock-Eval HI values and TOC concentrations of sediments from Hole 1082A. The correspondence between increases in both parameters indicates that preservation of marine organic matter is important to enhancing the organic carbon richness of sediments on the Walvis Ridge.

change in the downhole measurements toward lower values, except for the U content, which progressively increases from 320 mbsf. Between 320 and 180 mbsf, the gamma-ray intensity, which is well correlated with the U content, has a lower frequency signal. This fact is associated with the low resistivity in this interval of opal-rich sediment (see "Biostratigraphy and Sedimentation Rates" section, this chapter) and suggests a higher sedimentation rate. The velocity and density also exhibit a regular decrease uphole, with a step at 320 mbsf, caused by progressive compaction of the sediment with depth.

Table 13. Results of Rock-Eval pyrolysis analyses of sediments from Hole 1082A.

Core, section, interval (cm)	Depth (mbsf)	TOC (wt%)	S_1	S_3	S_3	T_{max} (°C)	HI	OI
175-1082A-								
Subunit IA - Pleistocene nannofossil- and foraminifer-rich clay								
1H-3, 46-47	3.46	5.67	2.82	26.41	6.96	412	465	122
4H-3, 46-47	30.06	3.24	0.97	13.24	4.13	412	408	127
5H-7, 30-31	45.00	3.45	1.12	16.21	4.74	413	469	137
6H-5, 65-66	52.05	12.33	3.15	47.14	7.34	409	382	59
6H-7, 60-61	54.80	10.70	13.44	71.79	10.51	401	670	98
7H-1, 9-10	55.39	4.86	1.82	22.60	6.68	411	465	137
7H-3, 23-24	58.53	5.45	3.39	28.12	7.16	400	515	131
7H-3, 104-105	59.34	5.89	2.16	32.28	7.49	414	548	127
7H-4, 23-24	60.03	6.89	2.61	37.37	8.03	410	542	116
7H-4, 89-90	60.69	16.08	10.49	89.76	12.83	408	558	79
7H-4, 103-104	60.83	12.05	5.47	70.07	12.07	411	581	100
7H-5, 69-70	61.99	9.61	4.63	50.21	11.70	407	522	121
7H-6, 45-46	63.25	3.55	1.77	18.37	7.60	410	517	214
11H-3, 46-47	96.76	5.44	2.07	29.09	7.41	404	534	136
Subunit IB - Pliocene-Pleistocene diatom-rich clay								
14H-1, 46-47	122.26	2.62	0.53	9.48	5.70	415	361	217
14H-3, 46-47	125.26	3.02	0.83	9.91	4.98	407	328	164
14H-4, 140-141	127.70	4.94	1.66	27.08	6.11	409	548	123
14H-4, 149-150	127.79	5.83	4.03	34.58	6.61	398	593	113
14H-5, 10-11	127.90	5.90	1.29	16.44	4.95	408	278	83
14H-5, 20-21	128.00	5.43	2.21	25.61	6.11	402	471	112
14H-5, 30-31	128.10	5.60	1.24	24.92	6.68	413	445	119
14H-5, 40-41	128.20	2.91	0.69	12.14	5.42	414	417	186
15X-1, 46-47	129.06	2.98	0.79	13.57	4.86	413	455	163
25X-1, 46-47	225.66	6.64	2.41	34.98	6.49	403	526	97
31X-5, 46-47	288.02	3.33	0.84	13.31	4.95	409	399	148
37X-3, 46-47	333.15	4.36	2.12	20.67	4.91	399	474	112
Subunit IC - Pliocene nannofossil clay								
46X-1, 46-47	418.16	3.76	0.76	16.35	5.16	415	434	137
47X-1, 46-47	427.76	1.91	0.39	6.46	3.70	413	338	193
47X-3, 46-47	430.76	3.54	0.73	14.56	3.95	413	411	111
50X-3, 46-47	459.22	2.25	0.48	7.46	3.20	415	331	142
Unit II - Miocene-Pliocene nannofossil ooze								
54X-5, 46-47	500.04	2.16	0.45	5.66	3.58	420	262	165
56X-5, 46-47	519.39	1.41	0.32	3.79	2.80	415	268	198
57X-5, 46-47	529.49	1.79	0.42	6.80	2.67	415	379	149

Notes: TOC = total organic carbon; HI = hydrogen index; and OI = oxygen index. Units of the various Rock-Eval parameters are given in the "Organic Geochemistry" section of the "Explanatory Notes" chapter (this volume).

Thirteen layers, characterized by very high velocity, resistivity, and density and by low gamma-ray intensity, were tentatively identified as dolomite or authigenic carbonate layers (Fig. 34). Only three dolomitic layers were visually identified in the cores (see "Lithostratigraphy" section, this chapter) probably because of incomplete recovery with the extended core barrel. Because of their high resistivity, the position and thickness of the dolomitic layers can be clearly identified on the FMS images. Dolomitic layers are present in the entire logged interval but are particularly concentrated in the lower half.

The temperature tool measures borehole fluid temperature, which can be used to estimate downhole thermal gradients provided that the data reflect borehole, rather than in situ formation, temperature. The results suggest a downhole thermal gradient of 33°C/km, an estimate which is low because of the cooling effect of circulation during drilling.

Correlation Between Holes 1081A (Walvis Ridge) and 1082A (Walvis Basin)

The downhole measurements of the two neighboring holes are very similar, despite the higher sedimentation rate observed at Site 1082 in the Walvis Basin. Both general trends and details can be correlated and allow the establishment of a reliable depth-to-depth correlation, as shown by the gamma-ray intensity curve (Fig. 35). Most of the parameters show the same range of variation at the two holes, with the exception of gamma-ray intensity and U content, which are

Table 14. Results of headspace gas analyses of sediments from Hole 1082A.

Core, section, interval (cm)	Depth (mbsf)	C_1 (ppmv)	CO_2 (ppmv)	C_2= (ppmv)	C_2 (ppmv)	H_2S (ppmv)	C_3= (ppmv	C_3 (ppmv)	C_1/C_2
175-1082A-									
1H-2, 0-5	1.50	3	1,513			14			
1H-3, 0-5	3.00	6	3,397	0.7	0.7	20		0.3	8
1H-4, 0-5	4.50	118	24,581	1.4	1.4			1.0	84
1H-5, 0-5	6.00	13	29,513	1.3	0.9			0.7	14
2H-3, 0-5	10.80	35	12,862	0.1	0.5	15			70
2H-4, 0-5	12.20	322	43,198	1.1	1.3			0.5	248
2H-5, 0-5	13.60	116	49,725	2.1	2.1			1.5	55
2H-6, 0-5	15.00	150	43,534	2.7	2.8		0.7	1.2	54
2H-7, 0-5	16.40	247	61,950	1.8	2.4			0.7	103
3H-2, 0-5	18.70	800	75,504	1.5	2.9			0.8	276
3H-3, 0-5	20.10	2,955	28,480		1.0				2,955
3H-4, 0-5	21.50	9,351	81,913	2.8	5.2		0.7	1.3	1,798
3H-5, 0-5	22.90	20,113	81,120	2.8	6.3			2.8	3,193
3H-6, 0-5	24.30	28,728	110,359	0.8	4.8	19		1.0	5,985
3H-7, 0-5	25.70	36,760	130,824	1.5	5.9			1.6	6,231
4H-2, 0-5	28.20	21,630	58,284	0.5	3.2			0.8	6,759
4H-3, 0-5	29.60	25,500	38,120	0.2	2.8	22		0.6	9,107
4H-4, 0-5	31.00	31,592	82,381	0.8	3.8			0.9	8,314
4H-5, 0-5	32.40	36,693	52,156	1.7	5.7			2.4	6,437
4H-6, 0-5	33.80	83,199	83,032	3.0	9.9		0.8	3.3	8,404
4H-7, 0-5	35.20	70,468	81,325	3.1	9.2		0.9	3.3	7,660
5H-2, 0-5	37.70	19,558	92,638	0.7	2.9			0.9	6,744
5H-3, 0-5	39.10	14,987	43,427		1.9			0.4	7,888
5H-4, 0-5	40.50	21,938	79,215	2.1	4.8		0.6	2.2	4,570
5H-5, 0-5	41.90	19,813	55,020	2.8	5.3		0.8	2.8	3,738
5H-6, 0-5	43.30	26,379		3.8	7.0		1.0	3.8	3,752
5H-7, 0-5	44.70	36,019	86,842	3.5	8.4		1.0	4.4	4,288
6H-2, 0-5	47.20	10,934	120,700	1.5	4.6		0.1	2.2	2,377
6H-3, 0-5	48.60	9,988	34,462	0.3	2.5			0.6	3,995
6H-4, 0-5	50.00	11,363	106,911	3.2	7.0		0.4	4.5	1,623
6H-5, 0-5	51.40	13,438	86,175	4.6	10.4		1.4	7.2	1,292
6H-6, 0-5	52.80	13,130		1.2	4.9		0.3	2.1	2,680
6H-7, 0-5	54.20	14,239	78,067	4.6	11.5		1.5	7.6	1,242
7H-4, 0-5	59.80	53,469	84,848	0.2	8.2			2.0	6,521
8H-5, 0-5	69.51	30,546	101,834	0.2	5.3	21		1.4	5,763
9H-5, 0-5	80.10	31,761	143,078	0.3	6.9	29		2.0	4,603
10H-5, 0-5	88.54	9,998	91,465		2.9			1.0	3,448
11H-5, 0-5	99.15	17,658	141,058	0.4	8.6			3.5	2,053
12H-5, 0-5	107.19	9,998	171,092	0.3	5.0			2.3	2,000
13H-6, 0-5	118.66	5,250	110,549	0.2	4.1	24		2.3	1,280
14H-4, 0-5	126.30	8,817	124,767	0.2	4.1			1.5	2,150
15X-3, 0-5	131.22	5,748	118,051	0.4	4.9			2.7	1,173
16X-4, 0-5	142.80	2,470	80,672		1.0			0.6	2,470
17X-2, 0-5	149.40	3,722	115,744		2.8			1.6	1,329
18X-3, 0-5	160.25	3,834	95,170	0.2	3.2			2.0	1,198
19X-3, 0-5	169.01	3,365	76,715		1.7			1.0	1,979
20X-5, 0-5	181.74	3,162	82,081		2.7			2.1	1,171
21X-4, 0-5	189.92	4,336	136,983	0.4	5.2			4.2	834
22X-4, 0-5	200.32	6,335	142,740	0.3	5.3			4.7	1,195
23X-4, 0-5	209.56	3,830	97,311	0.2	3.9		0.7	1.3	982
24X-4, 0-5	219.76	3,740			2.0			2.0	1,870
25X-4, 0-5	229.68	3,349		0.4	7.4			8.5	453
26X-4, 0-5	239.30	3,685	3,104		1.6			1.2	2,362
27X-4, 0-5	248.90	4,278		0.3	5.0			5.9	861
28X-4, 0-5	258.50	1,567	33,961	0.3	1.0			0.9	1,507
29X-4, 0-5	268.10	2,928		0.9	3.4				849
30X-4, 0-5	277.80	5,208	86,673	0.5	3.4			3.6	1,545
31X-4, 0-5	286.39	5,040		1.4	6.6		0.2	9.6	761
32X-4, 0-5	297.00	3,024	66,569	0.7	2.0			1.8	1,512
33X-4, 0-5	306.64	2,641		0.4	2.5		0.1	3.3	1,056
34X-4, 0-5	316.18	2,887		0.4	1.8			2.4	1,604
35X-4, 0-5	325.90	6,973	98,034	0.5	6.8			7.8	1,025
37X-4, 0-5	334.19	2,124	41,706	0.4	5.0			6.5	425
38X-4, 0-5	345.10	2,239		0.3	1.7			1.8	1,317
39X-4, 0-5	353.62	3,427	56,214	0.9	8.0			10.0	430
40X-5, 0-5	363.69	3,602		0.5	4.6			5.1	783
41X-4, 0-5	374.00	4,414	68,072	2.2	12.3		0.9	14.2	359
42X-4, 0-5	383.70	4,902		0.4	4.5			4.2	1,089
43X-4, 0-5	392.49	3,908		1.1	9.4			10.2	416
44X-3, 0-5	401.40	2,519	101,315	1.0	4.0		0.4	4.0	630
45X-3, 0-5	411.10	2,623		0.8	3.0		0.4	3.0	874
46X-3, 0-5	420.70	3,907		1.0	3.3			3.0	1,184
47X-4, 0-5	431.80	3,486	103,868	0.8	6.0		0.2	6.0	581
48X-3, 0-5	440.00	2,770		0.2	1.6			1.1	1,731
49X-4, 0-5	451.30	1,662	47,590	0.3	2.0			2.0	831
50X-4, 0-5	460.26	1,410		0.8	5.6			6.1	252
51X-4, 0-5	470.40	3,097	43,068	0.2	4.3			3.5	720
52X-4, 0-5	479.19	3,556		1.7	3.8		0.8	3.5	936
53X-4, 0-5	489.20	8,201	21,321	1.2	3.0		0.5	2.0	2,734
54X-5, 0-5	499.58	5,867		2.7	9.0		1.7	10.4	652
55X-4, 0-5	508.25	4,581	41,332	1.4	3.5			3.0	1,309
56X-5, 0-5	518.93	5,135		1.1	5.7		0.6	6.0	901
57X-6, 0-5	530.53	5,351	38,751	0.9	4.0			4.0	1,338
58X-4, 0-5	537.60	7,415		0.4	2.3			1.6	3,224
59X-5, 0-5	548.76	2,759	39,092	0.5	1.4			1.0	1,971
60X-5, 0-5	557.74	18,957		1.2	5.8		0.6	4.1	3,268
61X-5, 0-5	567.87	5,076	45,667	0.6	2.4			2.0	2,115

Table 14 (continued).

Core, section, interval (cm)	Depth (mbsf)	C_1 (ppmv)	CO_2 (ppmv)	C_2= (ppmv)	C_2 (ppmv)	H_2S (ppmv)	C_3= (ppmv	C_3 (ppmv)	C_1/C_2
62X-4, 0-5	576.20	10,821		0.3	3.0			2.0	3,607
63X-5, 0-5	586.30	2,942	23,015	0.5	1.6	36		1.3	1,839
64X-4, 0-5	595.40	4,214		0.3	1.8			1.6	2,341

Notes: C_1 = methane; CO_2 = carbon dioxide; C_2= = ethene; C_2 = ethane; C_3= = propene; and C_3 = propane. Dominance of C_1 over C_2 indicates that the gases originate from in situ microbial degradation of organic matter.

lower in the basin (dilution effect). The dolomitic layers are less common at Hole 1082A than at Hole 1081A.

Log-Core Correlations

The core MST and log measurements of natural gamma-ray intensity are very similar. Core data are recorded in counts per second (cps), whereas log data are presented in API (Oil Industry Standard) units. Detailed correlations between the core and log data sets are possible because of the high sedimentation rate at this site and the limited coring disturbance (Fig. 36). In Hole 1082A, log depth is similar to core depth.

REFERENCES

Barron, J.A., 1985. Late Eocene to Holocene diatom biostratigraphy of the equatorial Pacific Ocean, Deep Sea Drilling Project Leg 85. *In* Mayer, L., Theyer, F., Thomas, E., et al., *Init. Repts. DSDP,* 85: Washington (U.S. Govt. Printing Office), 413–456.

Berggren, W.A., Kent, D.V., Swisher, C.C., III, and Aubry, M.-P., 1995. A revised Cenozoic geochronology and chronostratigraphy. *In* Berggren, W.A., Kent, D.V., Aubry, M.-P., and Hardenbol, J. (Eds.), *Geochronology, Time Scales and Global Stratigraphic Correlation.* Spec. Publ.—Soc. Econ. Paleontol. Mineral. (Soc. Sediment. Geol.), 54:129–212.

Blow, W.H., 1969. Late middle Eocene to Recent planktonic foraminiferal biostratigraphy. *In* Brönnimann, P., and Renz, H.H. (Eds.), *Proc. First Int. Conf. Planktonic Microfossils, Geneva, 1967:* Leiden (E.J. Brill), 1:199–422.

Brunner, C.A., 1991. Latest Miocene to Quaternary biostratigraphy and paleoceanography, Site 704, subantarctic South Atlantic Ocean. *In* Ciesielski, P.F., Kristoffersen, Y., et al., *Proc. ODP, Sci. Results,* 114: College Station, TX (Ocean Drilling Program), 201–215.

Caulet, J.-P., 1991. Radiolarians from the Kerguelen Plateau, Leg 119. *In* Barron, J., Larsen, B., et al., *Proc. ODP, Sci. Results,* 119: College Station, TX (Ocean Drilling Program), 513–546.

Claypool, G.E., and Kvenvolden, K.A., 1983. Methane and other hydrocarbon gases in marine sediment. *Annu. Rev. Earth Planet. Sci.,* 11:299–327.

Cragg, B.A., Harvey, S.M., Fry, J.C., Herbert, R.A., and Parkes, R.J., 1992. Bacterial biomass and activity in the deep sediment layers of the Japan Sea, Hole 798B. *In* Pisciotto, K.A., Ingle, J.C., Jr., von Breymann, M.T., Barron, J., et al., *Proc. ODP, Sci. Results.,* 127/128 (Pt. 1): College Station, TX (Ocean Drilling Program), 761–776.

Eisma, D., and Van der Gaast, S.J., 1971. Determination of opal in marine sediments by X-ray diffraction. *Neth. J. Sea Res.,* 5:382–389.

Emerson, S., and Hedges, J.I., 1988. Processes controlling the organic carbon content of open ocean sediments. *Paleoceanography,* 3:621–634.

Gartner, S., 1977. Calcareous nannofossil biostratigraphy and revised zonation of the Pleistocene. *Mar. Micropaleontol.,* 2:1–25.

Guyodo, Y., and Valet, J.-P., 1996. Relative variations in geomagnetic intensity from sedimentary records: the past 200,000 years. *Earth. Planet. Sci. Lett.,* 143:23–36.

Kennett, J.P., and Srinivasan, M.S., 1983. *Neogene Planktonic Foraminifera: A Phylogenetic Atlas:* Stroudsburg, PA (Hutchinson Ross).

Kent, D.V., and Opdyke, N.D., 1977. Paleomagnetic field intensity variation recorded in a Brunhes epoch deep-sea sediment core. *Nature,* 266:156–159.

King, J.W., Banerjee, S.K., and Marvin, J., 1983. A new rock-magnetic approach to selecting sediments for geomagnetic paleointensity studies: application to paleointensity for the last 4000 years. *J. Geophys. Res.,* 88:5911–5921.

Lazarus, D., 1992. Antarctic Neogene radiolarians from the Kerguelen Plateau, Legs 119 and 120. *In* Wise, S.W., Jr., Schlich, R., et al., *Proc. ODP, Sci. Results,* 120: College Station, TX (Ocean Drilling Program), 785–809.

Martini, E., 1971. Standard Tertiary and Quaternary calcareous nannoplankton zonation. *In* Farinacci, A. (Ed.), *Proc. 2nd Int. Conf. Planktonic Microfossils Roma:* Rome (Ed. Tecnosci.), 2:739–785.

Meyers, P.A., 1994. Preservation of elemental and isotopic source identification of sedimentary organic matter. *Chem. Geol.,* 144:289–302.

————, 1997. Organic geochemical proxies of paleoceanographic, paleolimnologic, and paleoclimatic processes. *Org. Geochem.,* 27:213–250.

Millero, F.J., and Sohn, M.L., 1992. *Chemical Oceanography:* Boca Raton (CRC Press).

Moore, T.C., Jr., 1995. Radiolarian stratigraphy, Leg 138. *In* Pisias, N.G., Mayer, L.A., Janecek, T.R., Palmer-Julson, A., and van Andel, T.H. (Eds.), *Proc. ODP, Sci. Results,* 138: College Station, TX (Ocean Drilling Program), 191–232.

Motoyama, I., 1996. Late Neogene radiolarian biostratigraphy in the subarctic Northwest Pacific. *Micropaleontology,* 42:221–260.

Müller, P.J., 1977. C/N ratios in Pacific deep sea sediments: effect of inorganic ammonium and organic nitrogen compounds sorbed by clays. *Geochim. Cosmochim. Acta,* 41:765–776.

Okada, H., and Bukry, D., 1980. Supplementary modification and introduction of code numbers to the low-latitude coccolith biostratigraphic zonation (Bukry, 1973; 1975). *Mar. Micropaleontol.,* 5:321–325.

Peters, K.E., 1986. Guidelines for evaluating petroleum source rock using programmed pyrolysis. *AAPG Bull.,* 70:318–329.

Sanfilippo, A., Westberg-Smith, M.J., and Riedel, W.R., 1985. Cenozoic radiolaria. *In* Bolli, H.M., Saunders, J.B., and Perch-Nielsen, K. (Eds.), *Plankton Stratigraphy:* Cambridge (Cambridge Univ. Press), 631–712.

Valet, J.-P., and Meynadier, L., 1993. Geomagnetic field intensity and reversals during the past four million years. *Nature,* 336:234–238.

Yamazaki, T., and Ioka, N., 1994. Long-term secular variation of the geomagnetic field during the last 200 kyr recorded in sediment cores from the western equatorial Pacific. *Earth Planet. Sci. Lett.,* 128:527–544.

Yamazaki, T., Ioka, N., and Eguchi, N., 1995. Relative paleointensity of the geomagnetic field during the Brunhes Chron. *Earth Planet. Sci. Lett.,* 136:525–540.

Ms 175IR-110

NOTE: Core-description forms ("barrel sheets") and core photographs can be found in Section 4, beginning on page 581. Forms containing smear-slide data and shore-based log processing data can be found on CD-ROM. See Table of Contents for materials contained on CD-ROM.

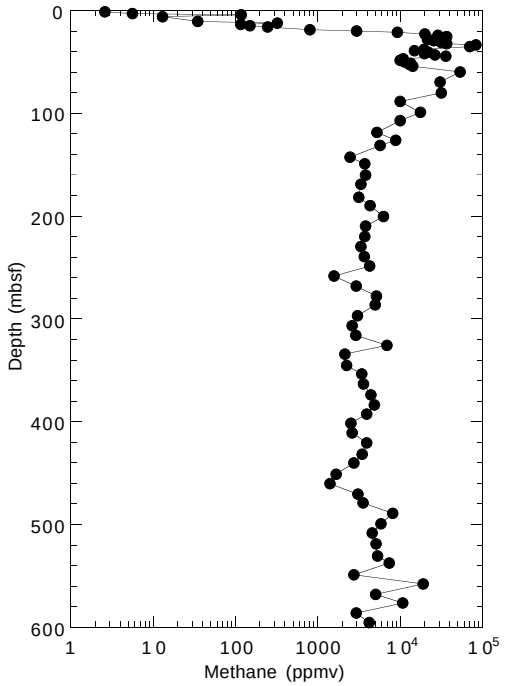

Figure 27. Headspace methane concentrations in sediments from Hole 1082A.

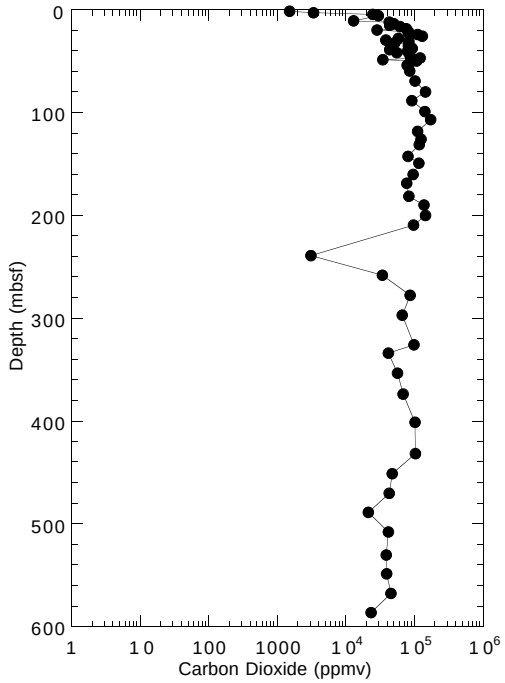

Figure 28. Headspace CO_2 concentrations in sediments from Hole 1082A.

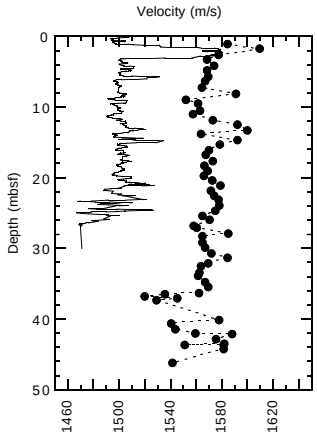

Figure 29. Discrete velocity profile (solid circles) compared with MST P-Wave velocities (solid line) measured at Hole 1082A.

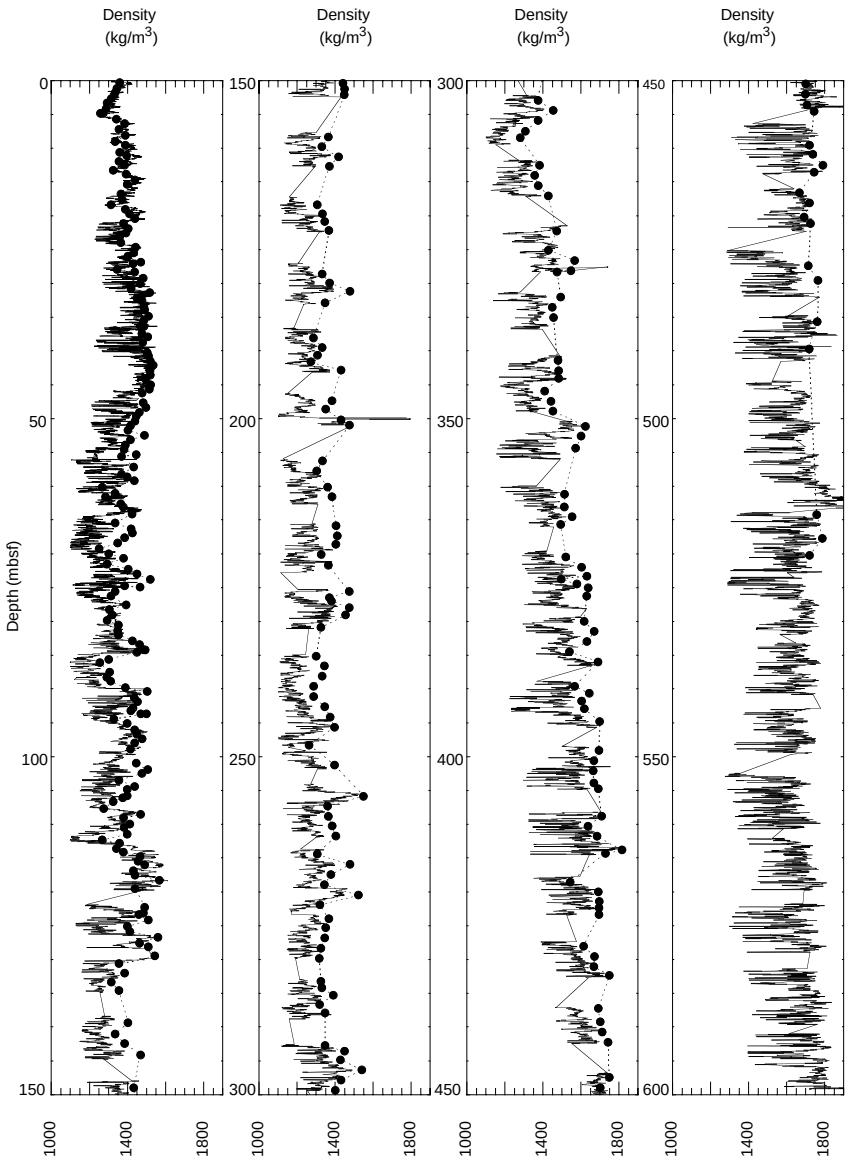

Figure 30. Gravimetric wet bulk density compared with GRAPE bulk density at Hole 1082A.

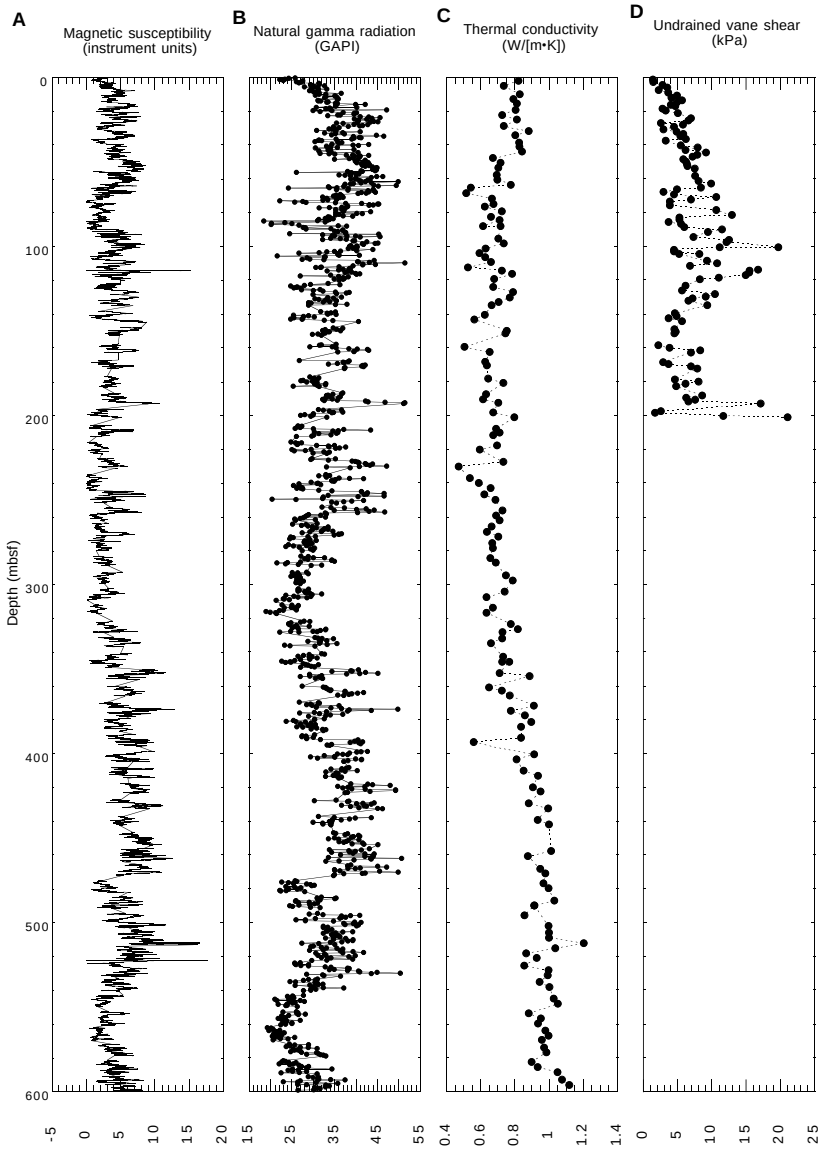

Figure 31. Comparison of (**A**) magnetic susceptibility with (**B**) natural gamma radiation from MST measurements and discrete values of (**C**) thermal conductivity and (**D**) undrained vane shear strength over the entire depth range of 600m at Hole 1082A.

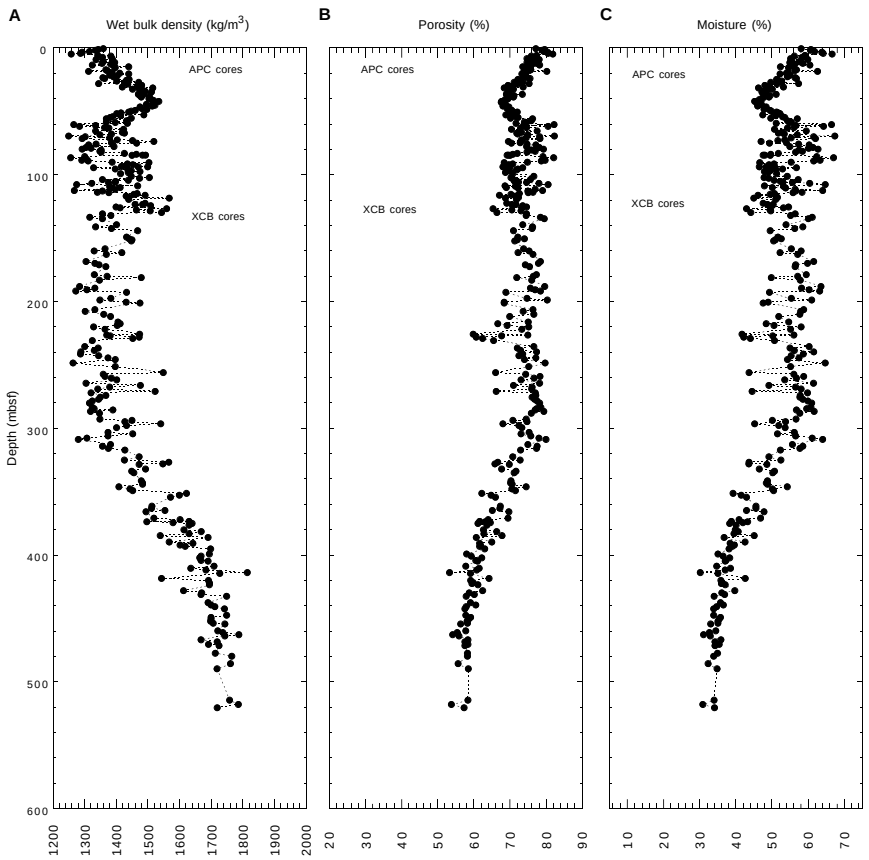

Figure 32. Gravimetric (**A**) wet bulk density, (**B**) porosity, and (**C**) moisture content derived from index properties measurements at Hole 1082A.

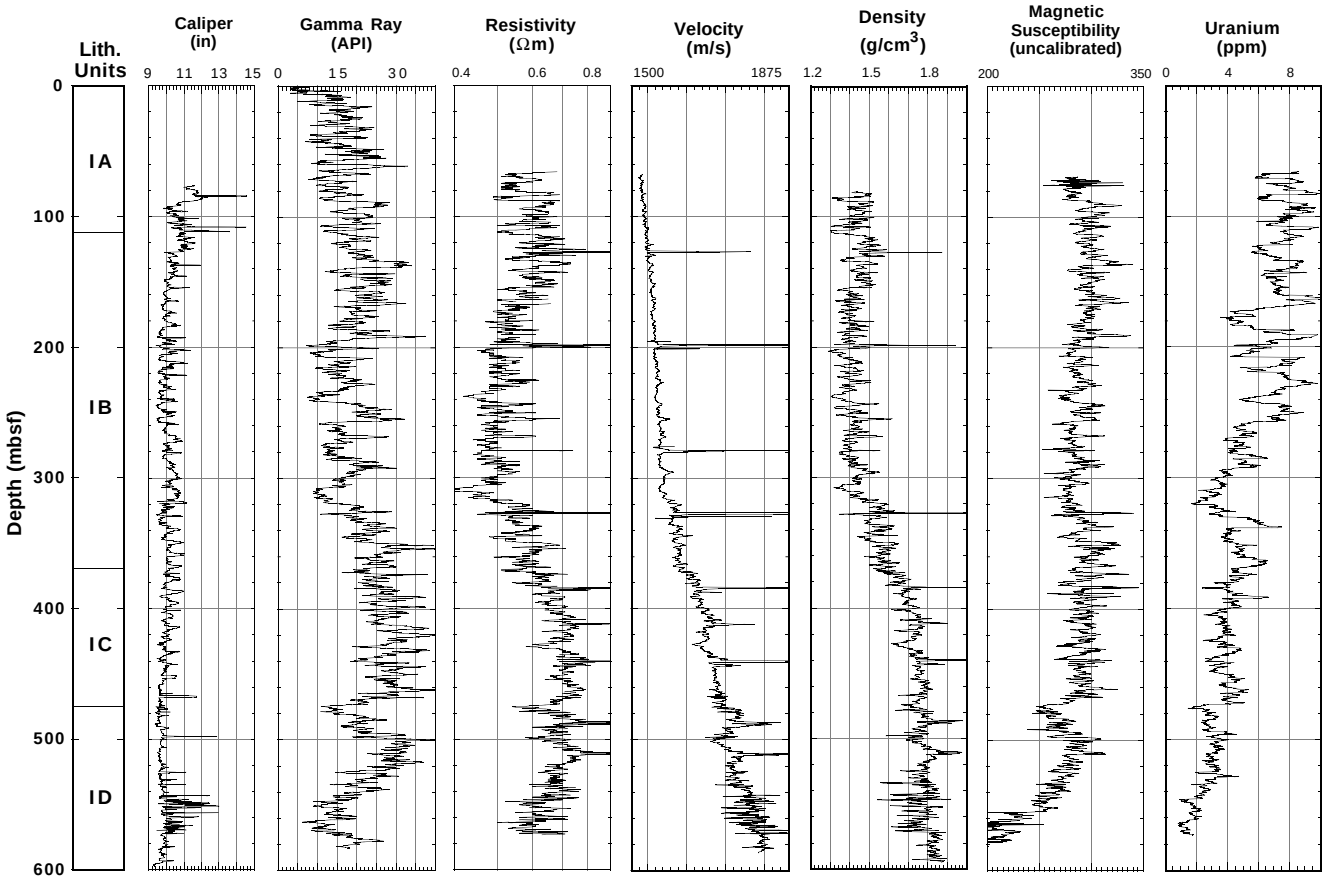

Figure 33. Downhole logs of caliper, natural gamma-ray, resistivity, velocity, density, magnetic susceptibility, and uranium content for Hole 1082A.

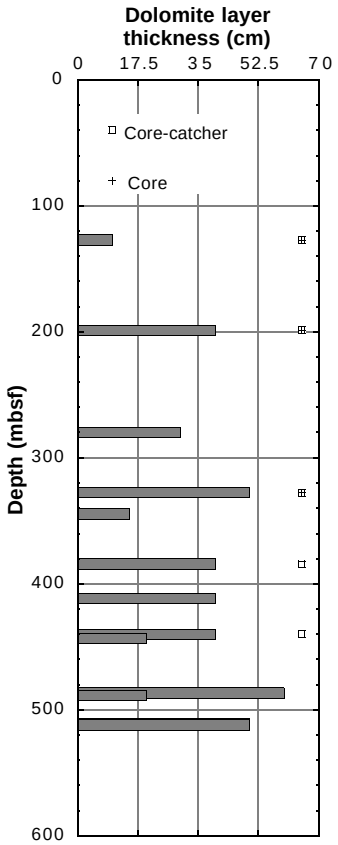

Figure 34. Thickness of the dolomitic layers, as identified from Hole 1082A logs. Core and core-catcher observations also are included.

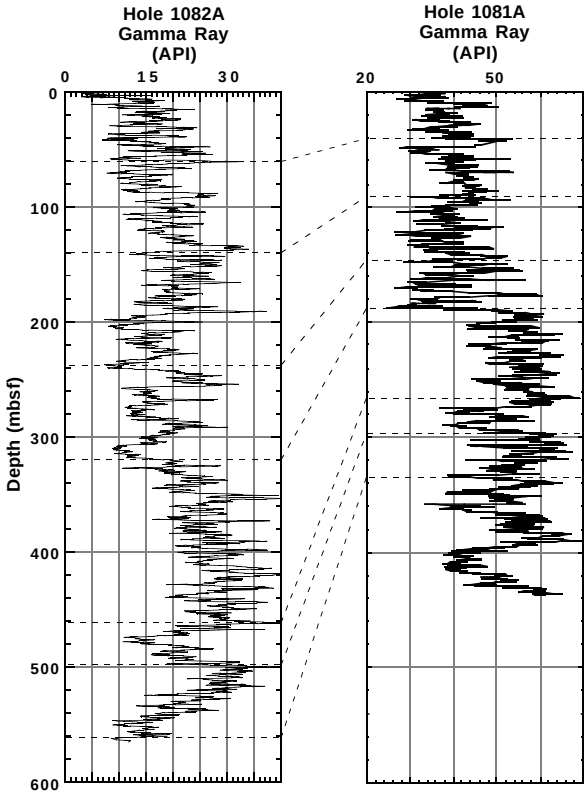

Figure 35. Downhole gamma-ray logs compared between Holes 1082A (Walvis Basin) and 1081A (Walvis Ridge).

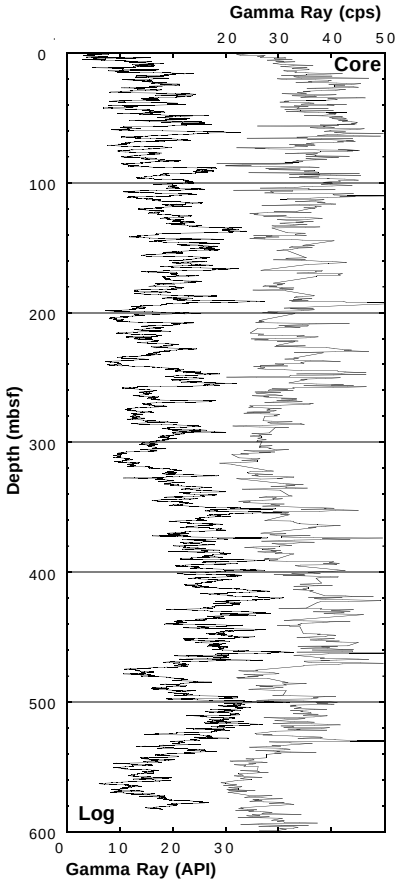

Figure 36. Comparison of core (MST) and log natural gamma-ray data for Hole 1082A.